Impact of Strain and Alloy Disorder on the Electronic Properties of III-Nitride Based Two-dimensional Electron Gases

Thèse N° 9469

Présentée le 23 août 2019

à la Faculté des sciences de base
Laboratoire en semiconducteurs avancés pour la photonique et l'électronique
Programme doctoral en physique

pour l'obtention du grade de Docteur ès Sciences

par

Pirouz SOHI

Acceptée sur proposition du jury

Prof. R. Houdré, président du jury
Prof. N. Grandjean, directeur de thèse
Dr F. Semond, rapporteur
Dr J. Kuzmík, rapporteur
Prof. E. Matioli, rapporteur

2019

ÉCOLE POLYTECHNIQUE
FÉDÉRALE DE LAUSANNE

I learned very early the difference between knowing
the name of something and knowing something.
— Richard P. Feynman

To my parents . . .

Acknowledgements

First of all I would like to thank my supervisor, Prof. Nicolas Grandjean for giving me the opportunity to work in his outstanding research group. He offered me both academic and personal support throughout my thesis for which I am very grateful. Discussions with Nicolas were always fruitful thanks to his amazing insight and curious spirit.
I would also like to thank Dr. Jean-François Carlin for all his help, guidance and patience. I am particularly grateful for all the time he took to teach me about MOVPE and XRD. Furthermore, I would like to thank Denis Martin for teaching me how to use the MBE-system and keeping the machine running non-stop. Denis was always ready to help, even when I called him at 4 AM because of a malfunction in the setup. I would also like to thank Dr. Raphaël Butté for his red pen of doom while proofreading papers and this thesis. It was always a pleasure to have a beer/coffee with him and take in all the observational humor that he provided. Furthermore, I would like to thank Dr. Ian Rousseau for correcting the first draft of my thesis. I also would like to thank Prof. Mauro Mosca for the fabrication of TJ-LEDs and all the sweets he brought back from Sicily. I would like to thank Dr. Marco Malinverni for teaching me how to do Piranha cleaning and the MBE regrowth. Furthermore, I am thankful to Camille Haller for helping me with the PL setup many times. I am also thankful to Dr. Gordon Callsen for performing μ-PL and Raman measurements. Furthermore, I really enjoyed all his neat stories and anecdotes. I would like to thank Dr. Gwénolé Jacopin and Wei Liu for CL measurements and also Prof. Kanako Shojiki for AFM measurements at CMI. Furthermore, I would like to express my gratitude to Nicolas Leiser, Damien Trolliet, Jonathan Delaloye and Yoan Trolliet for keeping the MBE and the clean rooms in a working order.
A special thanks goes to my office mates and friends Camille, Sebastian and Ian for all the morning coffees, lunchtimes, drinks and dinners. I am also grateful to Sebastian for the occasional beer at SAT where we discussed physics and life.
Finally, I would like to thank my parents and Claudia for all their love and support. I am truly lucky to have you all in my life.

Lausanne
June, 2019 Pirouz Sohi

Abstract

Over the past 20 years, III-nitrides (GaN, AlN, InN and their alloys) have proven to be an excellent material group for electronic devices, in particular, for high electron mobility transistors (HEMTs) operating at high frequency and high power. This is mainly thanks to the wide band gap of III-nitrides and the spontaneous polarization along the technologically relevant (0001) direction. Heteroepitaxy of III-nitride heterostructures enables the formation of two-dimensional electron gases (2DEGs) with high carrier densities (> 10^{13} cm^{-2}) and high electron mobilities (2000 cm^2 V^{-1} s^{-1}). The heterostructures usually consist of AlGaN, InAlN or AlN barriers grown epitaxially on GaN buffers. Devices based on these structures exhibit excellent performance and have reached technological maturity, enabling notably the commercialization of AlGaN/GaN HEMTs. Despite the success of III-nitride HEMTs thus far, the full potential of the material group for electronics has not yet been unleashed.

The aim of this thesis is to investigate two novel heterostructure designs and to determine the physical mechanisms limiting their electronic properties. This was done by epitaxial growth followed by characterization of material and electronic properties.

The first studied heterostructure was AlN/GaN/AlN where the GaN channel is fully strained to AlN. In order to achieve pseudomorphic growth of GaN on AlN, the onset of strain relaxation, i.e., the critical thickness, is of paramount importance. Furthermore, the impact of growth parameters such as temperature and initial dislocation density need to be considered. Over the past years several research groups have reported on the electronic properties of ultra-thin GaN channels on AlN. Interestingly, all reported 2DEGs suffer from a low electron mobility with values usually below 600 cm^2 V^{-1} s^{-1}. In this thesis, the strain relaxation and critical thickness of GaN on AlN was determined. Furthermore, the origin of low electron mobility for AlN/GaN/AlN heterostructures and in general thin-GaN channels grown on AlN were systematically studied.

The second heterostructure that was investigated during this thesis was based on InGaN channels. In this case, the 2DEG is formed in an In-rich InGaN layer. The low electron effective mass of InN (0.05 m_0) compared to GaN (0.2 m_0) should theoretically give rise to a higher electron mobility. However, for In-rich channels alloy disorder scattering is particularity strong in III-nitrides. This has been shown both by optical measurements and theoretical calculations based on the localization landscape theory. Surprisingly, high electron mobilities have been reported in literature for high In content InGaN channels. In these cases, the electron mobility appears not to be limited by alloy disorder scattering. During this thesis, the electron mobility of InGaN channels was determined as a function of In content. Fur-

thermore, the unintentional growth of GaN interlayers is proposed as the possible origin for the reported high electron mobilities in literature.
Finally, low temperature growth of highly Si-doped GaN by metalorganic vapor-phase epitaxy (MOVPE) was optimized. This was applied for two applications. (i) Fabrication of low resistance ohmic contacts for HEMTs and (ii) growth of tunnel junctions (TJ) on blue light emitting diodes (LEDs). In both cases, the aim was to pave the way for large-scale production of HEMTs and TJ-based LEDs by MOVPE.

Zusammenfassung

In den letzten 20 Jahren haben sich III-Nitride (GaN, AlN, InN und ihre Legierungen) als eine hervorragende Materialgruppe für elektronische Bauelemente erwiesen. Dies gilt insbesondere für High-electron-mobility Transistoren (HEMTs), die mit hoher Frequenz und hoher Leistung arbeiten. Dies ist vor allem auf die grosse Bandlücke der III-Nitriden und die spontane Polarisation entlang der technologisch relevanten (0001)-Richtung zurückzuführen. Die Heteroepitaxie von III-Nitrid-Heterostrukturen ermöglicht die Bildung von zweidimensionalen Elektronengasen (2DEG) mit hohen Ladungsträgerdichten (> 10^{13} cm^{-2}) und hohen Elektronenmobilitäten (2000 cm^2 V^{-1} s^{-1}). Die Heterostrukturen bestehen üblicherweise aus AlGaN-, InAlN- oder AlN-Barrieren, die auf GaN epitaktisch gewachsen sind. Auf diesen Strukturen basierende Bauelemente weisen eine hervorragende Leistung auf und haben eine hohe technologische Reife erreicht, was insbesondere die Kommerzialisierung von AlGaN/GaN-HEMTs ermöglicht. Trotz des bisherigen Erfolgs von III-Nitrid-HEMTs ist das volle Potenzial der Materialgruppe für die Elektronik noch nicht ausgeschöpft.

Das Ziel dieser Arbeit ist es, zwei neuartige Heterostrukturen zu untersuchen und die physikalischen Mechanismen zu bestimmen, die ihre elektronischen Eigenschaften einschränken. Dies erfolgte durch epitaktisches Wachstum, gefolgt von der Charakterisierung der Material- und elektronischen Eigenschaften.

Die erste untersuchte Heterostruktur war AlN/GaN/AlN, wobei der GaN-Kanal vollständig auf AlN verspannt ist. Um ein pseudomorphes Wachstum von GaN auf AlN zu erreichen, wurde der Beginn der Spannungsrelaxation, d.h. die kritische Dicke, bestimmt. Des Weiteren wurden die Auswirkungen von Wachstumsparametern wie Temperatur und anfänglicher Versetzungsdichte untersucht. In den letzten Jahren haben mehrere Forschungsgruppen über die elektronischen Eigenschaften ultradünner GaN-Kanäle auf AlN berichtet. Interessanterweise leiden alle berichtete 2DEGs unter einer niedrigen Elektronenmobilität mit Werten, die generell unter 600 cm^2 V^{-1} s^{-1} liegen. In dieser Arbeit wurden die Spannungsrelaxation und die kritische Dicke von GaN auf AlN bestimmt. Darüber hinaus wurde systematisch der Ursprung der niedrigen Elektronenbeweglichkeit für AlN/GaN/AlN-Heterostrukturen und allgemein für dünne GaN-Kanäle auf AlN untersucht.

Die zweite Heterostruktur, die in dieser Arbeit untersucht wurde, basiert auf InGaN-Kanälen. In diesem Fall wird das 2DEG in einer In-reichen InGaN-Schicht gebildet. Die niedrige effektive Elektronenmasse von InN (0.05 m_0) im Vergleich zu GaN (0.2 m_0) sollte theoretisch zu einer höheren Elektronenbeweglichkeit führen. Bei In-reichen-Kanälen ist jedoch die Streuung der Legierungsstörung in III-Nitriden besonders stark. Dies wurde sowohl durch optische

Messungen als auch durch theoretische Berechnungen basierend auf der Theorie der Lokalisierungslandschaft gezeigt. Überraschenderweise wurde in der Literatur über hohe Elektronenmobilitäten für InGaN-Kanäle mit gesteigertem In-Gehalt berichtet. In diesen Fällen scheint die Elektronenbeweglichkeit nicht durch die Streuung der Legierungsstörung begrenzt zu sein. In dieser Arbeit wurde die Elektronenmobilität von InGaN-Kanälen als Funktion des In-Gehalts untersucht. Darüber hinaus wurde ein möglicher Ursprung für die in der Literatur berichteten hohen Elektronenmobilitäten vorgeschlagen.
Schliesslich wurde das Niedrigtemperaturwachstum von hoch Si dotiertem GaN durch metallorganische Gasphasenepitaxie (MOVPE) optimiert. Dies wurde für zwei Anwendungen angewendet: (i) Herstellung ohmscher Kontakte mit niedrigem Wiederstand für HEMTs und (ii) Wachstum von Tunnelkontakten (TJ) auf blauen Leuchtdioden (LED). In beiden Fällen sollte der Weg für die grosstechnische Produktion von HEMTs und TJ-basierten LEDs durch MOVPE geebnet werden.

Contents

Acknowledgements **v**

Abstract (English/Deutsch) **vii**

1 Introduction **1**

Introduction **1**

2 Basic properties of III-nitrides **5**
2.1 Crystal and band structures . . . 5
2.2 Polarization . . . 7
2.2.1 Spontaneous polarization . . . 8
2.2.2 Piezoelectric polarization . . . 8
2.3 III-nitride two-dimensional electron gases . . . 11
2.4 Strain relaxation and critical thickness . . . 15
2.4.1 Critical thickness . . . 16
2.4.2 Dislocations . . . 18

3 Experimental method **21**
3.1 Epitaxial growth . . . 21
3.1.1 Molecular beam epitaxy . . . 22
3.1.2 Metalorganic vapor phase epitaxy . . . 24
3.1.3 Substrates . . . 26
3.2 Material characterization . . . 27
3.2.1 Reflection high-energy electron diffraction . . . 27
3.2.2 High resolution x-ray diffraction . . . 29
3.2.3 Atomic force microscopy . . . 32
3.2.4 Photoluminescence . . . 32
3.3 Electrical characterization . . . 32
3.3.1 Four-point probe technique . . . 33
3.3.2 Van der Pauw theorem . . . 34
3.3.3 Hall effect . . . 35
3.3.4 Transmission line measurement . . . 37
3.4 Simulation software: NextNano . . . 39

4 Heteroepitaxy: GaN on AlN **41**
4.1 Background . . . 41
4.2 Critical thickness of GaN on AlN . . . 42
4.3 Growth interruptions . . . 51
4.4 Pseudomorphic growth . . . 53
4.5 Summary . . . 56

5 AlN/GaN/AlN heterostructures **57**
5.1 Background . . . 57
5.2 Channel thickness . . . 58
5.2.1 AlN/GaN interface instability . . . 61
5.3 Barrier . . . 64
5.4 Dislocation-induced surface roughening . . . 66
5.5 Dislocation scattering . . . 66
5.6 Modulation-doped heterostructures . . . 71
5.7 Summary . . . 75

6 InGaN-based channels **77**
6.1 Background . . . 77
6.1.1 InGaN alloy disorder . . . 77
6.1.2 Power electronics with InGaN channels . . . 79
6.2 Electron mobility of InGaN channels . . . 79
6.3 Impact of GaN interlayers . . . 85
6.4 Summary . . . 87

7 Ohmic contacts grown by MOVPE **89**
7.1 Background . . . 89
7.1.1 Ohmic contacts . . . 89
7.1.2 Alloyed ohmic contacts . . . 90
7.1.3 Ohmic contacts by MBE . . . 90
7.2 Regrowth of ohmic contacts by MOVPE . . . 91
7.2.1 Low temperature growth of n^{++} GaN by MOVPE . . . 91
7.2.2 Fabrication of TLM structures . . . 94
7.2.3 Optimization of SiO_x mask . . . 94
7.2.4 Optimization of regrowth temperature . . . 95
7.2.5 Summary . . . 97

8 Conclusions **99**
8.1 Summary . . . 99
8.2 Outlook . . . 101

A Tunnel junctions by MOVPE **103**
A.1 Background 103
A.2 Tunnel junctions on blue LEDs by MOVPE 104
A.3 Summary 107

B Acronyms **109**

Curriculum Vitae **127**

1 Introduction

III-nitride compounds (GaN, AlN and InN) and their alloys are wide-bandgap semiconductors with an energy that ranges from 0.64 to 6.00 eV, covering the electromagnetic spectrum from infrared deep into the ultraviolet. Over the past 20 years, the growth and fabrication technology of III-nitrides have matured significantly, enabling the commercialization of blue light emitting diodes and laser diodes [1]. III-nitrides are furthermore attractive for electronic applications, particularly for the fabrication of high electron mobility transistors (HEMTs) operating at high power and high frequencies [2, 3]. Thanks to their large band gap and material stability, III-nitride based transistors are also interesting for high temperature applications and could be used in harsh environments [4]. In Tab. 1.1 the critical properties of GaN for high power and high frequency applications are compared to conventional semiconductors. The high electron saturation velocity in GaN allows for shorter transient times for electrons moving below the transistor gate. This time scale directly determines the maximum frequency at which the device can be operated. The wide band gap (E_g) of GaN allows for high breakdown voltages, and the high polarization-induced two-dimensional electron gas (2DEG) density gives rise to high current densities. Furthermore, the high thermal conductivity (κ) compared to conventional III-V semiconductors (GaAs) and Si enables efficient heat management. These properties make III-nitrides appealing for HEMTs. It is worth mentioning that SiC and diamond do have better characteristics compared to GaN in certain aspects. However, the epitaxial growth of heterostructures and doping [5, 6] have proven to be very challenging in these material systems.

During this thesis, several open questions in III-nitride electronics were addressed with an emphasis on the underlying physics. The main physical properties that were investigated were strain and alloy disorder. The electronic properties of 2DEGs were studied for particular heterostructure designs which were predicted to exhibit excellent device performance.
The first structure consists of a fully pseudomorphic AlN/GaN/AlN heterostructure where the 2DEG resides within a thin GaN channel and the AlN acts both as a barrier and as a back-barrier. This configuration has several advantages: pseudomorphic growth of GaN on AlN prevents the introduction of charged dislocations, which are known to impact the electronic

Material	μ (cm^2 V^{-1} s^{-1})	E_g (eV)	v_{sat} (10^7 cm s^{-1})	E_{break} (kV cm^{-1})	κ (W m^{-1} K^{-1})
Si	600	1.12	1.0	300	150
GaAs	8500	1.42	1.0	400	46
Diamond	2200	5.45	2.7	10000	2200
SiC	1000	3.26	2.0	2200	440
GaN	2000	3.44	2.0	2000	230

Table 1.1 – Material comparison for high power and high frequency electronics at 300 K [7].

properties of the 2DEG and give rise to gate leakage currents in electronic devices [8]. Furthermore, the 2DEG is strongly confined between the wide band gap (6.00 eV) AlN barrier and back-barrier. Due to the high polarization-mismatch between GaN and AlN, a high 2DEG density ($> 1\times10^{13}$ cm^{-2}) is achievable even for very thin barrier thicknesses (~ 2 nm) [9]. This is very attractive for high frequency operation when down scaling the aspect ratio between the gate width and channel length. Ideally the heterostructure would be grown on AlN single crystal substrates in order to take advantage of the high thermal conductivity of AlN (compared to GaN), allowing for efficient heat management when operating at high power. In order to achieve pseudomorphic AlN/GaN/AlN heterostructures and prevent strain relaxation, the impact of growth conditions (e.g. temperature) needs to be well understood. One of the main objectives during this thesis was therefore to obtain a fundamental understanding of the strain relaxation process in such structures and in particular the critical thickness for GaN grown on AlN.
The second main topic studied during this thesis was alloy disorder scattering and in particular the impact thereof on the electron mobility of 2DEGs residing in InGaN channels as a function of In content. From the electronics point-of-view, the electron mobility is expected to increase with increasing In content due to the lower electron effective mass of InN compared to GaN. However, the impact of alloy disorder scattering needs to be considered for high In content channels, since it potentially might counteract the benefits of a lower electron effective mass. From optical measurements, it is well known that both electrons and holes are strongly affected by the disorder present in InGaN QWs.
The objective of the last topic discussed in this thesis is the fabrication of ohmic contacts for HEMTs by an industrially scalable technique (metalorganic vapor-phase epitaxy) instead of molecular beam epitaxy, which is technologically more demanding for III-nitride compounds.

- **Chapter 2: Basic properties of III-nitrides**- Discusses the basic properties of III-nitrides. 2DEGs based on III-nitrides are introduced. The theory and experimental results on strain relaxation and critical thickness are summarized.

- **Chapter 3: Experimental methods**- Discusses the experimental methods used during this thesis. Epitaxial growth is discussed in detail followed by the introduction of growth techniques used during the thesis. Background information on the material

and electrical characterization techniques are provided.

- **Chapter 4: Heteroepitaxy: GaN on AlN**- Investigates the strain relaxation and critical thickness of GaN grown on AlN as a function of growth temperature and initial dislocation density. Furthermore, the impact of growth interruptions on the strain relaxation was studied. The optimization of pseudomorphic GaN layers grown at reduced temperatures is investigated.
- **Chapter 5: AlN/GaN/AlN heterostructures**- Discusses the low electron mobility observed in AlN/GaN/AlN heterostructures. The impact of GaN channel thickness is investigated. The AlN/GaN interface instability is examined. The impact of barrier and substrate type is discussed. A dislocation scattering model is applied to a barrier thickness dependent series. The origin of the low electron mobility in AlN/GaN/AlN heterostructures is explored. Finally, a novel scheme for ultra-thin GaN channels with modulation-doping is presented.
- **Chapter 6: InGaN-based channels**- Investigates the electronic properties of InGaN channel 2DEGs. Alloy disorder in InGaN layers is discussed. The electron mobility of 2DEGs residing in InGaN channels is determined. The electron mobility is compared to a theoretical model as a function of In content. The discrepancy in the values reported in literature is studied. The impact of unintentional GaN interlayers between InGaN channel and barrier is discussed.
- **Chapter 7: Ohmic contacts grown by MOVPE**- Discusses the low temperature growth of highly Si-doped GaN by MOVPE and its application as regrown ohmic contacts for HEMTs. The concept of ohmic contacts and the need for low contact resistance is discussed. The state-of-the-art in fabrication of ohmic contacts is elaborated. The optimization of low temperature growth of highly Si-doped GaN is presented. The effect of growth temperature on the hardmask stoichiometry is discussed. The n^{++} GaN is applied to InAlN/GaN HEMTs as regrown ohmic contacts.
- **Chapter 8: Conclusions**- Summarizes the obtained results with outlook on potential future research.

2 Basic properties of III-nitrides

In this chapter, the basic properties of III-nitrides are discussed in order to pave the way for the experimental results provided in the following chapters. In the first part, the crystal structure of III-nitrides is detailed, followed by a review of the mechanical and electronic properties.

2.1 Crystal and band structures

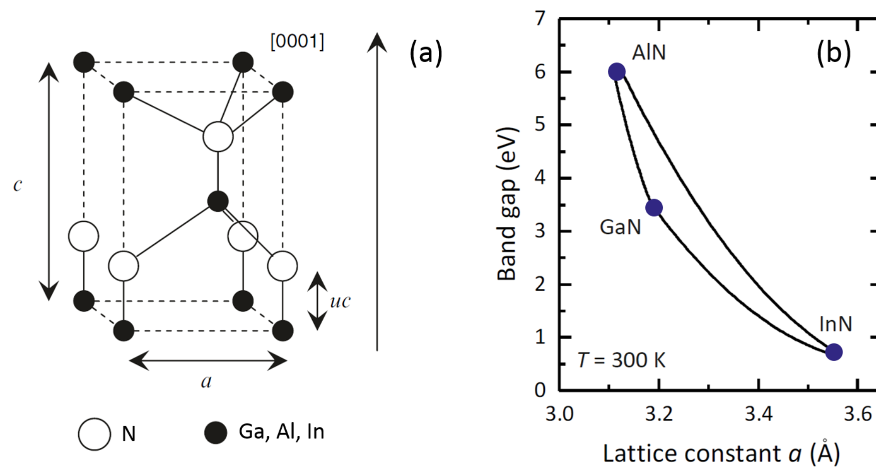

Figure 2.1 – (a) Wurtzite crystal structure of III-nitrides. (b) Room-temperature band gap energy and *in-plane* lattice constant a of III-nitrides. Reproduced with modification from [10] and permission from Springer Nature.

III-nitrides (GaN, AlN, InN and their ternary and quaternary alloys) are semiconductor compounds which have a thermodynamically stable wurtzite crystal structure with hexagonal six-fold symmetry. Cations (metal) and anions (nitrogen) form two interpenetrating hexagonal close-packed structures which are shifted along the (0001) direction (c-axis) and stacked in an ABABAB sequence, as shown in Fig. 2.1(a). The distance between successive planes (AB) corresponds to the bond length between anions and cations and can be expressed by uc,

Material	a (Å)	c (Å)	c/a	$\Delta c/a$	u	E_g (eV)
InN	3.545	5.703	1.6087	-0.0243	0.3787	0.64
GaN	3.189	5.185	1.6259	-0.0071	0.3769	3.44
AlN	3.112	4.982	1.6009	-0.0321	0.3814	6.00

Table 2.1 – Room-temperature lattice parameters a and c [11], ratio (c/a), internal displacement parameter u [12], deviation parameter reflecting departure from ideal wurtzite structure ($\Delta c/a$) and room-temperature band gap (band to band) energy (E_g) of InN [13], GaN [11] and AlN [14].

where u is the internal parameter and c is the lattice constant in the direction of the stacking. Within each basal plane, atoms are separated by the *in-plane* lattice constant a. For the ideal wurtzite structure each atom is bonded to four atoms, where each atom is positioned at the corners of a regular tetrahedron with a bonding angle of 109.47 °. In the ideal case the lattice constants are expected to fulfill the following conditions:

$$c/a = \sqrt{8/3} \sim 1.633, \qquad u = 0.375. \tag{2.1}$$

Due to the strong ionic character of III-nitrides, the bilayer stacking planes are attracted to each other (large difference in electronegativity) giving rise to a distortion of the crystal from the ideal case. In Tab. 2.1, the lattice constants (a and c), their ratio (c/a) and the internal displacement parameter (u) of III-nitride binary compounds are given. The strong ionic bond in III-nitrides is reflected in the negative sign of $\Delta c/a$, which gives the deviation of (c/a) from the ideal case. Hence, the wurtzite crystal is extended along the (0001) direction. For ternary alloys of III-nitrides the lattice constants can be linearly interpolated (Vegard's law) and are given (in Å) by [15]

$$\begin{aligned}
a_{\mathrm{Al_xGa_{1-x}N}}(x) &= 3.189 - 0.089x, \\
a_{\mathrm{In_xGa_{1-x}N}}(x) &= 3.189 + 0.386x, \\
a_{\mathrm{In_{1-x}Al_xN}}(x) &= 3.545 - 0.475x, \\
\\
c_{\mathrm{Al_xGa_{1-x}N}}(x) &= 5.185 - 0.232x, \\
c_{\mathrm{In_xGa_xN}}(x) &= 5.185 + 0.574x, \\
c_{\mathrm{In_{1-x}Al_xN}}(x) &= 5.703 - 0.806x.
\end{aligned} \tag{2.2}$$

The strong orbital overlap gives rise to a band gap energy (E_g) which ranges from 0.64 to 6.00 eV for III-nitrides (Tab. 2.1). The band gap energy for ternary alloys can be expressed to

second order by (in eV) [16–19]

$$\begin{aligned} E^{g}_{\mathrm{AlGaN}}(x) &= 6.00x + 3.44(1-x) - 1.00x(1-x), \\ E^{g}_{\mathrm{InGaN}}(x) &= 0.64x + 3.44(1-x) - 1.67x(1-x), \\ E^{g}_{\mathrm{InAlN}}(x) &= 6.00x + 0.64(1-x) - 3.10x(1-x). \end{aligned} \tag{2.3}$$

In Fig. 2.2, the band alignment of the binary III-nitrides is given.

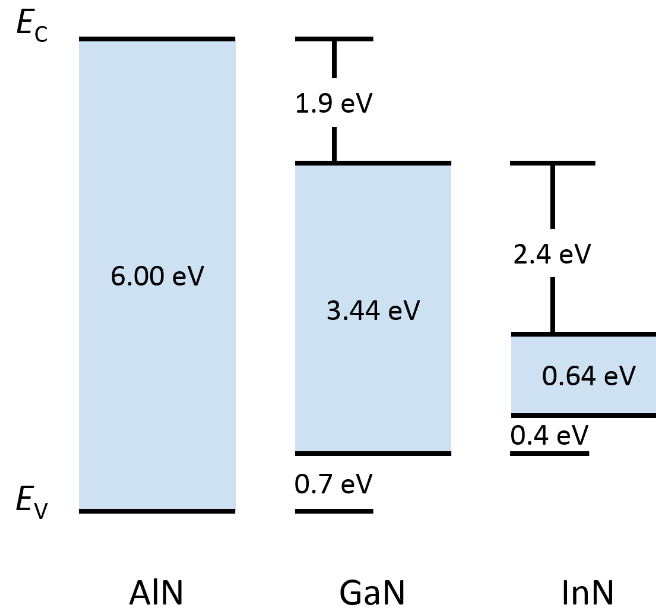

Figure 2.2 – Room-temperature band gap and band alignment of III-nitrides. Values are taken from [11, 13, 14, 20].

For ternary alloys the band offset can be determined by making use of the common anion rule [21, 22]

$$\Delta E^{\mathrm{c}}_{\mathrm{ABN}}(x) = 0.63\left(E^{\mathrm{g}}_{\mathrm{ABN}}(x) - E^{\mathrm{g}}_{\mathrm{ABN}}(0)\right), \tag{2.4}$$

where $E^{\mathrm{g}}_{\mathrm{ABN}}(x)$ is the band gap energy of the ternary alloy.

2.2 Polarization

III-nitrides are pyroelectric materials with internal electric fields in excess of MV cm^{-1}. This is due to their spontaneous and piezoelectric polarizations, which are discussed in the following sections.

Material	P^{sp} (C m^{-2})	e_{31} (C m^{-2})	e_{33} (C m^{-2})	C_{13} (GPa)	C_{33} (GPa)
InN	-0.042	-0.57	0.97	92	224
GaN	-0.034	-0.49	0.73	103	405
AlN	-0.090	-0.60	1.46	108	373

Table 2.2 – Spontaneous polarization P^{sp} and piezoelectric constants of InN, GaN and AlN [12, 23].

2.2.1 Spontaneous polarization

The lack of inversion symmetry along the c-axis of the wurtzite structure leads to the formation of an electrostatic dipole. This gives rise to a macroscopic spontaneous polarization along the c-axis. Spontaneous polarization is present in III-nitrides for the ideal wurtzite structure and is further enhanced due to non-ideality arising from the high ionicity of the bonds. The internal parameter u for III-nitrides given in Tab. 2.1 reflects the non-ideal cation anion bond length along the c-axis. The polarization is defined as the dipole moment per unit volume (C m^{-2}). The magnitude of spontaneous polarization for binary III-nitride compounds (based on *ab initio* calculations) are given in Tab. 2.2. For stronger deviation from ideality (higher ionicity) P_{sp} increases. AlN has therefore the highest spontaneous polarization among the III-nitride compounds. For the ternary alloys (AlGaN, InGaN and InAlN) the spontaneous polarization can be expressed to second order in the composition x as [16, 24]

$$\begin{aligned}
P^{sp}_{\mathrm{Al_xGa_{1-x}N}}(x) &= -0.090x - 0.034(1-x) + 0.021x(1-x), \\
P^{sp}_{\mathrm{In_xGa_{1-x}N}}(x) &= -0.042x - 0.034(1-x) + 0.037x(1-x), \\
P^{sp}_{\mathrm{In_{1-x}Al_xN}}(x) &= -0.090x - 0.042(1-x) + 0.070x(1-x).
\end{aligned} \tag{2.5}$$

Interestingly, linear interpolation (Vegard's law) is not sufficient in describing the spontaneous polarization of alloys. This is due to the nonlinear polarization response to changes in the lattice parameter ($a(x)$) i.e. changes in hydrostatic compression of the binary compounds.

2.2.2 Piezoelectric polarization

In addition to the spontaneous polarization, which is present in bulk III-nitride semiconductors, an additional contribution needs to be taken into account when dealing with heterostructures consisting of several layers exhibiting lattice and thermal expansion coefficient mismatch. The deformation of the lattice due to mismatch leads to a change of the internal lattice parameters which modifies the magnitude of the spontaneous polarization. This can be seen as applying a stress to the relaxed lattice (Fig. 2.3(a)) which in turn changes the a and c lattice parameter (Fig. 2.3(b)).The additional contribution to the total polarization due to strain is called piezoelectric polarization. Piezoelectric polarization for III-nitrides can be

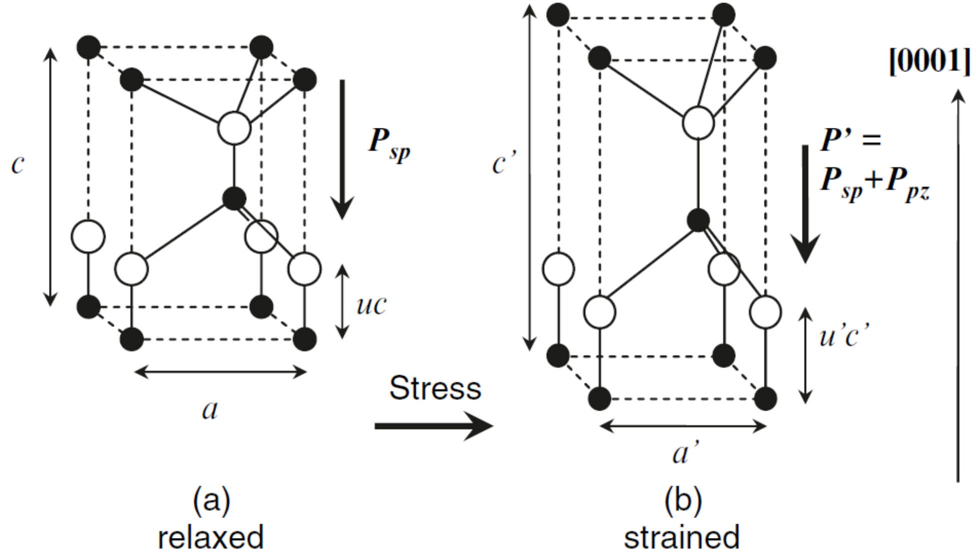

Figure 2.3 – Illustration of the piezoelectric effect. In contrast to the relaxed lattice (a) a deformation of the *in-plane* lattice constant (b) gives rise to piezoelectric polarization along the (0001) direction. Reproduced with modification from [10] and permission from Springer Nature.

expressed phenomenologically as [24]

$$\begin{aligned} P^{\text{pz}}_{\text{AlN}} &= -1.808\varepsilon + 5.624\varepsilon^2 \text{ for } \varepsilon < 0, \\ P^{\text{pz}}_{\text{AlN}} &= -1.808\varepsilon - 7.888\varepsilon^2 \text{ for } \varepsilon > 0, \\ P^{\text{pz}}_{\text{GaN}} &= -0.918\varepsilon + 9.541\varepsilon^2, \\ P^{\text{pz}}_{\text{InN}} &= -1.373\varepsilon + 7.559\varepsilon^2, \end{aligned} \tag{2.6}$$

where ε is the *in-plane* strain of the layer defined as

$$\varepsilon(x) = \frac{a - a_0}{a_0}. \tag{2.7}$$

As expected, the piezoelectric polarization is directly related to the strain state of the layer. For ternary III-nitride alloys, piezoelectric polarization can be expressed as

$$P^{\text{pz}}_{\text{ABN}}(x) = xP^{\text{pz}}_{\text{AN}}\big(\varepsilon(x)\big) + (1-x)P^{\text{pz}}_{\text{BN}}\big(\varepsilon(x)\big). \tag{2.8}$$

In contrast to spontaneous polarization, Vegard's law holds for piezoelectric polarization. This is due to the fact that the non-linearity of P^{pz} is encompassed in the quadratic dependence of the binary polarization as a function of the basal strain (ε) given in Eq. 2.6. In case of pseudomorphic growth, the strain can be directly calculated by inserting the *in-plane* lattice constant $a(x)$ given by Eq. 2.2. For a microscopic understanding of piezoelectric polarization, the impact of lattice-distortion needs to be considered. In the following section, elasticity theory, specifically Hooke's law, will be used to describe the response of the crys-

tal lattice under stress. The lattice distortion is then related to the piezoelectric polarization. Hooke's law states that the applied stress (σ_{ij}) is related to the distortion induced strain (ε_{kl}) by the following equation

$$\sigma_{ij} = \sum_{k,l} C_{ijkl}\varepsilon_{kl}, \tag{2.9}$$

where C_{ijkl} is a fourth-rank tensor describing the elastic stiffness of the material. Due to spatial symmetry of the wurtzite crystal, C_{ijkl} can be reduced to a 6×6 matrix with the following notation: $xx\rightarrow1$, $yy\rightarrow2$, $zz\rightarrow3$, $(yz,zy)\rightarrow4$, $(xz,zx)\rightarrow5$, $(xy,yx)\rightarrow6$. Hence, the tensor can be rewritten as $C_{ijkl} = C_{mn}$ were $i,j,k,l = (x,y,z)$ and $m,n = 1,...,6$, and Hooke's law simplifies to

$$\sigma_i = \sum_j C_{ij}\varepsilon_j, \tag{2.10}$$

where C_{ij} is given by

$$C_{ij} = \begin{pmatrix} C_{11} & C_{12} & C_{13} & 0 & 0 & 0 \\ C_{12} & C_{11} & C_{13} & 0 & 0 & 0 \\ C_{13} & C_{13} & C_{33} & 0 & 0 & 0 \\ 0 & 0 & 0 & C_{44} & 0 & 0 \\ 0 & 0 & 0 & 0 & C_{44} & 0 \\ 0 & 0 & 0 & 0 & 0 & \frac{1}{2}(C_{11}-C_{12}) \end{pmatrix}. \tag{2.11}$$

For III-nitride heterostructures grown along the c-axis, the strain caused by lattice-mismatch of the a parameter and/or a mismatch in thermal expansion coefficient is directed parallel to the substrate. Therefore, no force is applied in the growth direction. The biaxial strain ($\varepsilon_1 = \varepsilon_2$) leads to stresses ($\sigma_1 = \sigma_2$ and $\sigma_3 = 0$). The relation between the strain along the c-axis (ε_3) and *in-plane* (ε_1) can be derived by using Eq. 2.9, which results in

$$\varepsilon_3 = -2\frac{C_{13}}{C_{33}}\varepsilon_1, \tag{2.12}$$

where ε_3 and ε_1 are determined by the relative change of the lattice constants with respect to the relaxed lattice constants provided in Tab. 2.1.

$$\begin{aligned} \varepsilon_1 &= \frac{a-a_0}{a_0}, \\ \varepsilon_3 &= \frac{c-c_0}{c_0}. \end{aligned} \tag{2.13}$$

Finally, the piezoelectric polarization can be expressed by the following equation which is simplified due to the hexagonal wurtzite symmetry as

$$\begin{aligned} P_z^{\mathrm{pz}} &= e_{31}\varepsilon_1 + e_{31}\varepsilon_2 + e_{33}\varepsilon_3, \\ &= 2\left(e_{31} - e_{33}\frac{C_{13}}{C_{33}}\right)\varepsilon_1, \end{aligned} \tag{2.14}$$

where e_{31} and e_{33} are piezoelectric constants provided in Tab. 2.2. The total polarization of the layer can then be described as the sum of both the spontaneous polarization and the contribution due to piezoelectric effects as

$$P_{\mathrm{ABN}} = P^{\mathrm{pz}}_{\mathrm{ABN}} + P^{\mathrm{sp}}_{\mathrm{ABN}}. \tag{2.15}$$

In case of epitaxially grown III-nitride multilayers (heterostructures), the total polarization changes at each interface leading to a discontinuity. To preserve the continuity of the normal component of the displacement field, Gauss' law states that such an abrupt change in electric field (between layers A and B) induces a fixed sheet charge density (σ) at the interface which can be expressed as

$$\sigma = \mathbf{n} \cdot (\mathbf{P}_{\mathrm{A}} - \mathbf{P}_{\mathrm{B}}), \tag{2.16}$$

where $\mathbf{P}_{\mathrm{A}}$ and $\mathbf{P}_{\mathrm{B}}$ are the total polarizations of the layers A and B across the interface and $\mathbf{n}$ is the normal vector to the interface. For III-nitrides, the built-in polarization field is along the (0001) direction. Hence, for growth along the (0001) direction, $\mathbf{P}$ and $\mathbf{n}$ are parallel to each other.
The sheet density for a layer at a free surface is given by

$$\sigma_{\mathrm{ABN}} = P_{\mathrm{ABN}} = P^{\mathrm{pz}}_{\mathrm{ABN}} + P^{\mathrm{sp}}_{\mathrm{ABN}}, \tag{2.17}$$

and, in general for interfaces between two compounds ABN and CDN, it is expressed by

$$\begin{aligned} \sigma_{\mathrm{ABN/CDN}} &= P_{\mathrm{CDN}} - P_{\mathrm{ABN}} \\ &= \left(P^{\mathrm{pz}}_{\mathrm{CDN}} + P^{\mathrm{sp}}_{\mathrm{CDN}}\right) - \left(P^{\mathrm{pz}}_{\mathrm{ABN}} + P^{\mathrm{sp}}_{\mathrm{ABN}}\right), \end{aligned} \tag{2.18}$$

where the sign depends on the scalar product described in Eq. 2.16. For the example of the Ga-face AlN/GaN interface, the polarization-induced charge is positive and reaches a value of $\sim 7\times10^{13}$ cm^{-2}. Free electrons are attracted to the positively charged interfaces. Hence, electron concentrations comparable to the positive charge density can accumulate without the need for modulation doping as is the case in GaAs heterostructures. At the interface, electrons will be free to move within the plane and are strongly confined in the (0001) direction leading to the formation of a two-dimensional electron gas (2DEG), which will be discussed in the following section.

2.3 III-nitride two-dimensional electron gases

As discussed in the previous section, the positive charge at the interface between a large band gap III-nitride material such as AlGaN and GaN attracts free (mobile) electrons which are then accumulated at the interface. Due to the large conduction band offset between AlGaN and GaN, the electrons are strongly confined at the interface in a (approximately) triangular well along the (0001) direction and free to move within the plane in two dimensions (hence

the name two-dimensional electron gas). The conduction band diagram and sheet charge density of such a heterostructure is illustrated in Fig. 2.4. The free electrons accumulating in the 2DEG originate from donor-like surface states [25, 26]. Unsaturated bonds (dangling bonds) at free semiconductor surfaces give rise to electronic states within the band gap. The surface states, which are above the Fermi level, will therefore be ionized, supplying a large density of electrons. The exact distribution and type of surface states responsible for the electron supply to the 2DEG are to this date not fully understood [27]. Within a heterostructure containing a 2DEG (as shown in Fig. 2.4), four main charge components are present: (i) polarization charge at the surface (σ_{surf}), (ii) polarization charge at the interface (σ_{int}), (iii) 2DEG density σ_{2DEG} and finally the donor-like surface states which give rise to a positive charge once ionized (σ_{comp}). In order to determine the 2DEG density, Schrödinger-Poisson

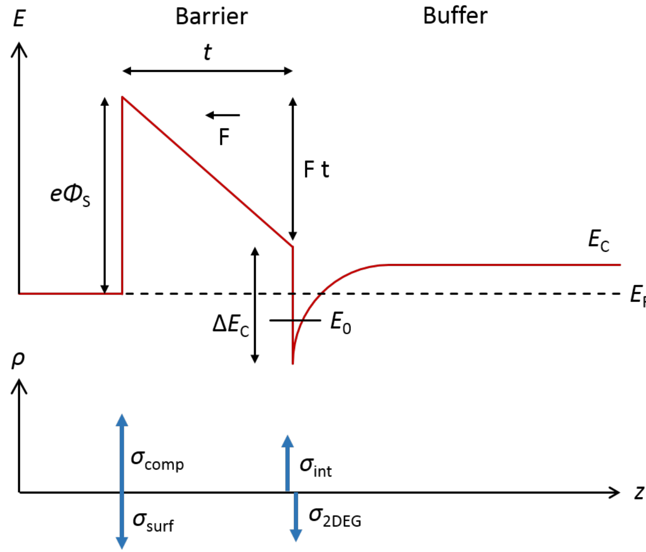

Figure 2.4 – Conduction band diagram (top) and sheet charge density distribution (bottom) for a III-nitride heterostructure consisting of a barrier (e.g. AlGaN, InAlN or AlN) grown on a GaN buffer.

calculations are usually performed self-consistently in the effective mass approximation to give a numerical solution. However, a simplified model will be described in the following section in order to provide some physical insight. The heterostructure is assumed to be a barrier (e.g. AlGaN) grown on a GaN buffer, as illustrated in Fig. 2.4, with the 2DEG confined within a triangular quantum well. The Fermi level is pinned at the position of donor-like surface states below the conduction band edge at the AlGaN surface. This is due to the high density surface states giving rise to a surface barrier height of value $e\Phi_{\mathrm{S}}$. From the energy diagram in Fig. 2.4, it follows that

$$e\Phi_{\mathrm{S}}(x) - \Delta E_{\mathrm{c}} - Ft + E_0 + (E_{\mathrm{F}} - E_0) = 0, \tag{2.19}$$

where ΔE_c is the band discontinuity between the barrier and the buffer, F is the electric field in the barrier (with thickness t) given by

$$F = \frac{e(\sigma - n_s)}{\epsilon_0 \epsilon}, \tag{2.20}$$

and

$$E_F - E_0 = \frac{\pi \hbar^2}{m^\star} n_s, \tag{2.21}$$

where it is assumed that only one subband of the triangular quantum well is occupied with a ground state energy E_0 as a function of 2DEG electron density n_s

$$E_0(n_s) = \left(\frac{9\pi\hbar e^2 n_s}{8\varepsilon_0 \varepsilon \sqrt{8m^\star}} \right)^{2/3}, \tag{2.22}$$

where $\hbar$ is the reduced Planck's constant, e is the elementary charge, ε_0 is the permittivity of vacuum, ε is the relative dielectric constant and $m^\star$ is the electron effective mass. E_F is set as the zero in energy in the calculations. The 2DEG carrier density n_s can be determined from the roots of Eq. 2.19. The carrier density is mainly determined by two parameters, (i) the polarization-induced charge σ at the interface and (ii) the barrier thickness (t). Alloy composition and strain of the barrier strongly affect the spontaneous and piezoelectric polarizations. Furthermore, with increasing barrier thickness, the 2DEG density increases. In the following section, various barrier types for the formation of III-nitride 2DEGs will be discussed.

AlGaN/GaN

In 1992, Khan *et al.* [2] reported on the first 2DEG based on III-nitrides using a AlGaN/GaN heterostructure. Over the past two decades, the AlGaN/GaN system has been extensively studied and is among the best understood III-nitride HEMT(s). The Al content of the AlGaN barrier strongly affects the sheet charge density at the interface and hence the 2DEG density, as discussed in the previous section. For high Al content the carrier density increases due to the large spontaneous polarization of AlN. Furthermore, the barrier thickness plays a crucial role for the 2DEG density. The carrier density increases with barrier thickness and saturates as the built-in field flattens fully compensating the positive sheet charge at the interface. Hence, larger barrier thicknesses seem desirable. On the other hand the AlGaN barrier does not fulfill lattice-matching conditions with GaN, which can be seen in Fig. 2.1. AlGaN grown on GaN remains under tensile strain for any composition and increases with the layer thickness. Hence, above a critical thickness the strain is released by the introduction of dislocations and cracks, limiting the barrier thickness. Furthermore, the critical thickness decreases drastically with increasing Al content of the barrier. Therefore, there is a trade-off between the thickness and the Al composition of the AlGaN barrier. Typical AlGaN/GaN heterostructures used in HEMTs have an Al content of ~ 20-30 % and a thickness of 20 to 30 nm leading

to 2DEG carrier densities of 0.5 to 1×10^{13} cm^{-2} and an electron mobility of 1000 to 2000 cm^2 V^{-1} s^{-1} [28–30]. A thin AlN spacer (1-2 nm) is usually inserted between the AlGaN barrier and the GaN buffer in order to prevent alloy disorder scattering of the 2DEG wave function in the AlGaN barrier. As will be discussed in Chap. 6, alloy disorder scattering is much stronger in III-nitrides compared to conventional III-V semiconductors (e.g. GaAs).

InAlN/GaN

InAlN is an interesting barrier material since it can be grown lattice-matched to GaN for an indium content of ~ 17 %. Furthermore, the spontaneous polarization-mismatch is 2 to 3 times larger than for typical low Al content AlGaN barriers. InAlN/GaN heterostructures were first proposed by Kuzmík in 2001 [3] and high quality 2DEGs were achieved by Gonschorek *et al.* in 2006 [31]. The large spontaneous polarization of InAlN enables 2DEG carrier densities well above the ones possible with AlGaN reaching values typically ~ 2×10^{13} cm^{-2} while keeping the barrier thickness well below 10 nm. For comparison, AlGaN/GaN heterostructures with similar barrier thicknesses give rise to a 2DEG density < 0.5×10^{13} cm^{-2}. The high carrier density at low barrier thicknesses has two main advantages for electronic devices. (i) The high carrier concentration enables current densities as high as 3 A mm^{-1} [4], which is important for transistors providing high power densities. (ii) The sub-10 nm barrier thickness of InAlN barriers allows for easier downscaling of the transistor geometry with respect to AlGaN. Shorter gate lengths are particularly desirable for transistors operating at high frequencies. Despite the extraordinary properties of InAlN barriers, there are two main issues limiting their potential for high frequency applications, (i) gate leakage currents and (ii) short channel effects. In this thesis, InAlN/GaN heterostructures were used as a workhorse to study alloy disorder (Chap. 6) and for the demonstration of MOVPE regrown ohmic contacts (Chap. 7).

AlN/GaN

AlN barrier HEMTs grown on GaN buffers were first reported in the early 2000s [9, 32, 33]. The large polarization-mismatch (both spontaneous and piezoelectric) between GaN and AlN leads to very high positive sheet charge densities at the interface, which in turn gives rise to high 2DEG carrier densities which are theoretically as high as ~ 7×10^{13} cm^{-2} [10] while keeping the barriers ultra thin (~ 2-6 nm), as reported by Cao *et al.* [34]. Furthermore, the binary system of AlN on GaN eliminates alloy disorder scattering. High electron mobilities (~ 2000 cm^2 V^{-1} s^{-1}) combined with the high 2DEG densities give rise to the record low sheet resistances 150-170 Ω/sq reported for any III-nitride based HEMTs [35]. Furthermore, the large conduction band offset between AlN and GaN prevents the real-space transfer of carriers from channel into barrier. One of the main challenges in the growth of AlN barriers on relaxed GaN buffers is the tensile strain. Above the critical thickness of AlN on GaN, strain relaxation leads to the formation of cracks and dislocations, which in turn deteriorate the electron mobility and also reduce the 2DEG density due to the loss of piezoelectric polariza-

tion. Nevertheless, careful optimization has enabled very impressive device performance in the past two decades [36–39]. Interestingly, most reported AlN barrier HEMTs were grown by plasma-assisted molecular beam epitaxy (PA-MBE), with only few reports using the industrially more scalable MOVPE method [40, 41]. This is possibly due to the much lower growth temperatures used in PA-MBE compared to MOVPE. In Chap. 5 the instability of the AlN/GaN interface will be discussed in more detail.

AlN/GaN/AlN

AlN/GaN/AlN heterostructures make use of the AlN barrier described in the previous section while having two main additional benefits, (i) a thin GaN channel allows for strong confinement and control of the 2DEG, preventing leakage of carriers into the buffer and (ii) the AlN substrate is an excellent thermal conductor (300 W m^{-1} K^{-1}) [7] and electrical insulator (6.00 eV) which allows for efficient heat management and low buffer leakage, respectively. Over the past decade, several reports have been given on the performance of AlN/GaN/AlN heterostructures [42–44] and in general thin GaN channels grown on AlN [45–48]. One peculiar issue common to all these reports is a poor 2DEG electron mobility (< 1000 cm^2 V^{-1} s^{-1}) while having a carrier density well above 1×10^{13} cm^{-2}. In Chap. 5 of this thesis, the origin for the observed low electron mobility will be discussed.

N-polar HEMTs

All the heterostructures discussed so far were grown along the Ga-face (0001) direction. For the sake of completeness, heterostructures grown along the N-face (N-polar) direction should also be mentioned. Specifically over the last decade, remarkable device performance has been reported for these structures [49–53]. One of the main advantages of N-polar HEMTs is, that electrical contact is made to GaN compared to the much larger band gap barriers in Ga-polar structures. This allows for ultra low contact resistances (0.027 Ω mm [54]) and outstanding device performance [51, 52].

2.4 Strain relaxation and critical thickness

The epitaxial growth of heterostructures with layers consisting of different lattice constants gives rise to strain and can lead to the introduction of misfit dislocations which in turn severely deteriorate the performance of electronic and optoelectronic devices. In the case of electronics, dislocations create conducting paths, which can lead to parasitic gate leakage currents [8]. Furthermore, dislocations have been shown to reduce the lifetime of blue laser diodes [55, 56]. Hence, it is important to understand and to be able to control the strain state of layers in order to reduce the introduction of dislocations to a minimum. In the following section, strain relaxation mechanisms in general, and in particular for III-nitride heterostructures, will be discussed.

The lattice-mismatch between the growing layer and the substrate is an important parameter and is given by

$$f = \frac{a - a_\mathrm{s}}{a_\mathrm{s}}, \tag{2.23}$$

where a and a_s are the lattice constant of the growing epilayer and substrate, respectively. In Fig. 2.5(a) a substrate (green) and layer (blue) with differing *in-plane* lattice constants are illustrated. As the layer is epitaxially grown, the *in-plane* lattice constant is reduced and matched to the one of the substrate. The layer is said to be compressively strained (Fig. 2.5(b)). With increasing thickness of the layer, the strain and hence the elastic energy of the surface increases. The accumulated strain can generally be relieved in two ways: (i) Modulation of the free surface by roughening (elastic strain relaxation) or (ii) by the introduction of misfit dislocations (plastic strain relaxation), which is illustrated in Fig. 2.5(c). In the following section, only the latter case will be discussed. At a critical thickness h_c , the creation of misfit dislocations becomes energetically more favorable than a further increase of the accumulated strain in the layer. In the next section, various critical thickness models will be introduced which have been developed over the past 70 years.

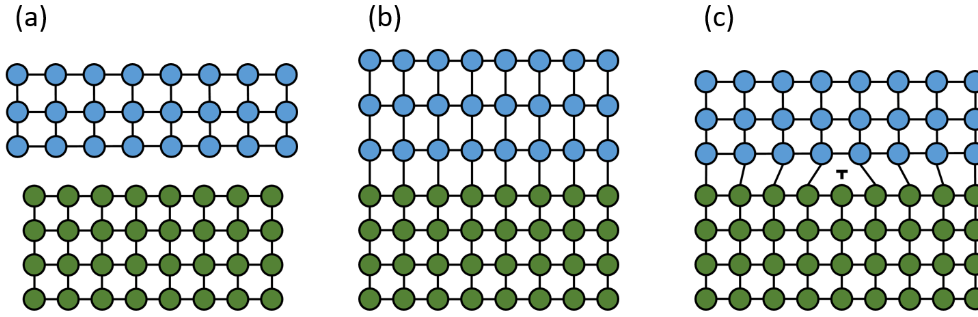

Figure 2.5 – Illustration of substrate and layer lattice where (a) the lattices are relaxed and (b) the layer is grown pseudomorphically on the substrate, giving rise to compressive strain. (c) Strain relaxation by the introduction of a dislocation marked with ⊤.

2.4.1 Critical thickness

In 1949, Frank and van der Merwe [57, 58] developed a theory for the determination of the critical thickness based on energy minimization. The layer thickness (h_c) at which the elastic energy matches the energy for creating misfit dislocations was thereby expressed by

$$h_\mathrm{c} = \frac{b}{8\pi f}\left(\frac{1-\nu\cos^2\beta}{(1+\nu)\cos\lambda}\right)\left(\ln\left(\frac{h_\mathrm{c}}{b}\right)+1\right), \tag{2.24}$$

where b is the magnitude of the misfit dislocation Burgers vector, β is the angle between b and the dislocation line and λ is the angle between b and the direction normal to the dislocation line. The energy minimization used in this theory implies that the critical thickness is

determined under equilibrium conditions.
Matthews and Blakeslee [59, 60] formulated a theory based on a force balance model instead of energy. The layer thickness at which the elastic-strain induced force on the dislocation line balances the internal tension of the dislocation line was defined as the critical thickness. The theory determined the critical thickness at which pre-existing dislocations in the layer could be bent. The critical thickness is inversely proportional to the lattice-mismatch f for both theories. For large lattice-mismatch, the surface elastic energy increased and reduces the critical thickness. As expected, the two models are equivalent and give rise to the same critical thickness since both describe near-equilibrium conditions. Surprisingly, experimental reports clearly demonstrated that pseudomorphic layers with thicknesses well beyond h_c (predicted by Eq. 2.24) could be grown [61–65]. This is due to the fact that the layers are in a metastable state and cannot be described by a model under equilibrium conditions. Kinetic barriers defined by the applied growth conditions (e.g. temperature, growth rate and initial dislocation density) hinder the nucleation and motion of dislocations for efficient strain relief. People and Bean [66] and Dodson and Tsao [67] attempted to describe the kinetic limitation by a semi-empirical model where the driving force for the motion of dislocations is the excess stress within the layer. Furthermore, the multiplication and glide of dislocations in strain fields was considered. The evolution of the strain relaxation as a function of time $\gamma(t)$ can be expressed in the Dodson and Tsao model as

$$\frac{d\gamma(t)}{dt} = C\mu_s^2 \left(f_0 - \gamma(t) - r(h)\right)^2 \left(\gamma(t) + \gamma_0\right), \tag{2.25}$$

where C is a thermally activated term for the motion of dislocations, μ_s is the shear modulus, $r(h)$ the thickness-dependent strain, γ_0 is the relaxation due to pre-existing dislocations and ν is Poisson's ratio. The model can be used to qualitatively understand the evolution of strain relaxation as a function of layer thickness/time. Fischer *et al.* [68] developed a model for the Ge_xSi_{1-x}/Si system of metastable heterostructures in which the critical thickness is thermally activated. Furthermore, the elastic interaction of dislocations is implemented. The critical thickness can be expressed by

$$h_c = \frac{b\cos\lambda}{2f}\left(1 + \frac{1-\nu/4}{4\pi(1+\nu)\cos(\lambda)^2}\right)\ln\left(\frac{h_c}{b}\right), \tag{2.26}$$

where b is the magnitude of the dislocation Burgers vector, f the lattice-mismatch, ν the Poisson's ratio and λ the angle between the Burgers vector and the direction in the interface normal to the dislocation line. The critical thickness calculated by Eq. 2.26 in the metastable state can be orders of magnitude larger than the value obtained by equilibrium theory described by Eq. 2.24.
In the case of III-nitrides, many reports over the last 20 years discuss the critical thickness and the evolution of strain relaxation as a function of layer thickness. Elastic strain relaxation [69, 70] and plastic strain relaxation were investigated for AlN/GaN [71–75], AlGaN/GaN [76] and InGaN/GaN heterostructures [77]. In the case of AlN/GaN, only partial strain relaxation was observed whereas for InGaN/GaN and AlGaN/GaN fully coherent layers were reported,

suggesting kinetic limitations leading to a metastable state. The calculated critical thickness for GaN on AlN ranges between 3 and 20 MLs depending on the applied model [57, 68, 78]. Furthermore, experimental values range between 11 and 12 MLs [72, 79] far from the near-equilibrium critical thickness. Kinetic limitations for efficient strain relaxation have been suggested to be due to a large force necessary to move dislocations within the atomic plane (Peierls force), which lowers the dislocation mobility in III-nitrides [80]. In Chap. 4, the strain relaxation of GaN on AlN and the impact of growth temperature and initial dislocation density will be discussed in detail.

2.4.2 Dislocations

As discussed in the previous section, above the critical thickness for plastic strain relaxation, misfit dislocations are introduced in order to relieve the strain. Furthermore, it has been established that the mobility and nucleation of dislocations are thermally activated [81] with a characteristic activation energy of 2 to 2.7 eV for GaN [82]. High temperatures increase the mobility and multiplication of dislocations enabling the strain relaxation process. The dislocation density for III-nitrides grown on foreign substrates generally improves with the thickness of the layer and ranges between 10^{10} and 10^{7} cm^{-2}. Interestingly, the dislocation density at the initial stages of growth of GaN on AlN has been shown to be as high as 7×10^{11} cm^{-2} [83]. Such high dislocation densities have a detrimental effect on the electronic properties in III-nitride based 2DEG, as discussed in the following section.

Dislocation scattering

Edge-type threading dislocations in III-nitride heterostructures are observed to be oriented along the (0001) growth direction [84] with dangling bonds at every lattice constant along the axis. The dangling bonds are electrically charged and act as Coulomb scattering centers [85]. In the presence of a 2DEG, the charged dislocation lines pierce the 2D plane and give rise to a charged impurity-like scattering site for electrons, as illustrated in Fig. 2.6(a). The two-dimensional scattering term for charged dislocations can be expressed by [86]

$$\mu_{\mathrm{disl}} = 43365\left(\frac{10^{8}\mathrm{cm}^{-2}}{N_{\mathrm{disl}}}\right)\left(\frac{n_s}{10^{12}\mathrm{cm}^{-2}}\right)^{1.34}\left(\frac{1}{f_0^2}\right), \tag{2.27}$$

where N_{disl} is the density of dislocations, n_{s} the 2DEG density and f_0 the fraction of charged occupied states within the energy gap. The electron mobility of 2DEGs is strongly affected both at room-temperature and low temperature by the density of dislocations [87, 88]. However, at sufficiently high n_{s} the charged dislocations can be effectively screened and the electron mobility is not affected. Furthermore, dislocations can give rise to a second scattering mechanism due to the strain distribution around the dislocation core [89], as illustrated in Fig. 2.6. In the presence of high dislocation densities, it is therefore challenging to distinguish between the two scattering mechanisms.

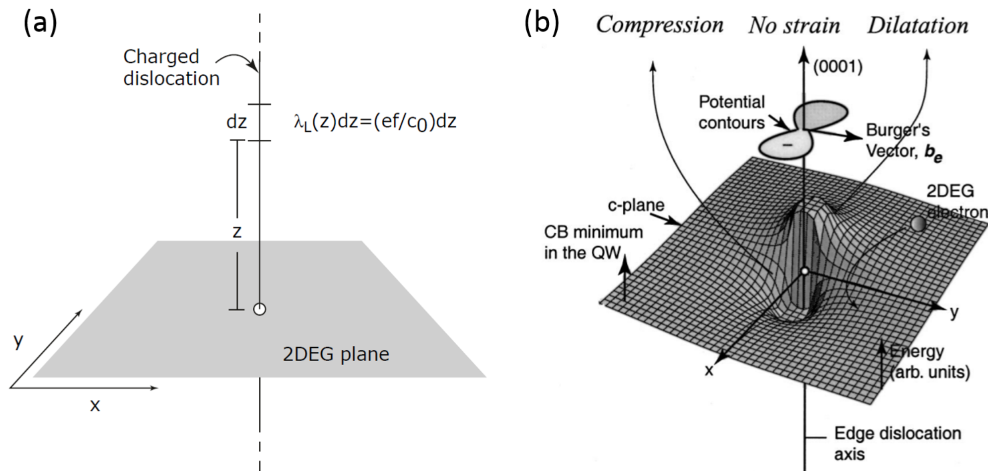

Figure 2.6 – (a) Illustration of a charged threading dislocation line piercing a 2DEG. (b) Two-dimensional conduction band profile fluctuation caused by strain fields around an edge dislocation. Reproduced with modification from [10] with permission from Springer Nature.

In Chap. 5, the impact of high dislocation densities on the electron mobility of AlN/GaN 2DEG heterostructures will be discussed.

3 Experimental method

In the first section of this chapter, growth methods for III-nitride heterostructures used during this thesis are described. In the subsequent parts, the material, optical and electrical characterization methods are discussed.

3.1 Epitaxial growth

Epitaxial growth is the deposition of a growing layer, the crystal structure of which is imposed by the substrate. In the case of homoepitaxy, the grown layer and the substrate are made out of the same material and the structural properties strongly depends on the kinetics of growth i.e. the surface diffusion length for atoms to find the most appropriate site at the crystal surface to be incorporated. On the other hand, heteroepitaxy involves two materials with different lattice constants. In this case, the lattice-mismatch is an additional crucial parameter which determines the growth. Historically, three growth modes are distinguished in heteroepitaxy: (i) Frank–Van der Merwe (FM) (ii) Stranski–Krastanov (SK) and (iii) Volmer–Weber (VW) as illustrated in Fig. 3.1. The growth mode depends on the relative magnitude of the

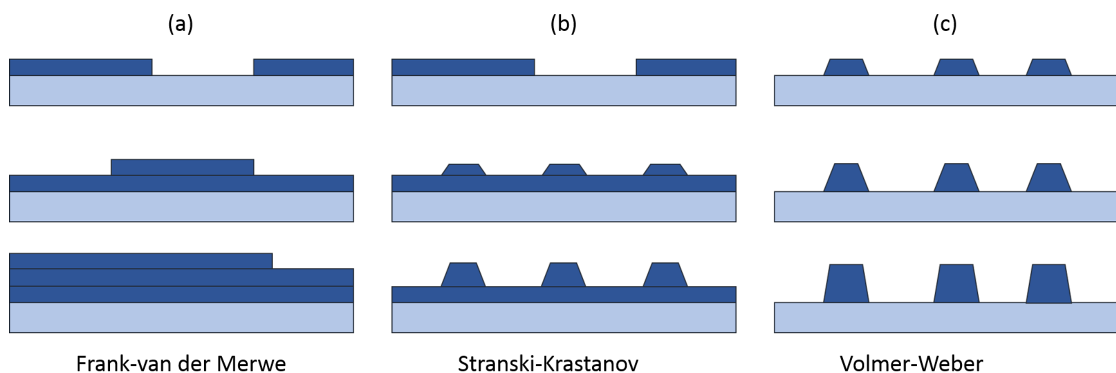

Figure 3.1 – Illustration of growth modes in heteroepitaxy.

surface energies γ_s, γ_l and $\gamma_i(h)$ corresponding to the substrate, layer and interface, respec-

tively. The substrate and layer energies assume a semi-infinite crystal, whereas the interface energy contains the strain energy and hence depends on the layer thickness h [90]. In the FM growth mode (Fig. 3.1(a)) the layer is grown on the substrate layer-by-layer. This occurs when the surface energy of the substrate is larger than the layer and the interface. The condition is given as

$$\Delta\gamma = \gamma_l + \gamma_i(h) - \gamma_s \leq 0, \tag{3.1}$$

for all thicknesses (h) and the layer remains 2D, which is typical for material systems with small lattice-mismatch (< 1 %). For large layer thicknesses, the strain energy increases. The accumulated strain is generally released in two ways: (i) by the introduction of misfit dislocations (plastic relaxation), in which case the layer remains 2D or (ii) by a surface deformation (elastic relaxation) [91]. In the case where Eq. 3.1 remains valid for the FM growth mode only up to a certain thickness, the SK growth mode (Fig. 3.1(b)) becomes energetically favorable. The growth continues by introducing coherent 3D islands on the 2D layer (wetting layer) which is typically only a few ML thick. The VM growth mode (Fig. 3.1(c)) corresponds to the case where the 3D islands directly form on the substrate without a wetting layer (the condition in Eq. 3.1 is not fulfilled).
The evolution of strain relaxation for GaN grown on AlN in the FM regime is discussed in Chap. 4. The introduction of dislocations above the critical thickness is shown to be strongly temperature dependent, which suggests that, in addition to the equilibrium growth conditions assumed in the FM growth mode, the surface kinetics also needs to be taken into account. The introduction of misfit dislocations in the initial stages of growth for GaN on AlN is identified as a possible origin for the low electron mobility in thin GaN channel 2DEGs grown on AlN (Chap. 5). The impact of alloy disorder on the electronic and optical properties of InGaN channel 2DEGs is investigated. Furthermore, parasitic incorporation of Ga atoms for specific reactor configurations are discussed in Chap. 6. The growth of highly Si-doped GaN at low temperature was investigated for regrown ohmic contacts in HEMTs in Chap. 7.
The growths were performed both by molecular beam epitaxy (MBE) and metalorganic vapor phase epitaxy (MOVPE), the principles of which will be discussed in the following sections.

3.1.1 Molecular beam epitaxy

MBE is a thin film deposition process which involves the reaction of one or more molecular beams with a crystalline surface in an ultra-high vacuum environment. The technique was developed by Cho and Arthur at Bell Telephone Laboratories in the late 1960s [92] and is nowadays widely used for the manufacturing of semiconductor devices such as high electron mobility transistors. Furthermore, the high purity crystalline films achievable by MBE enabled fundamental physical discoveries such as the fractional quantum Hall effect [93].
In Fig. 3.2 the main components of a MBE-system are illustrated. The ultra-high vacuum within the MBE-chamber is achieved by turbomolecular and/or ionic pumps resulting in a base-pressure of 10^{-8} to 10^{-10} mbar. Due to the low chamber pressure, the mean free path for

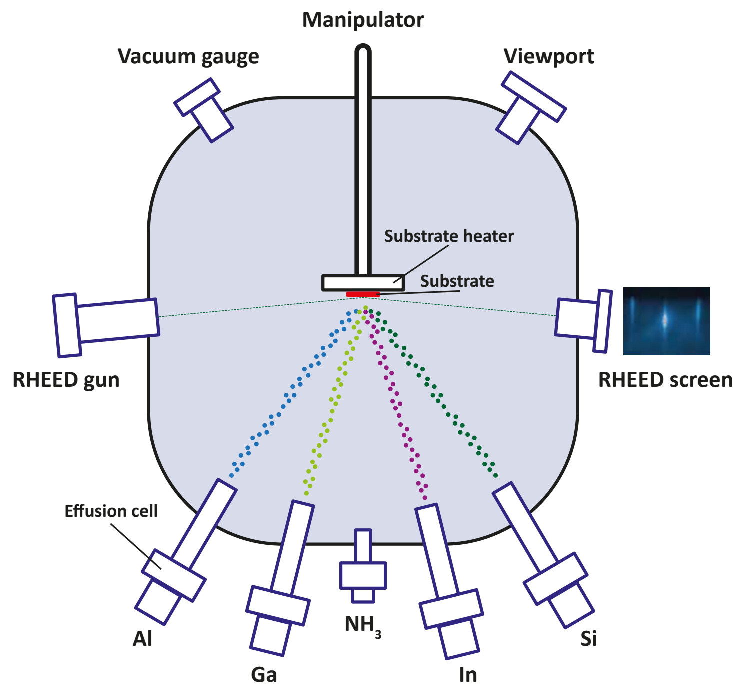

Figure 3.2 – Schematics of a NH_3-MBE system.

the molecular beams is longer than the distance between the cells and the substrate. Hence, the molecules reach the substrate without interacting with each other or gaseous molecules present in the chamber. For the growth of III-nitride layers, group III elements are supplied by solid sources of Al, Ga and In, which are placed in effusion evaporators (Knudsen cells). The cells consist of three main parts. (i) Heating filaments, which are used to melt the solid sources with a high temperature control. The cell temperature determines the beam-equivalent pressure (flux) of the molecular beam and hence the amount of material reaching the substrate. (ii) Pyrolytic boron nitride crucible which contains the ultra pure Ga, Al and In pellets. Boron nitide is used due its chemical inertness, low outgassing and thermal stability. (iii) A computer-controlled shutter allows for precise opening and closing of the cells. The active nitrogen is supplied either by NH_3 or a nitrogen plasma. In the case of NH_3-MBE, the NH_3 is thermally cracked at the growing surface for a temperature starting at 450 °C and reaches a maximum efficiency of only 3.8 % at 700 °C [94]. This is one of the main reasons why high NH_3 overpressures are needed for the growth of III-nitrides both by NH_3-MBE and MOVPE. On the other hand, plasma-assisted MBE (PA-MBE) does not require thermal cracking, since the active nitrogen is produced by radio-frequency electron cyclotron resonance excitation. Consequently, growth temperatures for PA-MBE are usually 200 °C lower than in NH_3-MBE. Moreover, the growth by NH_3-MBE occurs under N-rich rich conditions whereas PA-MBE is performed under metal-rich growth conditions.

As a cell shutter is opened, the elements leave the cells as a beam and condensate on the sample surface, which has a lower temperature than the cell. The atoms move by hopping over the crystal surface and either find a bonding site or they desorb (in MBE the sticking

coefficient is usually 1). The hopping and desorption is thermally activated and is therefore governed by temperature. The sample temperature is controlled by resistive heating of a graphite filament which then transfers the heat to the sample by irradiation absorption. For transparent substrates (such as sapphire) a 1 μm thick Mo layer needs to be deposited on the backside of the wafers in order to enable absorption and hence heating. The sample temperature is measured both by using a pyrometer and a thermocouple. The growth rate is measured in two ways, (i) reflection high-energy electron diffraction (RHEED), which will be discussed in detail in the following section, and (ii) reflectivity measurements by using a red laser diode. The MBE-system used for the epitaxial growths described in this thesis was

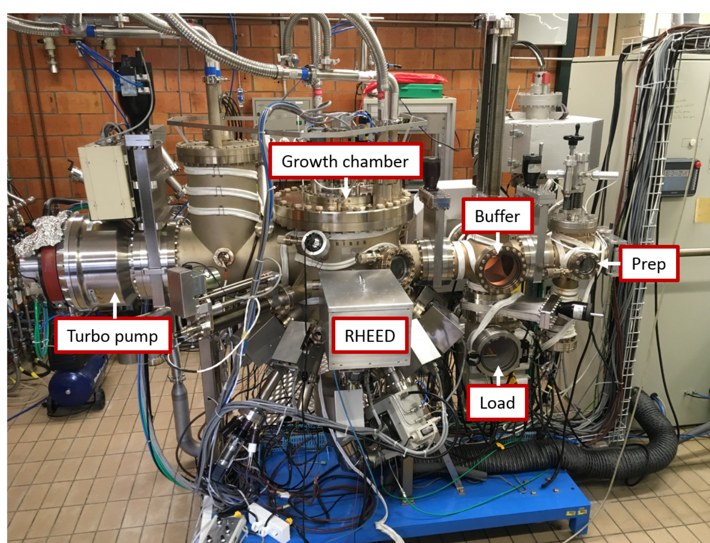

Figure 3.3 – Picture of the MBE-system used for the growths in this thesis.

a Riber compact 21, as shown in Fig. 3.3. The samples were introduced into the preparation chamber prior to growth in order to outgas both sample and the Mo holder. The samples were outgassed at 600 °C usually for several hours until the base pressure of the preparation chamber dropped below 5×10^{-9} mbar. The samples were stored in a cassette in the buffer chamber. Cryogenically cooled panels within the growth chamber are used to remove residual impurities, where the cooling is performed with a liquid nitrogen line (77 K). Excess NH_3 freezes at 196 K on the panels. The cryopanels need to be periodically warmed up (in a controlled manner) in order to prevent built-up of NH_3 in the chamber. This process is called regeneration and is done usually once a week depending on the amount of NH_3 used.

3.1.2 Metalorganic vapor phase epitaxy

MOVPE is a chemical vapor deposition technique invented by Harold M. Manasevit and W. I. Simpson in 1968 [95]. In contrast to MBE, growth by MOVPE occurs by chemical reactions. Furthermore the growth occurs in the gas phase and not in a vacuum, with typical chamber pressures between 50 and 200 mbar. The basic principle of a MOVPE system is illustrated in

Fig. 3.4. Metalorganic precursors are transported with a carrier gas (usually N_2 or H_2) to the

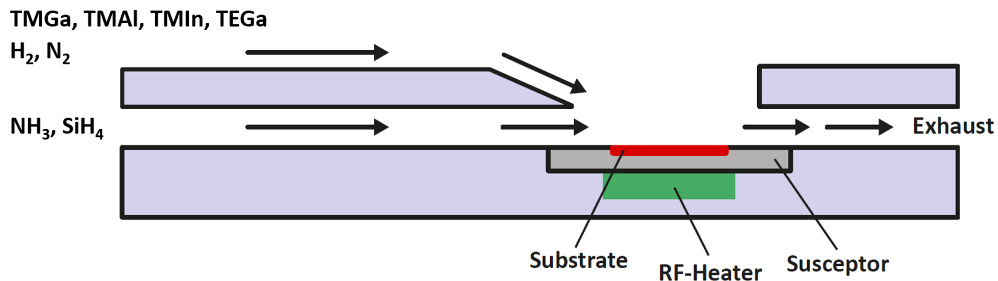

Figure 3.4 – Schematic of a horizontal MOVPE system.

reactor, where they decompose by pyrolysis and are adsorbed on the sample surface. The required temperature for decomposition of metalorganic compounds increases with the bond strength of the specific precursor. The more carbon atoms attach to the central metal atom, the weaker the bond and hence the lower the temperatures needed for pyrolysis. For the growth of III-nitrides by MOVPE the group-III precursors used for Ga, Al and In are trimethylgallium (TMGa, $Ga(CH_3)_3$), triethylgallium (TEGa, $Ga(C_2H_5)_3$), trimethylaluminum (TMAl, $Al_2(CH_3)_6$) and trimethylindium (TMIn, $In(CH_3)_3$), respectively. Furthermore, $n-$ and p-type doping are achieved by the introduction of SiH_4 and Cp_2Mg, respectively. The group-III precursors are introduced into the reactor separated from the NH_3 in order to prevent parasitic reactions away from the sample surface. This is achieved in horizontal reactors (illustrated in Fig. 3.4) by using a quartz plate separating the flow of the metalorganics (which is laminar) from the NH_3. The precursors are usually in a liquid or solid phase which are transported to the reactor by using a carrier gas (N_2 or H_2). This is achieved by placing the metalorganics in bubblers where a saturated vapor forms above the metalorganic liquid. A thermostatic bath within the bubbler system keeps the metalorganic vapor pressure constant. Carrier gases are injected into the bubblers which then carry away metalorganics to the growth chamber at a fixed concentration. The substrate temperature is controlled with a RF-heater and measured with a pyrometer. The growth temperatures used in III-nitride MOVPE are usually higher (700 to 1200 °C) than in MBE due to the presence of metalorganics that require high temperatures for decomposition and to avoid carbon contamination. Growth by MOVPE is generally performed under N-rich growth conditions. The samples are placed on a graphite susceptor which can withstand high temperatures and is chemically inert. The process of MOVPE growth can be described by the following stages, (i) the precursors are transported to the sample surface, (ii) the metalorganic compounds and NH_3 decompose by pyrolysis allowing the metal atoms and nitrogen to be adsorbed on the sample surface, (iii) surface kinetics of atoms and incorporation in to the crystal, and (iv) the desorption and removal of reaction by-products which are then transported to the exhaust.
In this thesis, a horizontal Aixtron 200/4 RF-S MOVPE reactor (shown in Fig. 3.5) was used for the growth of InAlN-based HEMTs, InGaN channels and the regrowth of n^{++} ohmic contacts.

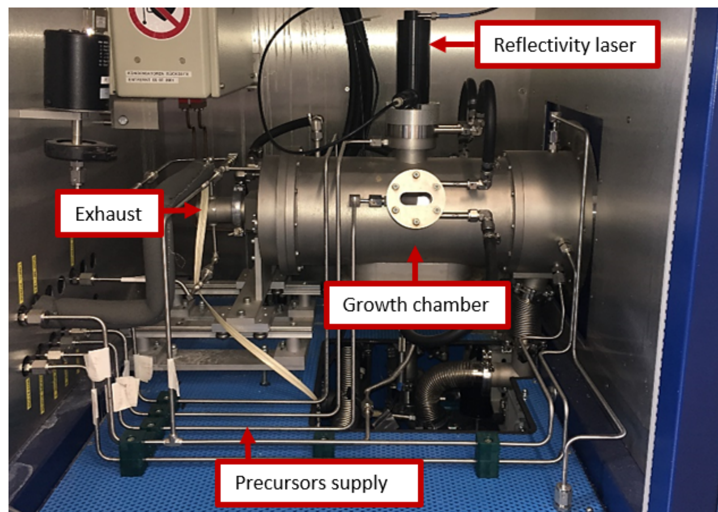

Figure 3.5 – Picture of the MOVPE-system used for the growths in this thesis.

3.1.3 Substrates

The epitaxial growths performed for this thesis were done on SiC, sapphire and AlN single crystal substrates, as shown in Fig. 3.6. Each substrate has pros and cons for electronic device performance, which will be discussed in the following section.

SiC

The high thermal conductivity and low lattice-mismatch of SiC to GaN and AlN, allow for high quality III-nitride heterostructures. In particular, for high power electronic devices, SiC enables efficient thermal heat management and low dislocation densities. One of the main drawbacks for the use of SiC is the high substrate price ($2000 for a 2 inch wafer diameter).

Sapphire

Sapphire is widely used in the fabrication of blue light emitting diodes. Surprisingly, the high initial dislocation density on sapphire does not deteriorate the efficiency of these devices thanks to the carrier localization occurring in the active region. Sapphire (Al_2O_3) substrates where used during this thesis in two forms, (i) bare sapphire substrates ($50 for a 2 inch wafer diameter) for thick GaN layers by MOVPE to be used as buffers for InAlN/GaN heterostructures, and (ii) commercial AlN templates on sapphire wafers (Dowa) were used for the growth of AlN/GaN/AlN heterostructures by MBE. The substrates have a dislocation density of $\sim 10^9$ cm^{-2} and cost about $700 for a 2 inch diameter wafer.

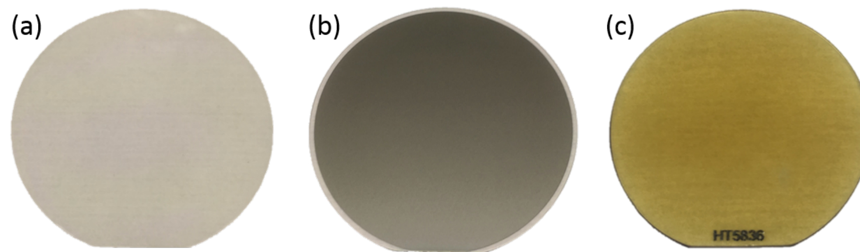

Figure 3.6 – Comparison of substrates used for the growth of III-nitrides in this thesis. (a) SiC (2 inch diameter) (b) AlN template on sapphire (2 inch diameter) with MO deposition on the backside and (c) AlN single crystal (1 inch diameter).

AlN single crystal

AlN single crystal substrates (HexaTech) are grown by physical vapor deposition. In this process, AlN source material is heated in furnaces (> 2000 °C) and by sublimation transported to a cold seed, where by condensation single crystalline AlN boules are grown. They are subsequently sliced into wafers ($5000 for 1 inch diameter). The dislocation density achievable by physical vapor deposition (PVD) is as low as $\sim 10^3$ cm^{-2}. However, these single crystals suffer from a high density of point defects, which is noticeable by the yellow color visible in Fig. 3.6(c). AlN single crystal substrates were compared with AlN template on sapphire to study the impact of the initial dislocation density on the strain relaxation of GaN on AlN (Chap. 4) and the growth of AlN/GaN/AlN heterostructures (Chap. 5).

3.2 Material characterization

3.2.1 Reflection high-energy electron diffraction

Reflection high-energy electron diffraction (RHEED) is a characterization technique used to study the surface of crystalline materials generally during growth by MBE. The RHEED setup consists of an electron gun, the sample surface, a phosphor screen and a CCD camera for detection and analysis as illustrated in Fig. 3.7.

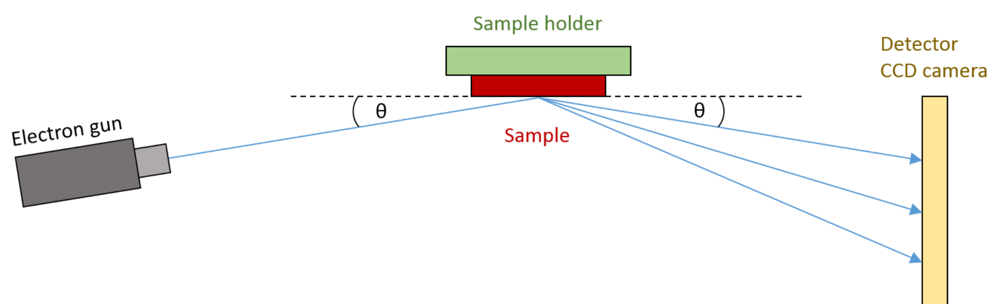

Figure 3.7 – Illustration of RHEED configuration.

The electron beam generated by the gun is accelerated to 10-20 keV and strikes the sample under a grazing angle (< 4°) relative to the sample surface. Electrons are diffracted from the surface atoms of the sample and constructive interference leads to bright spots at particular angles (Θ) on the detector, which depend on the crystal structure and the atomic plane spacing. Since the diffraction pattern strongly depends on the surface atoms, RHEED is a very surface-sensitive characterization tool giving only information about the surface of the growing crystal. Furthermore, RHEED can in general only be operated in ultra-high vacuum (MBE environment) since the electron beam strongly scatters at gas molecules. In the case of an ideal sample, the RHEED pattern consists of perfect spots. However, for real sample surfaces, the RHEED diffraction spots are usually elongated or become streaky rods. This is mainly due to the quality of the sample surface, which can lead to the broadening of the reciprocal lattice rods. A streaky RHEED pattern generally indicates a flat sample surface, where the streak broadening is due to small area coherence. There are two main scattering regimes for electrons in RHEED: (i) kinematic and (ii) dynamic scattering. A detailed description of RHEED and its application during MBE growth is thoroughly explained in literature [96]. Kinematic scattering is characterized by elastic single electron-matter (surface atoms)

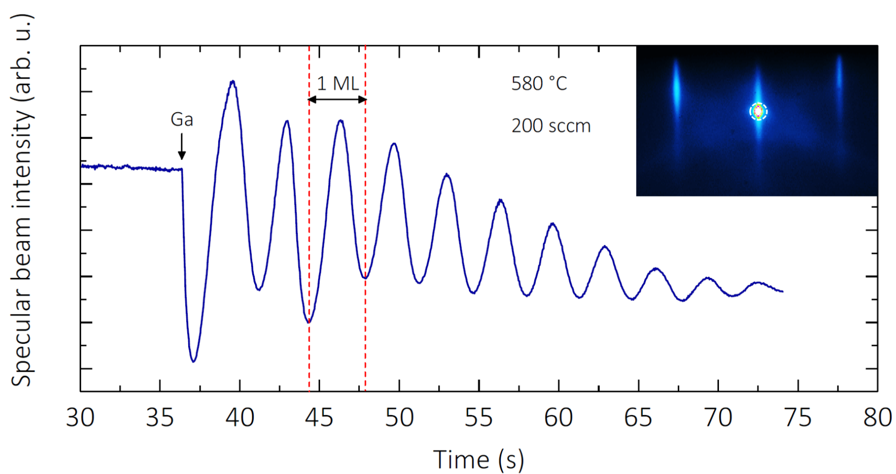

Figure 3.8 – RHEED specular beam intensity as a function of time during growth of GaN on AlN exhibiting oscillations. Inset: RHEED pattern with the specular beam indicated with white dashed circle.

interactions. The arising RHEED pattern provides information about the crystallographic properties of the sample surface. In particular, the spacing between reciprocal lattice points is inversely proportional to the lattice spacing of the real crystal surface. Hence, monitoring the spacing can be used to study the evolution of the *in-plane* lattice constant during growth of lattice-mismatched layers. This method was used extensively for the study of strain relaxation of GaN on AlN discussed in Chap. 4. Dynamic scattering, on the other hand, is due to inelastic interactions of electrons with the sample surface, which leads to change in intensity of RHEED reflections. The variation of the RHEED spot intensity is especially pronounced in RHEED oscillations, which were first reported in 1980 [97–99]. An example of RHEED oscil-

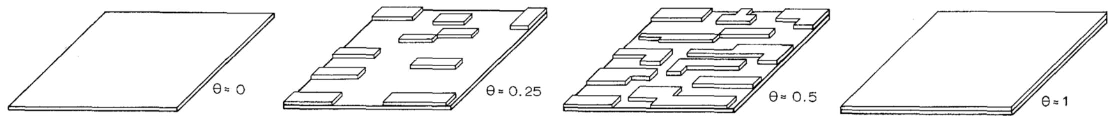

Figure 3.9 – Illustration of the layer-by-layer growth for a fractional layer coverage Θ from 0 to 1. Reproduced with modification from [100] with permission from Springer Nature.

lations during the growth of GaN on AlN are shown in Fig. 3.8. The specular beam intensity (white dashed circle shown in inset) oscillates as a function of deposition time of GaN on AlN. The arrow (Ga) indicates the point in time at which the Ga shutter was opened and growth commenced. The period of the oscillations indicates the growth of exactly 1 ML. Generally RHEED oscillations are observed for layer-by-layer growth mode (Frank–Van der Merwe) and for a 2D nucleation process. In the case of GaN grown by NH_3-MBE, this growth regime is reached when the temperature is lowered from 800 °C (step-flow growth) to below 600 °C. The modulation in intensity can be understood as a measure of the fractional layer coverage of the surface (Fig. 3.9). The intensity is the highest (constructive interference) for fully covered layers($\Theta = 1$) and the lowest for the fractional coverage $\Theta = 0.5$. RHEED oscillations are used during growth by MBE for the determination of the growth rate, alloy composition and layer thickness.

3.2.2 High resolution x-ray diffraction

High resolution x-ray diffraction (HR-XRD) is used to determine layer thicknesses, composition and strain of semiconductor heterostructures. A monochromatic beam of x-rays is generated by a x-ray tube and shone on a crystalline sample surface. The periodic arrangement of the lattice atoms causes the x-rays to be diffracted at particular angles, as illustrated in Fig. 3.10(a).

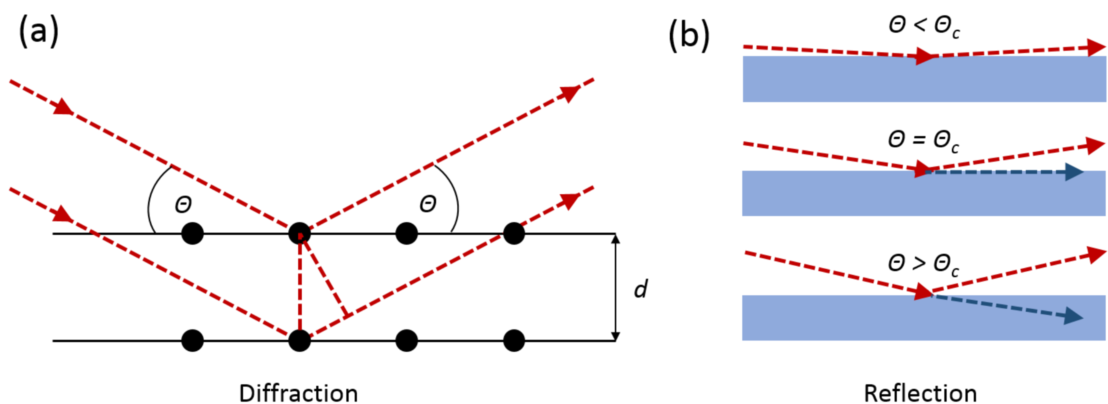

Figure 3.10 – Illustration of (a) diffraction of x-ray beams under Bragg condition. (b) Reflection of x-ray beams above and below the critical angle for total reflection.

The diffraction condition is given by Bragg's law

$$2d_{hkl}\sin(\theta) = n\lambda, \tag{3.2}$$

where d is the spacing between diffracted planes, θ is the incident angle, n is an integer corresponding to the order of diffraction and λ is the x-ray wavelength. In Fig. 3.10(a) the angle between the incident beam and sample surface is defined as θ and the diffracted angle between incident beam and the detector is 2θ. Since λ is a fixed quantity defined by the x-ray source, the peak position of Bragg reflections gives the plane spacing (d), which depends on strain and composition of the layer.

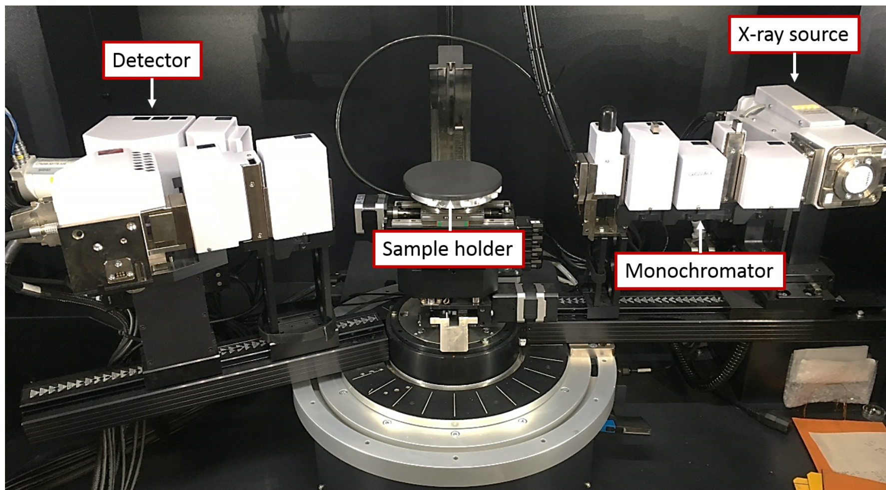

Figure 3.11 – Picture of HR-XRD system used for the characterization of heterostructures grown during this thesis.

X-ray diffraction

X-ray diffraction (XRD) is a common technique used to determine the strain, composition and crystalline thickness of semiconductor heterostructures. Symmetric scans (ω= (1/2) 2θ) are particularly interesting because they lead to reflections which are sensitive to the lattice parameter perpendicular to the surface. In the case of $\omega/2\theta$ scans, the measurement is coupled in such a way that the detector is moved by 2θ and the sample is tilted by ω. In Fig. 3.12(a) the $\omega/2\theta$ scan for the (0002) reflection is shown for an InAlN/GaN HEMT structure. The GaN peak clearly differs from the AlN peak due to the difference in c lattice parameter. Furthermore, Pendellösung fringes can be used to determine the thicknesses of thin layers t by using the Scherrer equation

$$t = \frac{\lambda}{2\Delta\theta\cos\theta}, \tag{3.3}$$

where $\Delta\theta$ is the period of fringes and λ is the x-ray beam wavelength.

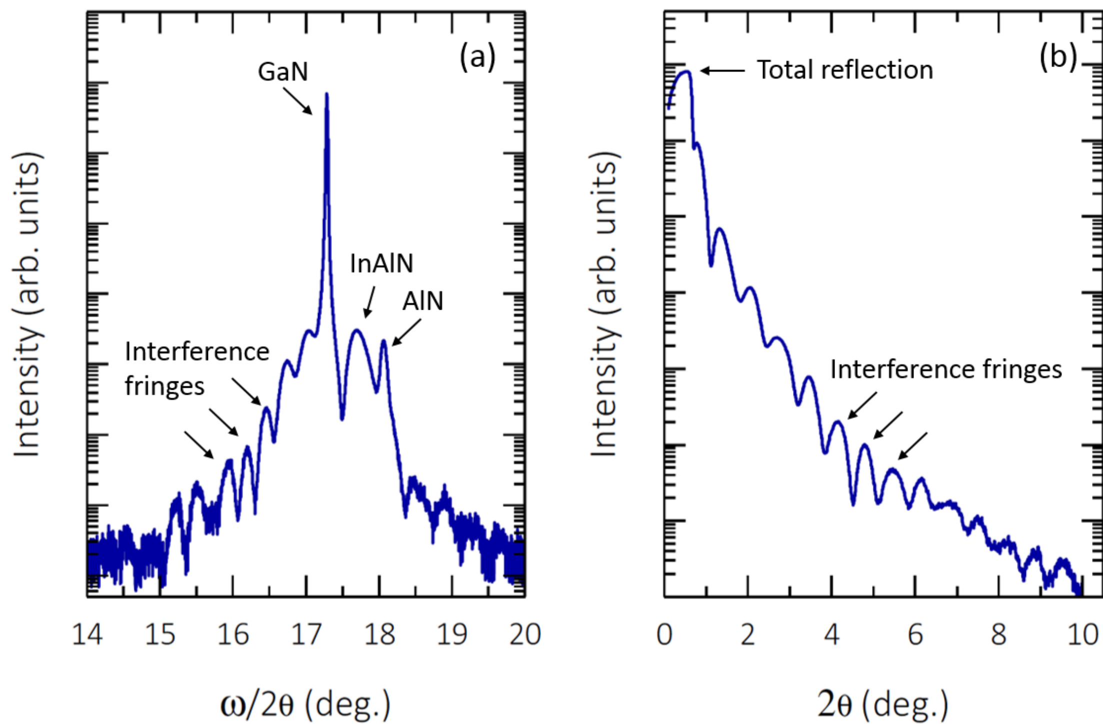

Figure 3.12 – (a) ω-2θ scan of the (0002) reflection of InAlN/GaN heterostructure on sapphire and (b) reflectivity scan of the same layer.

X-ray reflectivity

X-ray reflectivity (XRR) is a powerful measurement technique for the determination of layer thicknesses, interface roughness and density of semiconductor heterostructures. The measurement configuration can be thought as a $\omega/2\theta$ scan of the (0000) reflection. An example measurement is shown in Fig. 3.12(b). The x-ray beam strikes the sample surface under a grazing angle. Below the critical angle for total reflection (in this case $\sim 0.6°$) the x-ray beam is fully reflected, leading to a maximum intensity reaching the detector. Above the critical angle, the incident x-ray beam partially penetrates the sample. At each interface x-rays are reflected anew. The phase difference between reflected x-rays from different interfaces leads to interference fringes (oscillations in Fig. 3.12(b)), which can be used to determine the layer thicknesses. Furthermore, interface (and surface) roughness causes x-rays to be scattered diffusively rather than being reflected. This leads to a decay in intensity, which becomes more pronounced with increasing angle θ. The interface roughness can therefore be deduced from the damping of the reflectivity curves. During this thesis HR-XRD and XRR measurements were performed in a Bruker New D8 Discover setup (Fig. 3.11) for the determination of strain, layer thickness, alloy composition and interface roughness of III-nitride heterostructures.

3.2.3 Atomic force microscopy

Atomic force microscopy (AFM) is a scanning probe technique by which the topography of a sample surface can be imaged with atomic resolution. It was invented in 1982 at IBM by Gerd Binnig [101]. The working principle of the AFM is illustrated in Fig. 3.13. A cantilever

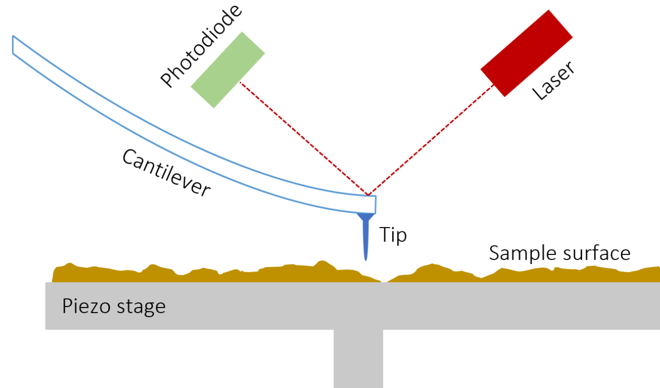

Figure 3.13 – Illustration of the working principle of an atomic force microscope.

with an atomically sharp tip is driven piezoelectrically over the sample surface. A laser beam is deflected from the backside of the cantilever and centered on a photo-detector. At small sample-tip distances (< 10 nm) Van der Waals interactions give rise to an attractive force. At smaller distances the force becomes repulsive due to physical contact between tip and sample. Piezoelectric elements are used to move the cantilever over the sample surface in a controlled manner in small precise steps. In this thesis, a Digital Instruments Nanoscope microscope was used in tapping mode to investigate the surface morphology of III-nitride heterostructures.

3.2.4 Photoluminescence

Photoluminescence (PL) is a powerful optical characterization tool that allows studying the emission energy and broadening of semiconductor heterostructures. Measurements were performed in a closed-cycle He cryostat (Janis) with a base temperature of 10 K. Photocarriers were generated by using a continuous wave (CW) HeCd laser (Kimmon Koha) with an emission wavelength of 325 nm. The resulting emission was collected by a spectrometer (Jobin-Yvon iHR 320) with Peltier-cooled Synapse CCD. PL was used in particular for the investigation of InGaN channels as a function of In content discussed in Chap. 6.

3.3 Electrical characterization

The electrical characterization of solids is of paramount importance both in fundamental and application-driven semiconductor research. In particular, the electrical resistivity of metals, semiconductors and their junctions directly influences the series resistance, capaci-

tance and threshold voltages of devices such as LEDs and transistors. The resistivity (ρ) of a solid is a fundamental property describing how conductive the material is. The values range between 10^{-8} to 10^{16} Ω cm, which allows classifying solids in metals, semiconductors and insulators. In the diffusive regime, the resistivity ρ (Ω cm) is defined as the ratio E/J, where E (V cm^{-1}) is the applied electric field and J (A cm^{-2}) is the current density. Experimentally, the resistance of a sample can be deduced in a two-probe configuration from the applied voltage V and current I flowing through the sample. However, the measured resistance intrinsically includes the contact and probe resistances, which are in series with the sample resistance. The problem of measuring the pure sample resistance was solved by the four-point probe measurement, which is discussed in the next section.

3.3.1 Four-point probe technique

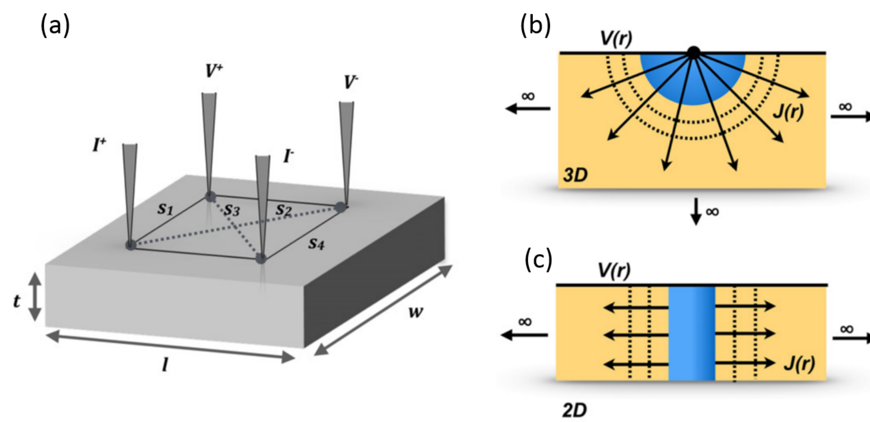

Figure 3.14 – (a) Illustration of the four-point probe measurement in the square geometry. The measurement current flows between two probes indicated by $I^{+(-)}$ and the voltage drop is measured between the other two probes $V^{+(-)}$. The current density (J) in 3D (b) and 2D (c) layers are shown to flow in a spherical and cylindrical manner, respectively. Reproduced from [102] under a Creative Commons license.

The four-point probe technique was first introduced by Frank Wenner in 1913 [103]. The basic principle of the technique is to use two probes for applying a current and measuring the voltage drop across the remaining two. This method allows for the direct measurement of the sample resistance, excluding contact and probe resistances, which would be added in series in a simple two-point approach. The configuration of the probes is usually in two geometries, (i) collinear and (ii) square. Resistivity measurements performed during this thesis were performed exclusively in the square geometry shown in Fig. 3.14(a), which is a necessary configuration for the Hall effect measurements described in the next section. The probe spacing and sample thickness are indicated as s and t, respectively. In the case where the thickness of the conducting layer is much smaller compared to the probe spacing ($t \ll s$), the semi-infinite 3D material appears as a 2D sheet and the current spreads through the sample cylindrically instead of spherically (3D case), which is illustrated in Figs. 3.14(b) and (c). This

assumption is valid for all resistivity measurements performed in this thesis, since the sample thickness usually was 10^{-8} m, whereas the probe spacing was 10^{-3} m. The resistivity of the conducting layer in a square geometry is given by [102]

$$\rho = \frac{\pi t}{\ln 2} \frac{V}{I}. \tag{3.4}$$

Interestingly, the resistivity does not depend on the probe spacing s, which underlines the 2D character of the layer geometry. Assuming a homogeneous and finitely thick sample, the resistivity can be replaced by a normalized quantity

$$R_{\mathrm{S}} = \frac{\rho_{\mathrm{2D}}}{t}, \tag{3.5}$$

which is called the sheet resistance and is measured in ohms (Ω). Often R_{S} is given in Ω/sq (ohms per square) in order to distinguish it from the resistance itself. The origin of this unit lies in the fact that a square sheet of 1 Ω/sq has the same resistance regardless of its dimensions.

3.3.2 Van der Pauw theorem

The resistivity of a sample with probes arranged in a square geometry is given by Eq. 3.4, as discussed in the previous section. However, this equation assumes an ideal configuration of probes (i.e. perfect symmetric alignment between them). For actual measurements, the probe asymmetry can lead to large deviations. Therefore, these asymmetries need to be taken into account by investigating the resistivity of sample geometries with weaker probe configuration symmetries and introducing a correction factor. The resistivity measurement of a layer can be extended from collinear and square geometries to any arbitrary shape by applying the Van der Pauw theorem, which is valid under the following conditions, (i) the probes are located at the sample's periphery and their respective size is small compared to the sample, and (ii) the samples need to be homogeneous, thin, isotropic and singly connected. If a current I_{12} is flowing between probes 1 and 2, while a voltage drop V_{34} is measured between probes 3 and 4, the resistance is given by $R_{1,2/3,4} = V_{34}/I_{12}$. In the same manner, the resistance $R_{2,3/4,1}$ is defined. The Van der Pauw theorem states that these resistances satisfy the following relation [104]

$$\mathrm{e}^{-\pi \frac{t}{\rho} R_{1,2/4,3}} + \mathrm{e}^{-\pi \frac{t}{\rho} R_{2,3/1,4}} = 1, \tag{3.6}$$

and the resistivity of a layer is then given by the following expression,

$$\rho = \frac{\pi t}{\ln(2)} \frac{R_{1,2/4,3} + R_{2,3/1,4}}{2} F, \tag{3.7}$$

where F is the correction factor given by

$$\cosh\left(\frac{\ln 2}{F}\frac{R_{1,2/3,4}/R_{2,3/4,1}-1}{R_{1,2/3,4}/R_{2,3/4,1}+1}\right)=\frac{1}{2}e^{\frac{\ln 2}{F}}. \tag{3.8}$$

For samples with a symmetry plane (e.g ideal square probe geometry), the resistances $R_{1,2/3,4}$ and $R_{2,3/4,1}$ are identical (F = 1) and Eq. 3.7 reduces to the resistivity expression (Eq. 3.4) discussed in the previous section. In the symmetric case, the resistivity can be determined from a single resistance measurement. The resistivity of a sample is a measure of how well it conducts an electrical current. Its value is directly related to the density (n) and mobility (μ) of the carriers by

$$\rho=\frac{1}{qn\mu}, \tag{3.9}$$

In the following section, the Hall effect measurement will be introduced for the determination of μ and n.

3.3.3 Hall effect

The Hall effect was discovered by Edwin Hall in 1879 [105]. Today, it is widely used in the semiconductor industry for electrical characterization of conducting layers. In the previous section, the four-point measurement in the Van der Pauw geometry was discussed, which allows for the determination of the sheet resistance. A combination of both techniques allows for the measurement of density and mobility of carriers. In the first part of the following section, the theory of the Hall effect is discussed. Then, a description of the measurement procedure follows.

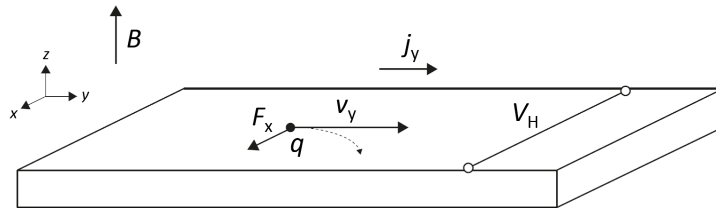

Figure 3.15 – Illustration of the Hall effect. A magnetic field (B) is applied perpendicular to a current (current density j_y) passing through a conducting layer. The carriers with charge q are deflected from their direction of motion (v_y) by the Lorenz force F_x. The accumulation of charge in the x-direction leads to a build-up of potential V_H.

Theory

The basic principle of the effect is illustrated in Fig. 3.15. An electrical current (I) flowing through a conducting layer (in the y-direction) results in the movement of carriers with an

average drift velocity (v_y) parallel or antiparallel to the current, depending on the charge of the carriers. When a magnetic field **B** is applied perpendicular to the current (z-direction) the carriers are deflected by the Lorenz force $\mathbf{F}_L$ described by

$$\mathbf{F}_L = e(\mathbf{E} + \mathbf{v} \times \mathbf{B}), \tag{3.10}$$

where **v** is the average drift velocity of the charge e and **E** and **B** are the electric and magnetic fields, respectively. The deflection leads to a build-up of charge in the direction perpendicular to the magnetic field and the current. The resulting potential is called the Hall voltage (V_H) and can be expressed by the following equation.

$$V_H = \frac{1}{t} R_H I B. \tag{3.11}$$

Here, I is the current, B is the applied magnetic field, t is the layer thickness and R_H is the Hall coefficient, which is given by,

$$R_H = \pm \frac{1}{en}, \tag{3.12}$$

where n is the carrier density. The sign of the Hall coefficient indicates the type of majority carriers (electrons or holes) participating in the conduction. Using Eq. 3.9 from the previous section, the carrier density and mobility can be calculated with

$$n = \frac{1}{R_H e}, \tag{3.13}$$

and

$$\mu = \frac{R_H}{\rho}. \tag{3.14}$$

Sample preparation

Before samples can be characterized by Hall measurements, the wafers need to be diced (or cleaved) in small pieces which fit on the chip holders used in the setup. In Fig. 3.16(a) a standard 2 inch sapphire wafer is illustrated. Thanks to the hexagonal crystal structure of sapphire the wafers can be cleaved into 6 equivalent pieces after deposition of III-nitrides. Further cleaving of the wafer sixths finally leads to 5×5 mm^2 square pieces (red dashed square in Fig. 3.16(a)), which fit well in the chip holder and are far away from the exclusion zone of the wafer (2-3 mm from wafer edge). Next, ohmic contacts need to be formed to the conducting layer. This was done in two ways: (i) Deposition and annealing (850 °C under N_2) of alloyed metal stacks (Ti/Al/Ni/Au) and (ii) soldering of In droplets (300 °C) at the corners of the sample as illustrated in Fig. 3.16(b). It is important to note that the relative size of contacts should be small compared to the total sample area in order to reduce measurement errors. In most cases, the second method was used due to the lower temperature and fewer

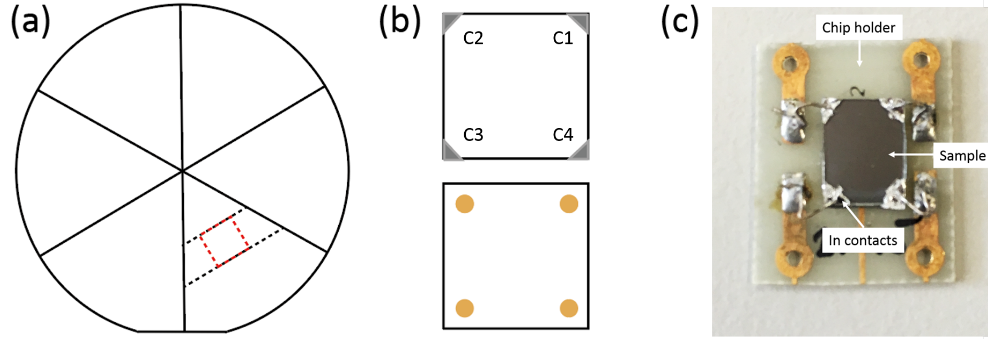

Figure 3.16 – Illustration of (a) substrate with cleavage lines and square piece (red) used for electrical characterization. (b) 5×5 mm^2 sample with indium (top) and alloyed Ti/Al/Ni/Au (bottom) contacts. (c) Photograph of sample in chip holder

processing steps. In Fig. 3.16(c) a fully soldered sample on a chip holder is shown which can be introduced into the setup.

Setup and measurement

Hall effect measurements were performed in a PhysTech RH 2010 setup consisting of a variable current source (1-100 μA), a voltage measurement circuit with automatic amplification, a magnet (±0.5 T) and a sample stage. The four-point resistivity was determined from I/V curves at different contact configurations and magnetic fields (B ± 0.5 T). The specific resistivity (Van der Pauw) was determined in a parallel configurations, which means that the current was passed through contact pairs (1,2) (see Fig. 3.16(b) for contact numbering) and the voltage drop was measured between contacts (3,4). The same measurement was performed on the two contact pairs rotated by 90° i.e. (2,3) and (1,4). The resistivity was then calculated with Eq. 3.7. For the Hall coefficient, the sample pairs are chosen in a perpendicular configuration as discussed in the previous section. The Hall coefficient is then given by

$$R_{\mathrm{H}} = \frac{t}{2B_{\mathrm{max}}}\left(R_{1,3/2,4}^{B=+\mathrm{B}_{\mathrm{max}}} - R_{1,3/2,4}^{B=-\mathrm{B}_{\mathrm{max}}}\right), \tag{3.15}$$

where the resistance $R_{1,3/2,4}^{B=+\mathrm{B}_{\mathrm{max}}}$ is measured at two magnetic fields of opposite sign. The carrier density and mobility can then be calculated with Eqs. 3.13 and 3.14, respectively.

3.3.4 Transmission line measurement

In the previous section, the four-point probe measurement was introduced, which is used to determine the sheet resistance of a conducting layer while minimizing the effect of sample geometry and contact resistance. However, from a technological perspective, the contact resistance between a metal pad and the semiconductor active area is of paramount importance

in order to reduce parasitic power consumption. In this section, the transmission line measurement will be discussed, which was used to determined the contact resistance of ohmic contacts to 2DEGs in Chap. 7. In Fig. 3.17 the resistance contributions for a semiconductor

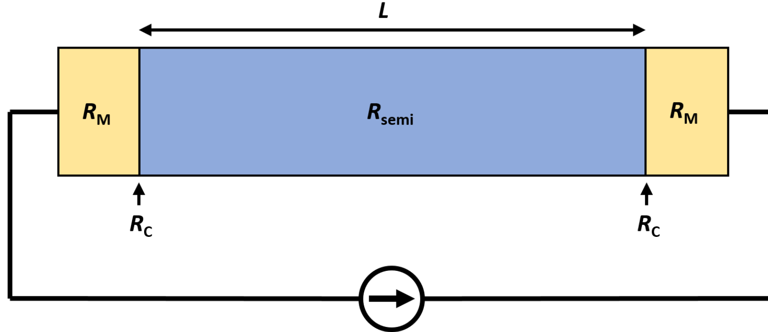

Figure 3.17 – Illustration of a simple resistor geometry for a semiconductor layer (blue) of length L connected to two metal contacts (yellow). The total resistance is the sum of the metal contact resistances (R_M), semiconductor resistance (R_semi) and the contact resistances (R_C), which are at the metal/semiconductor interfaces.

slab connected to metal pads are illustrated. In a closed circuit the semiconductor slab is connected to at least two metal pads (yellow squares in Fig. 3.17) each contributing a resistance of R_M. Furthermore, the metal/semiconductor interface gives rise to a second source of resistance also called the contact resistance (R_C). Finally the semiconductor resistance (R_semi) itself needs to be taken into account. The total resistance can therefore be written as

$$R_\mathrm{T} = 2R_\mathrm{C} + 2R_\mathrm{M} + R_\mathrm{semi}, \tag{3.16}$$

where R_C is the contact resistance at the metal/semiconductor interface and R_M is the metal resistance, which usually is much smaller than the contact resistance ($R_\mathrm{C} \gg R_\mathrm{M}$) and therefore can be neglected. The semiconductor resistance (R_semi) can be calculated from the sheet resistance (R_S), the length L and width W of the layer by $R_\mathrm{semi} = R_\mathrm{S} L/W$. The total resistance in Eq. 3.16 can therefore be rewritten as

$$R_\mathrm{T} = 2R_\mathrm{C} + R_\mathrm{S} L/W. \tag{3.17}$$

It is evident that the total resistance depends linearly on the spacing between the metal pads (L). In Fig. 3.18 a series of metal pads deposited on the semiconductor are illustrated with increasing spacing (L) between them. The transmission line measurement consists of measuring the total resistance in such structures as a function of the spacing and applying Eq. 3.17. In Fig. 3.19, a typical measurement is presented. As expected, the total resistance increases linearly as a function of the spacing. By linear fitting and extrapolation, the contact resistance and the sheet resistance can be determined from the total resistance intercept and the slope, respectively.

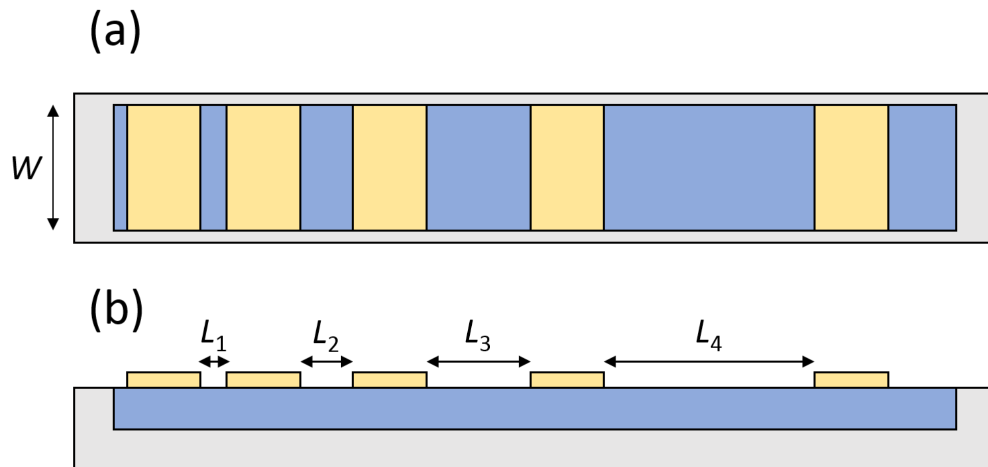

Figure 3.18 – Illustration of TLM structure. (a) Top view showing the metal pads (yellow) of width W on the conducting layer (blue). (b) Side view showing the metal contact spacings L_1 to L_4.

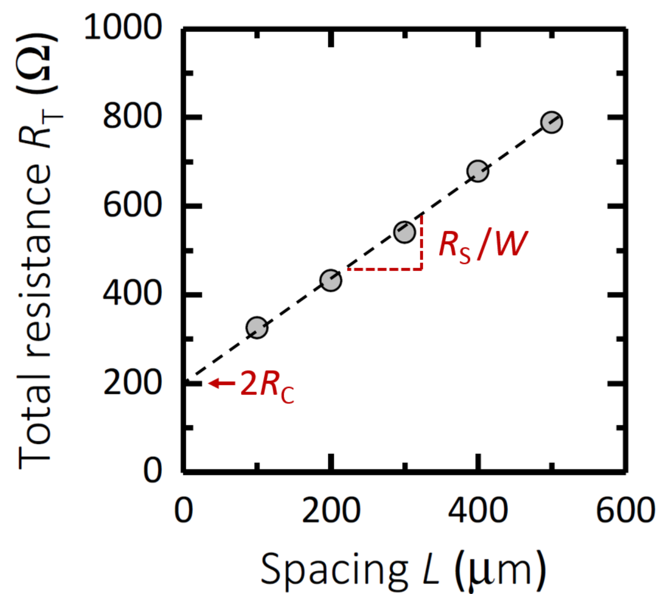

Figure 3.19 – Example illustrating a typical TLM measurement. The total resistance (R_T) is measured as a function of the metal pad spacing L. The contact resistance (R_C) and sheet resistance (R_S) can be deduced from linear extrapolation of the fitted line (dashed line).

3.4 Simulation software: NextNano

NextNano is a simulation tool used to understand the electronic structure of semiconductor heterostructures [106]. A database contains the material parameters for most group III-V materials. As an input, the heterostructure materials, crystal structure, crystallographic direction, temperature and dimensions are defined. The Fermi level pinning discussed in the

previous chapter is taken into account by defining a Schottky barrier at the surface (semiconductor/air interface) of the heterostructure. For this thesis, wurtzite III-nitride heterostructures grown along the (0001) direction at room temperature were considered. The software evaluates the bulk band structure for all used materials. The structures are assumed to be fully pseudomorphic. Hence, strain calculations are performed to take into account the deformation potentials. Subsequently, the new band edges, incorporating the spontaneous and piezoelectric polarization-induced charges and electric fields are determined. Finally, Poisson and multi-band $\mathbf{k} \cdot \mathbf{p}$ Schrödinger equations are solved self-consistently. The program output provides the wave function probabilities, band edges, electric fields and the electron and hole densities along the growth direction.

4 Heteroepitaxy: GaN on AlN

4.1 Background

The growth of GaN/AlN heterostructures presents one of the fundamental building blocks in III-nitride semiconductors. The large conduction band offset between GaN and AlN allows for the realization of strongly confined electron systems, e.g. quantum wells or triangular wells with a two-dimensional electron gas. Thin GaN channels grown on AlN are particularly interesting for high electron mobility transistors operating at high power, as AlN is an excellent thermal conductor ($\kappa = 300$ W m^{-1} K^{-1}). Heat generated during high power operation can therefore easily be removed from the device. Furthermore, AlN is a perfect electrical insulator ($E_g = 6.00$ eV), which reduces potential parasitic leakage currents from the two-dimensional electron gas to the buffer. With the emergence of AlN single crystal substrates in recent years, their application to HEMTs could potentially exhibit unprecedented performance.

However, one of the main challenges in the growth of GaN on AlN is the large lattice-mismatch of 2.4 %. As discussed in the previous chapter, the growth of lattice-mismatched layers is generally accompanied by strain accommodation. The plastic strain relaxation by the creation of dislocations is detrimental for electronic devices because they can introduce parasitic conduction paths, which lead to leakage current. Therefore, it is of great interest to understand the strain relaxation mechanism, and in particular, to determine the critical thickness above which strain relief occurs. In recent years there have been several reports on the critical thickness of GaN on AlN, which is usually 11-12 MLs [72, 79]. This exceeds by far the theoretical value of 3 MLs based on energy minimization [57] and force balance models [59], which assume near-equilibrium growth conditions. The underestimation of the critical thickness in theory suggests that the layers are in a metastable state due to the lack of efficient strain relaxation mechanism. Fischer *et al.* developed a theoretical model which incorporates the elastic interaction between dislocations [68]. Using this model, a critical thickness of 20 MLs has been calculated. Indeed, it is well known that III-nitrides grown along the *c*-axis lack proper gliding planes for dislocation motion and hence efficient strain release [75]. The metastable state of strained III-nitride semiconductors suggests a large impact of kinetics, governed by

the initial dislocation density and growth temperature.
In this chapter, the critical thickness of GaN on AlN is determined as a function of growth temperature and initial dislocation density.
The material used in this chapter was partially published [107] and reproduced with permission from IOP.

4.2 Critical thickness of GaN on AlN

The strain relaxation and the critical thickness of GaN grown on AlN was investigated by RHEED as a function of growth temperature and initial dislocation density. The temperature range was chosen to be between 750 and 900 °C in order to avoid GaN desorption at high temperatures (> 900 °C) and kinetic roughening at lower temperatures (< 750 °C). The initial dislocation density was 10^9 and 10^3 cm^{-2} for AlN templates on sapphire and AlN single crystal substrates, respectively. By monitoring the spacing between the (10) and $(\bar{1}0)$ RHEED streaks in real-time during growth, the surface *in-plane* lattice constant can be determined.
In Fig. 4.1(a), the streaky RHEED pattern of the AlN template on sapphire substrate surface is shown. The intensity profile between the reflections was measured along the $< \bar{1}010 >$ direction illustrated with a red line. Next, the reflection spacing was determined by fitting Gaussian curves to the intensity peaks shown in Fig. 4.1(b). The spacing of the reflections is inversely proportional to the *in-plane* lattice constant of the growing surface. Hence, the evolution of the lattice-constant can be monitored *in situ* as a function of GaN thickness grown on AlN. In Fig. 4.2, the streak spacing is shown for the growth of GaN on AlN template on sap-

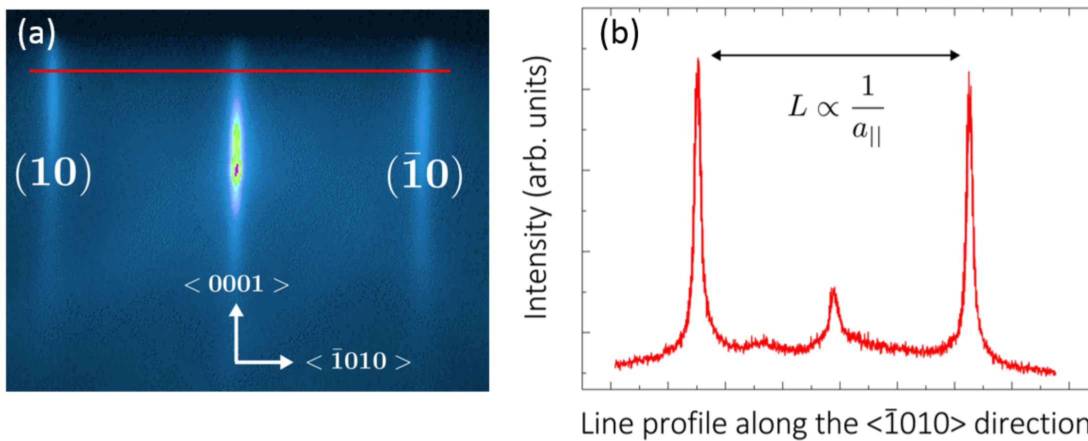

Figure 4.1 – (a) RHEED pattern of AlN template on sapphire in the $< 11\bar{2}0 >$ azimuth direction. The red line corresponds to a line profile used to determine the spacing between the (10) and $(\bar{1}0)$ reflection. (b) The streak spacing L is inversely proportional to the *in-plane* lattice constant a of the growing surface. Reproduced from [107] under a Creative Commons license.

phire at 800 °C as a function of time. The growth is initiated after a stabilization period of 20 s. The arrow indicates the time at which the Ga cell shutter was opened. The streak spacing

decreases with time, which corresponds to an increase of the *in-plane* lattice constant of the GaN surface on AlN. The streaky RHEED patterns of the AlN template on sapphire and GaN prior and after the growth are shown in Fig. 4.2, respectively. In Fig. 4.3 the RHEED pattern for GaN on AlN template on sapphire (a) and (c) is compared to the growth on AlN single crystal (b) and (d). Interestingly, the specular beam intensity for the growth on AlN single crystal is far more pronounced with a circular shape, indicating a very smooth surface. Furthermore, Kikuchi lines are clearly visible, which also suggests a high quality material [96]. Surface roughening by the formation of 3D islands (elastic strain relaxation) leads in general to a spotty RHEED pattern [72], as discussed in the previous chapter. Hence, a change in the *in-plane* lattice constant while maintaining a 2D surface can be ascribed to plastic strain relaxation by the introduction of dislocations. In a next step, the streak spacing is converted to the lattice-mismatch between GaN and AlN ($\Delta a/a = (a_{\mathrm{GaN}} - a_{\mathrm{AlN}})/a_{\mathrm{AlN}}$) and the time axis is replaced by the thickness of GaN grown on AlN by using the growth rate, which was determined from RHEED oscillations. In Fig. 4.4, the evolution of the lattice-mismatch between

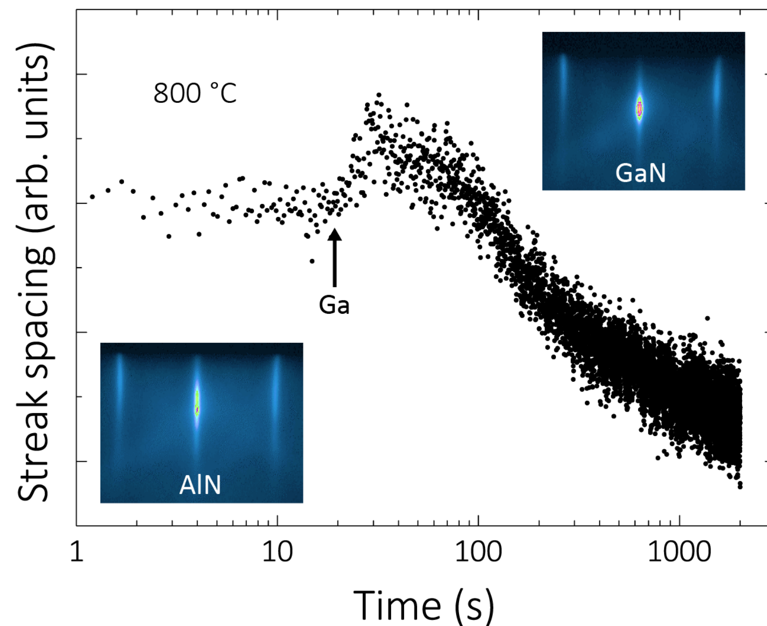

Figure 4.2 – Evolution of RHEED pattern streak spacing with time during growth of GaN on AlN template on sapphire. The arrow corresponds to the time of opening of the Ga cell shutter. The RHEED patterns (insets) show streaky rods prior and after growth, insuring a flat surface morphology.

GaN and AlN template on sapphire is given as a function of GaN thickness for different temperatures ranging from 750 to 900 °C. There are three main features: (i) The onset of plastic strain relaxation (at the critical thickness) is strongly temperature dependent, (ii) the lattice-mismatch saturates at large thicknesses for all temperatures, which suggests that the GaN layer never fully relaxes on AlN. Interestingly, the residual strain is also temperature dependent. At low temperature (750 °C), the strain remains for thick GaN layers (1000 MLs) and the relaxation process appears to be frozen out. For high temperature (900 °C), the residual

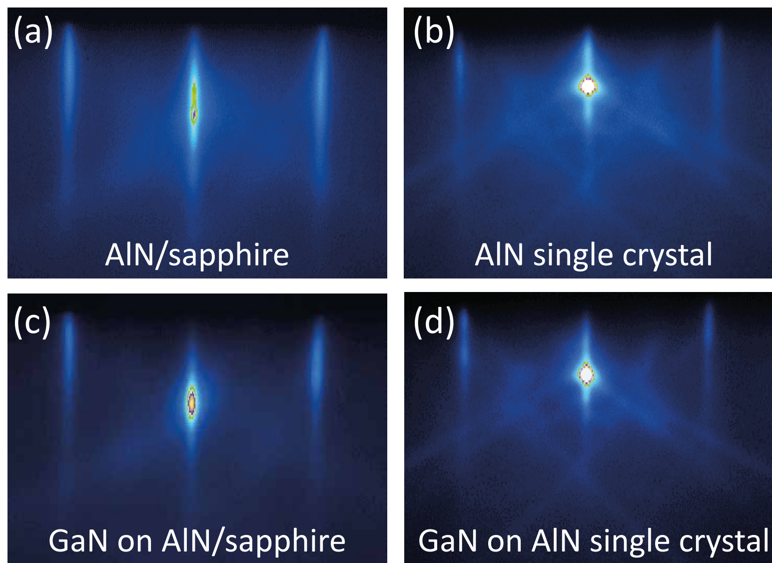

Figure 4.3 – RHEED pattern of (a) initial AlN template on sapphire, (b) AlN single crystal and after growth of ~ 100 MLs of GaN at 800 °C (c) and (d), respectively. Reproduced from [107] under a Creative Commons license.

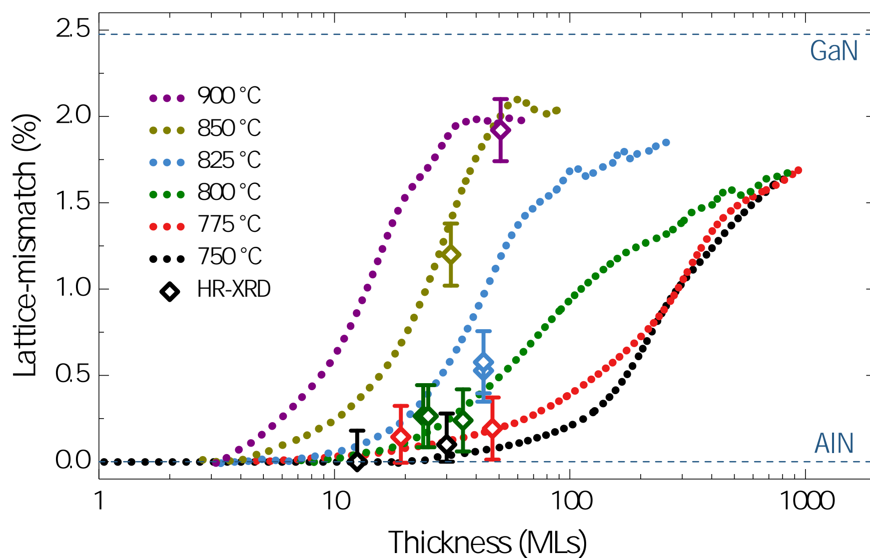

Figure 4.4 – Evolution of the lattice-mismatch as a function of GaN layer thickness grown on AlN template on sapphire for substrate temperatures ranging from 750 to 900 °C. Diamonds correspond to the lattice-mismatch determined *ex situ* by HR-XRD. Reproduced from [107] under a Creative Commons license.

strain is lower. (iii) The relaxation rate increases strongly with temperature, which suggests that the relaxation process is thermally activated. This can be clearly seen in Fig. 4.5, where only the initial relaxation stage is considered. The curves are linear and the slopes can be easily determined. Assuming a purely phenomenological thermal activation, an energy of

2.2 eV can be extracted from the corresponding Arrhenius plot shown in the inset of Fig. 4.5. The physical interpretation of this activation energy will be discussed at a later stage. In Fig.

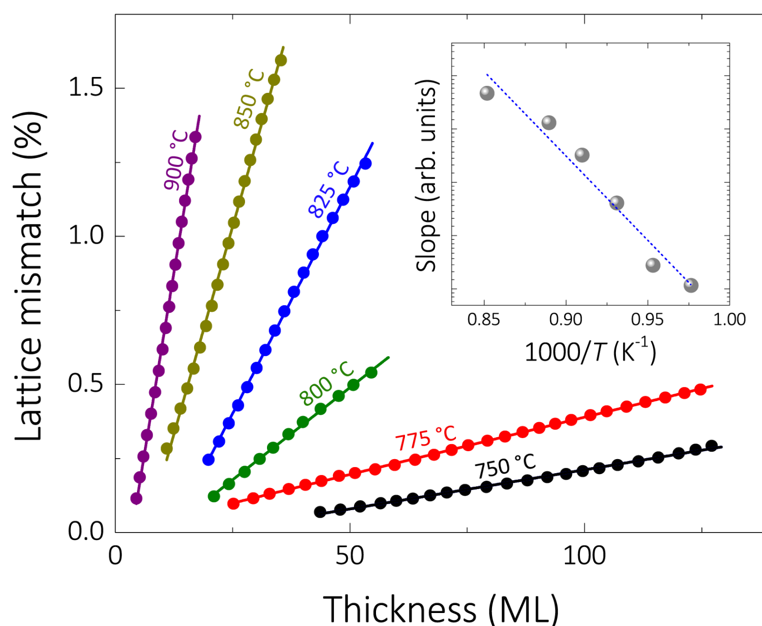

Figure 4.5 – Evolution of lattice-mismatch as a function of GaN layer thickness grown on AlN template on sapphire for substrate temperatures ranging from 750 to 900 °C shown in linear scale. The slopes were used to determine an activation energy as a function of growth temperature shown in the inset.

4.6, the critical thickness is given as a function of growth temperature, which was determined from the first inflection of the relaxation curves. The critical thickness increases from 3 to 16 MLs as the temperature is decreased from 900 to 750 °C. It is important to note that RHEED is a surface sensitive technique which only probes a few MLs below the surface. Therefore, the strain state of the layers are further examined *ex situ* by HR-XRD. The GaN layer thickness and strain were determined by performing ω-2Θ scans along the (0002) direction as discussed in the previous chapter. The results are shown in Fig. 4.4 as diamonds. A fairly good agreement is found between RHEED and HR-XRD, which means that the strain evolution observed *in situ* does indeed corresponds to the *ex situ* strain state of the layer. This might seem oversimplified at first, considering the effect of cooling on the strained layer. However, the thermal expansion coefficients of GaN, AlN and sapphire are very similar and therefore do not impact the strain substantially. The growth temperature strongly affects the strain relaxation and critical thickness of GaN layers grown on AlN. Interestingly, such a temperature dependence has been observed in other material systems such as Si/Ge [108], InGaAs/GaAs [61, 109, 110], MgO/Fe [111] and GaAsSb/GaAs [112]. As discussed in the previous chapter, it was shown that the low growth temperature of these layers leads to a metastable state with fully strained layers much thicker than the predicted critical thickness based on near-equilibrium calculations [62]. The metastable behavior was theoretically discussed by Fischer *et al.* [68], which then proposed a critical thickness model incorporating the creation and interaction energy

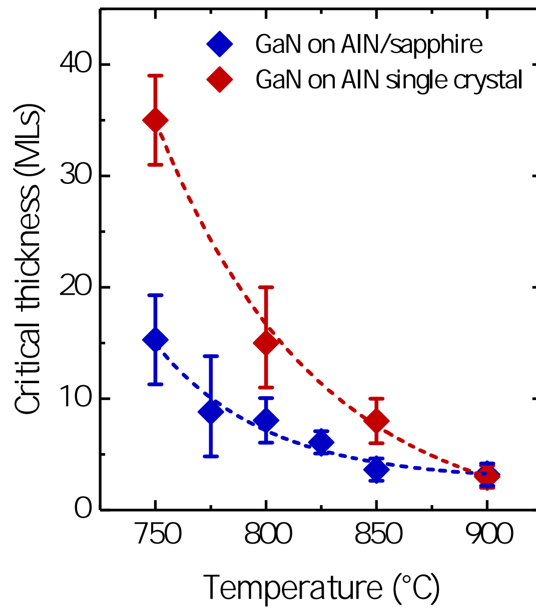

Figure 4.6 – Critical thickness of GaN on AlN/sapphire template (blue diamonds) and AlN single crystal (red diamonds) as a function of growth temperature. Dashed lines are fitting curves assuming an exponential temperature dependence. Reproduced from [107] under a Creative Commons license.

of dislocations. This additional energy term can be seen as direct competition with the thermal energy due to the growth temperature. Hence, at low temperatures the kinetics of strain relaxation are frozen out leading to a metastable phase of highly strained layers. The critical thickness based on the model proposed by Fischer *et al.* gives a critical thickness of about 20 MLs for GaN grown on AlN. This value should be used with care considering that the model was originally developed for Si/Ge, which has a cubic crystal structure. On the other hand, for the wurtzite crystal structure it has been shown using symmetry arguments that only certain planes (*i.e.* $1/3\langle 11\bar{2}3\rangle\{11\bar{2}2\}$ and $1/3\langle 11\bar{2}3\rangle\{1\bar{1}01\}$) are favorable for dislocation motion and therefore strain relaxation [80]. The semi-empirical model explaining the strain relaxation process for metastable layers was developed by Dodson and Tsao [67], which was discussed in detail in the previous chapter. In the next part, the model will be compared to our experimental results. The basic assumption of the theory is that the effective stress in the layer is the driving force for strain relaxation. The relaxtion process can be divided into four distinct regimes illustrated in Fig. 4.7. In the first regime, the elastic strain is accumulated in the growing GaN layer and remains pseudomorphic. In the second regime, the strain relaxation process begins via pre-existing dislocations from the AlN substrate. In the third regime, multiplication of dislocations leads to a rapid increase in the strain relaxation rate. The mobility of dislocations is thermally activated, which explains the strong temperature dependence of the strain relaxation rates shown in Fig. 4.5. In the fourth regime, the strain relaxation process saturates. This can be understood in the following way. The dislocation mobility is proportional to the effective stress remaining in the layer. With increasing thickness the strain

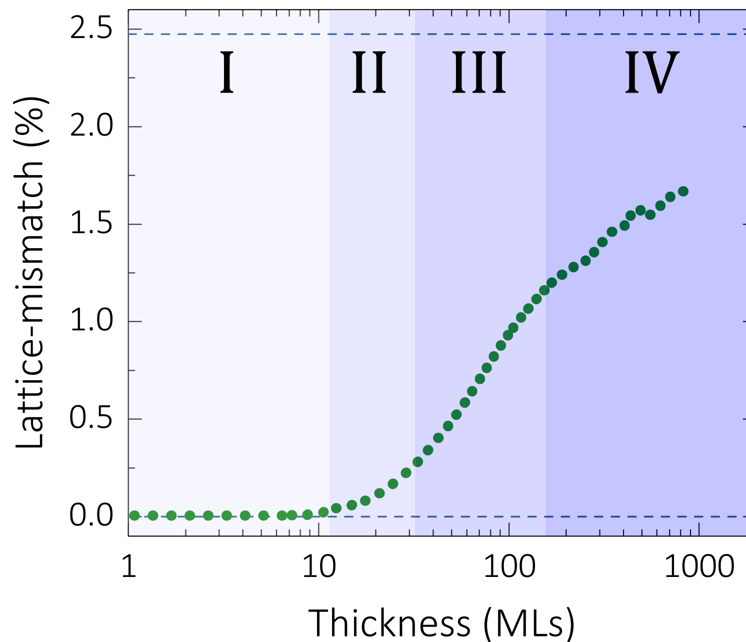

Figure 4.7 – Evolution of lattice-mismatch as a function of GaN layer thickness at 800 °C with illustration of the different strain relaxation regimes, (i) Pseudomorphic growth. (ii) Initial strain relaxation due to pre-existing dislocations. (iii) Strain relaxation due to creation and multiplication of misfit dislocations. (iv) Saturation of the relaxation process due to the reduced effective stress.

relaxes and reduces the effective stress and the mobility of dislocations. Multiplication and creation of dislocations becomes more difficult and the strain relaxes very slowly. This leads to residual strain at large GaN thicknesses (> 1000 MLs), as shown in Fig. 4.7. In a next step, the impact of initial dislocation density on the strain relaxation process is studied. For this purpose, GaN layers are grown on AlN single crystals in the same temperature range as for AlN template on sapphire. The evolution of the lattice-mismatch is displayed in Fig. 4.8 with the corresponding critical thicknesses given in Fig. 4.6. Interestingly, the critical thickness is also 3 MLs at high temperature (900 °C) for the AlN single crystal and therefore is independent of the initial dislocation density. This is in agreement with theoretical calculations based on energy minimization, which assumes near-equilibrium conditions [59]. In contrast, the critical thickness for GaN on AlN single crystal dramatically increases (30 MLs) when the temperature is lowered. This is in agreement with data reported on AlN/GaN/AlN quantum well heterostructures grown by PA-MBE, which results in a pseudomorphic GaN layer of 39 MLs in thickness [113]. The low growth temperature (600 °C) used in PA-MBE likely gives rise to an even higher critical thickness. The lowest temperature used in this study so far was limited to 750 °C due to the appearance of a spotty RHEED pattern at 700 °C likely due to kinetic roughening, which takes place in NH_3-MBE. In Sec. 4.4 of this chapter, the optimization of growth conditions will be discussed, which allow the growth of pseudomorphic GaN layers by NH_3-MBE at 700 °C. In Fig. 4.9, the evolution of the lattice-mismatch at 750

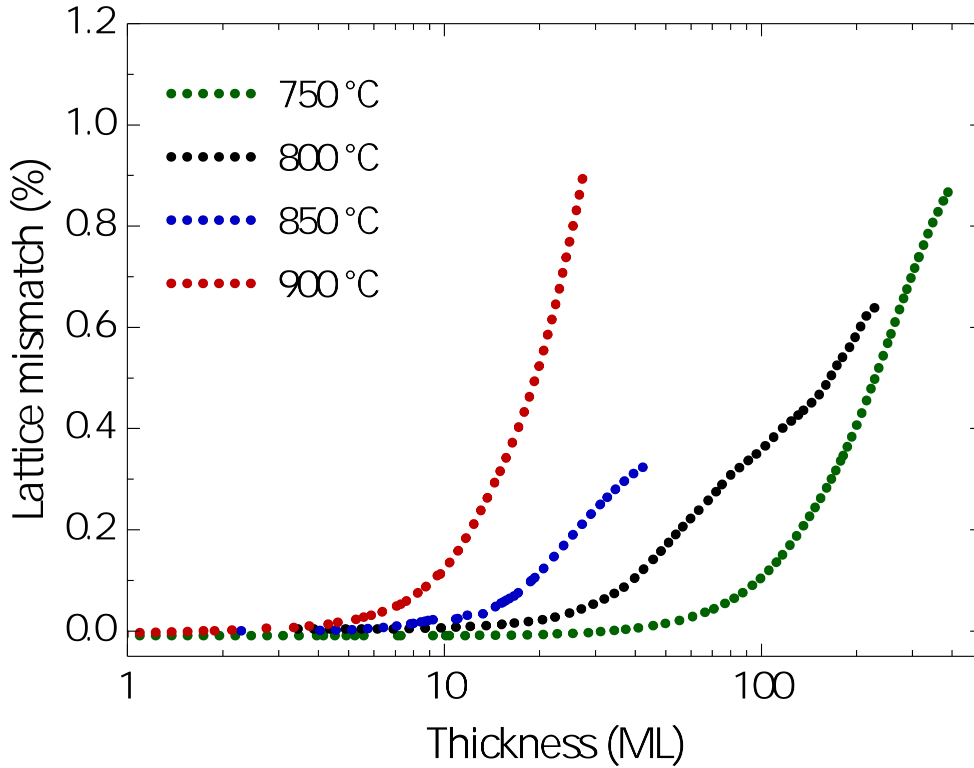

Figure 4.8 – Evolution of lattice-mismatch as a function of GaN layer thickness grown on AlN single crystal for substrate temperatures ranging from 750 to 900 °C.

and 900 °C is compared for both substrates (AlN template on sapphire and AlN single crystal). At 900 °C the critical thickness is 3 MLs for both substrates as discussed previously. In contrast, the relaxation rate at the early stages of growth is lower in the case of the AlN single crystal. For larger thicknesses, the relaxation rates become comparable. This can be understood in the following way. The low dislocation density of the AlN single crystal hinders the initial relaxation process. The effective strain increases with increasing thickness. The high stress field enables a high mobility for the motion and multiplication of dislocations. Eventually, their density becomes high enough to allow for efficient plastic relaxation, as it occurs on AlN template on sapphire. A similar behavior is observed at low temperature, but in this case the critical thickness is much larger. These observations are in agreement with the phenomenological model of Dodson and Tsao [67].

There are two clear observations from the results so far, (i) the temperature-dependent residual strain indicates a non-equilibrium state, which is in line with the fact that growth by MBE usually happens far from thermodynamic equilibrium and (ii) the temperature-dependent relaxation rate suggests a physical barrier for the motion and creation of dislocations, which are responsible for the plastic relaxation process. Hence, the temperature dependence of the strain relaxation rate and the critical thickness seem to be governed by a characteristic activation energy [62, 67]. The mobility of dislocations is known to be thermally activated.

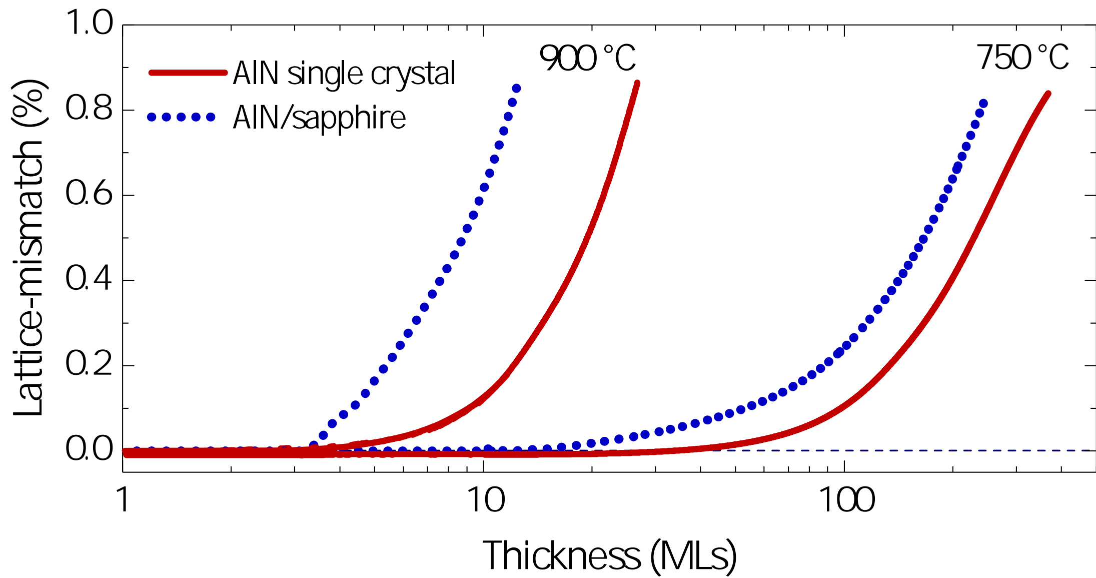

Figure 4.9 – Comparison of strain relaxation of GaN on AlN template on sapphire (blue dotted line) and AlN single crystal (red line) as a function of GaN layer thickness for 750 and 900 °C growth temperature. Reproduced from [107] under a Creative Commons license.

Therefore, it seems reasonable to assume, as a first approximation, an exponential temperature dependence. By applying Arrhenius' law to the critical thickness of GaN on AlN template on sapphire and AlN single crystal (see dashed line in Fig. 4.6), an activation energy of 1.1 and 1.6 eV can be extracted, respectively. Furthermore, as discussed previously, an activation energy of 2 eV is observed for the temperature dependence of the strain relaxation rates (Fig. 4.5). These values are in good agreement with the activation energy for dislocation motion (2.1 eV) suggested by Sugiura [114]. The estimation is based on an empirical comparison between activation energy and band gap energy in various material groups. Additionally, Yonenaga *et al.* experimentally determined an activation energy of 2-2.7 eV [82] by performing mechanical yield stress measurements. Theoretical calculations performed by Holec *et al.* incorporate the dislocation core into the energy minimization model and predict core energies of 1.6 and 3.1 eV for a-type (edge, $b = 1/3\langle 11\bar{2}0\rangle$) and $(a{+}c)$-type (mixed, $b = 1/3\langle 11\bar{2}3\rangle$) dislocations [78]. It is suggested that the experimentally observed activation energies are related to the Peierls force, which creates kinetic barriers hindering dislocation motion [77]. The magnitude of this hindering force is strong for slip systems with large Burgers vectors such as c-type and $(a{+}c)$-type dislocations, whereas a smaller force is expected for a-type dislocations. These results suggest that the experimentally determined activation energies could possibly be related to the creation of specific types of dislocations. Detailed studies by transmission electron microscopy are needed to further investigate the strain relaxation process and the type of dislocations that are involved. Finally, the strain state and surface morphology of 30 ML thick (8 nm) GaN layers grown at low temperature (750 °C) on AlN was investigated by reciprocal space mapping (RSM) and AFM. This was performed both

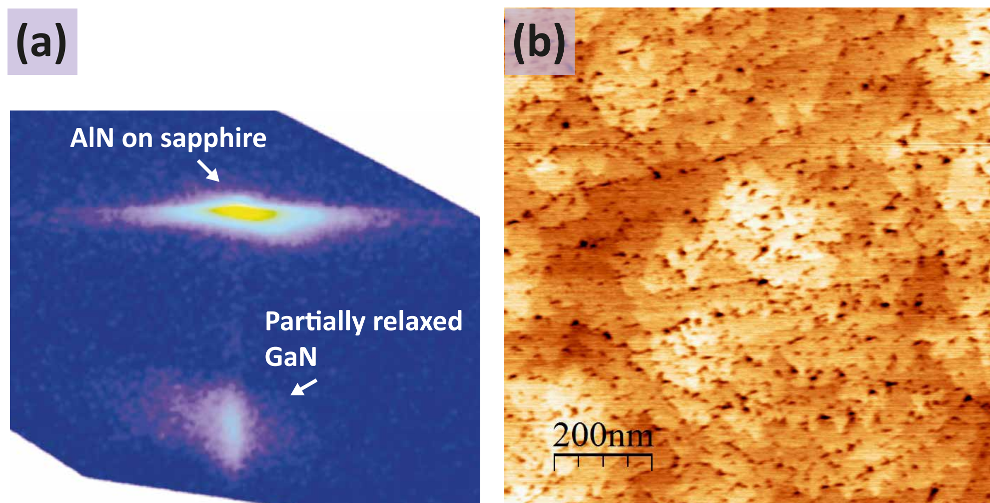

Figure 4.10 – (a) RSM and (b) 1×1 μm^2 AFM scan of 8 nm GaN grown on AlN template on sapphire at 750 °C with a root mean square roughness of 0.36 nm. Reproduced from [107] under a Creative Commons license.

on AlN template on sapphire and AlN single crystal. The RSM for the growth on sapphire (Fig. 4.10(a)) displays a partially relaxed GaN layer, which is expected, since the critical thickness at 750 °C is ~16 MLs. The AFM scan in Fig. 4.10(b) clearly shows a flat surface morphology with small pits possibly due to the generation of a high density of dislocations. In contrast, the growth performed on AlN single crystal exhibits a fully strained (pseudomorphic) GaN layer (see sharp GaN reflection in RSM given in Fig. 4.11(a)). This confirms the fact that thick GaN layers can be grown on AlN well above the near-equilibrium critical thickness of 3 MLs. The corresponding AFM scans in Fig. 4.11(b-c) exhibits a smooth surface morphology with a root mean square (rms) roughness of 0.4 nm over a 1×1 μm^2 scan. The roughness increases slightly (0.8 nm) for a 10×10 μm^2 scan. The surface morphology is characteristic of growth in the transition regime between step-meandering and hillocks due to Ehrlich-Schwöbel barrier effects at low temperature [115]. In order to achieve pseudomorphic GaN layers at low temperatures with improved surface morphology, growth parameters such as the V/III ratio and growth rate need to be optimized.

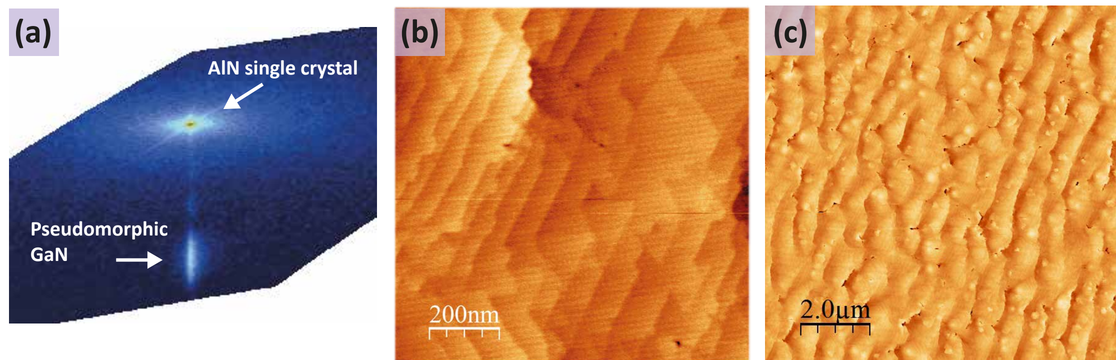

Figure 4.11 – (a) RSM of 8 nm thick GaN layer grown on AlN single crystal at 750 °C. 1×1 μm^2 with RMS roughness of 0.4 nm. (b) and (c) 10×10 μm^2 AFM scans showing the surface morphology of the layer with RMS roughness of 0.8 nm. Reproduced from [107] under a Creative Commons license.

4.3 Growth interruptions

In the previous section, the impact of temperature on the strain relaxation process during growth of GaN on AlN was discussed. With increasing thickness, the strain energy in the GaN layer increases. At the critical thickness, the strain is relieved by the introduction of dislocations. Furthermore, the strain relaxation rate above the critical thickness was shown to be strongly temperature dependent. At high temperature (850 °C), dislocation mobility is high and leads to multiplication of dislocations, whereas at low temperature (750 °C) dislocation motion is hindered and strain is frozen out. In order to investigate the impact of temperature on strained layers, the evolution of the lattice-mismatch was monitored during growth interruptions. In Fig. 4.12, the evolution of the lattice-mismatch is shown for both continuous and interrupted growths at 750 °C. The continuous growth (purple curve) exhibits the typical strain relaxation behavior. Above the critical thickness (at ~ 100 s growth), the lattice-mismatch continuously increases. In the case of growth interruptions (blue, red and green curves), the growth was terminated at different times below and above the critical thickness. Interestingly, the strain relaxation stops in both cases as the growth is terminated. This result shows that strain relaxation at low temperature is determined only by the thickness of GaN grown above the critical thickness. In Fig. 4.13, growth interruptions at 750 and 850 °C are compared. At 750 °C (Fig. 4.13(a)), the continuous growth (black curve) exhibits strain relaxation as previously discussed. At the critical thickness, which is reached after ~ 100 s, the lattice-mismatch increases and continues to increase until the end of the growth. The blue curve on the other hand shows the evolution of the lattice-mismatch for a 60 s growth period followed by a growth interruption. As expected, the strain relaxation process in not initiated because the critical thickness occurs after 100 s of GaN growth and the lattice-mismatch remains unchanged. At 850 °C (Fig. 4.13(b)), on the other hand, the situation changes. The strain relaxation during continuous growth (black curve) occurs after ~ 25 s of GaN deposition, which in agreement with the fact that at high temperature the critical thickness is lower.

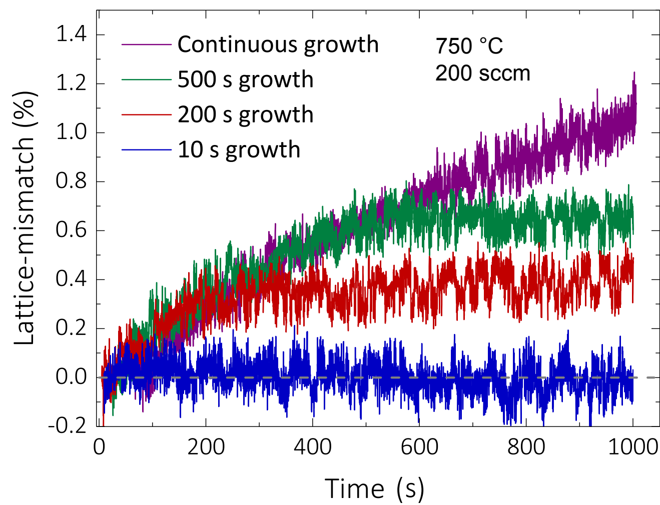

Figure 4.12 – Lattice-mismatch as a function of time for GaN grown on AlN template on sapphire at 750 °C. The strain relaxation of continuous growth (purple line) is compared to growth interruptions after 10, 200 and 500 s (blue, red and green lines), respectively.

The blue curve presents the strain relaxation for 60 s of GaN growth followed by a growth interruption. In this case, the strain continues to relax even though the growth has been terminated. This suggests that the increased dislocation mobility at high temperature allows for stronger interaction and multiplication of dislocations, leading to strain relaxation.

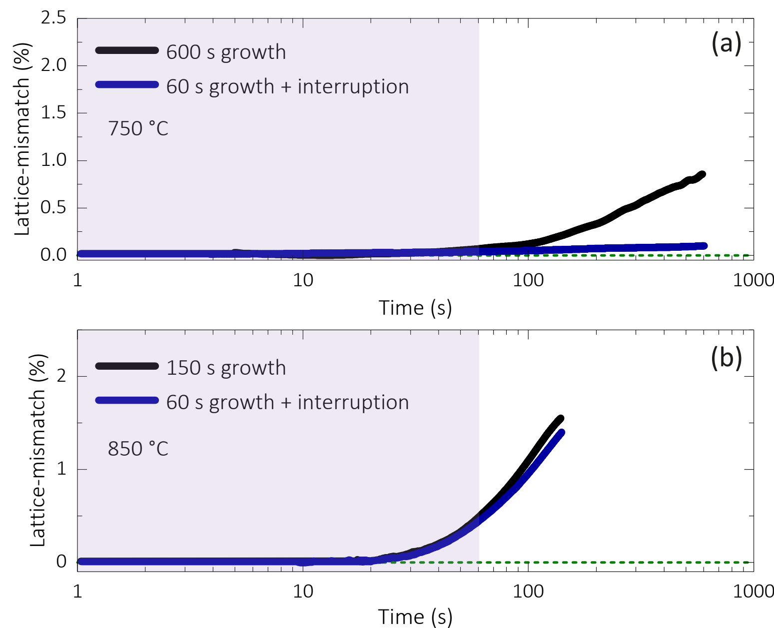

Figure 4.13 – Comparison in the evolution of lattice-mismatch of GaN on AlN template on sapphire as a function of time for continuous growth (black line) and growth interruption after 60 s (blue area) at (a) 750 °C and (b) 850 °C growth temperature.

4.4 Pseudomorphic growth

In this section, the growth of pseudomorphic GaN layers on AlN template on sapphire is discussed. As shown in the previous section, the critical thickness and the strain relaxation rate are strongly temperature dependent. At 750 °C, the critical thickness for strain relaxation of GaN on AlN template on sapphire is 16 MLs (~ 4 nm). In order to achieve larger thicknesses of fully strained GaN, the growth temperature needs to be further reduced. On the other hand, a lower growth temperature leads to kinetic surface roughening due to the reduced adatom mobility, which manifests itself by a spotty RHEED pattern. Therefore, there is a trade-off between lowering the growth temperature to increase the critical thickness and kinetic roughening. In order to investigate the growth mode and the strain state of GaN lay-

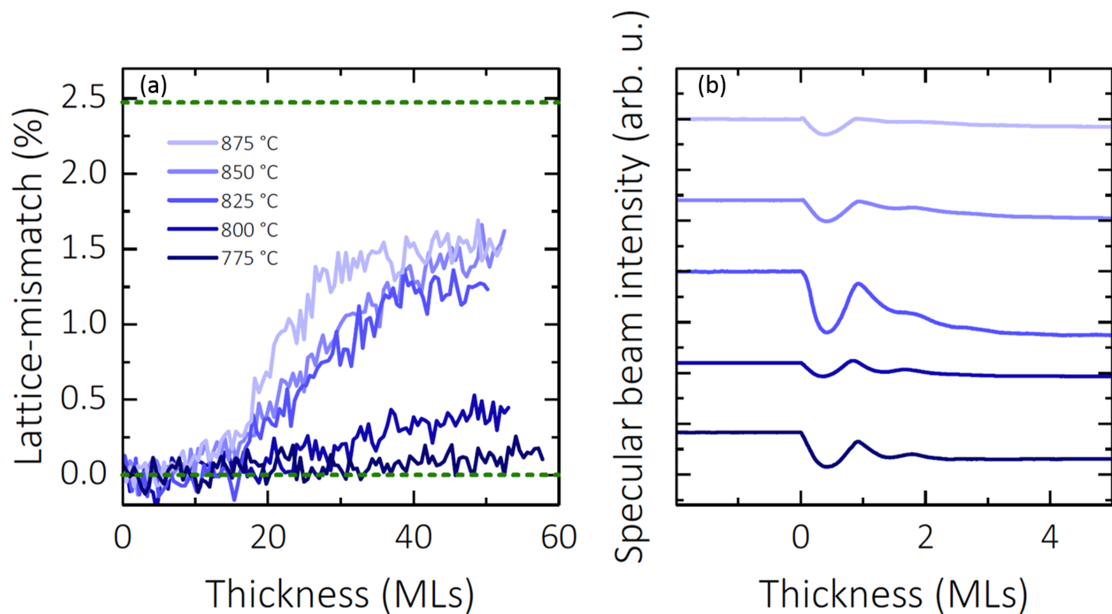

Figure 4.14 – Evolution of the lattice-mismatch (a) and specular beam intensity (b) as a function of layer thickness for GaN grown on AlN template on sapphire at different temperatures.

ers, the lattice-mismatch and the specular beam intensity were monitored as a function of growth temperature, as reported in Fig. 4.14. The NH_3 flow was kept at 200 sccm for these experiments. In Fig. 4.14(a), the impact of growth temperature on the strain relaxation is shown as a function of deposited GaN thickness. The strain relaxation rate increases strongly with temperature. The results are in agreement with the observations discussed in the previous section. In Fig. 4.14(b), the specular beam intensity is displayed as a function of GaN layer thickness at various temperatures. At low temperature (775 °C), clear oscillations are visible, which indicate a layer-by-layer growth mode. As the temperature is increased, the oscillations vanish, indicating a step-flow growth mode. In order to achieve step-flow growth at 775 °C, the surface diffusion length of adatoms needs to increase. Hence, the NH_3 flow was reduced by one order of magnitude (20 sccm) and the growth rate was also reduced from 0.3 to 0.1 ML/s. In Fig. 4.15 the resulting lattice-mismatch and specular beam intensity are

given for a growth of 50 MLs of GaN (blue curve). The strain relaxes as expected above the critical thickness and the specular beam intensity remains free of oscillations with a slight decrease in intensity possibly due to surface kinetic roughening [116]. The same growth was then repeated and stopped after 20 MLs of deposition. The results are shown in Fig. 4.15 (red curve). The calibration step before the actual growth can be used to verify whether the GaN layer will indeed be fully pseudomorphic and grown in a step-flow growth mode. In a next step, the surface morphology of the fully pseudomorphic GaN layers grown on AlN were investigated. In Fig. 4.16(a), the AFM scan of 4 nm thick GaN layers grown on AlN template on

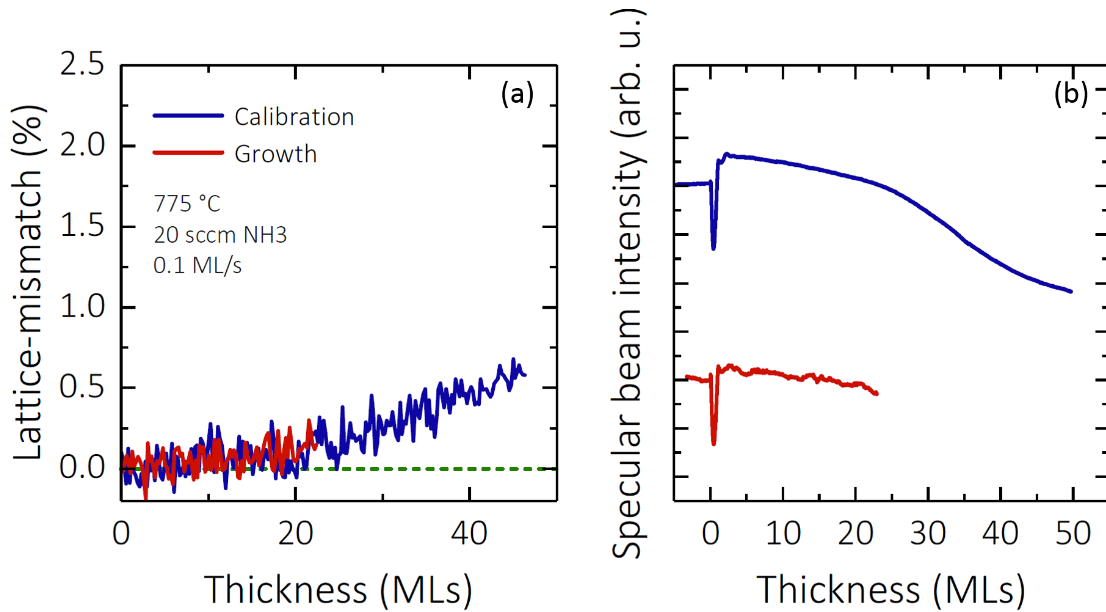

Figure 4.15 – Evolution of lattice-mismatch (a) and specular beam intensity (b) as a function of GaN grown on AlN template on sapphire at 775 °C. The calibration and growth curves are shown in blue and red, respectively.

sapphire at 775 °C (above the critical thickness) is shown. As expected, a high density of pits is present on the surface, which is probably related to the onset of plastic strain relaxation. In order to increase the critical thickness, the growth temperature was systematically lowered to 700 °C. The resulting AFM scans are shown in Fig. 4.16(b-d). As the temperature is lowered, the pits vanish. Furthermore, the RMS surface roughness decreases from 1.3 to 0.6 nm as the temperature is lowered to 700 °C (Fig. 4.16(e)). The spiral growth at screw dislocations is clearly visible for all temperatures and is the main source of surface roughening. Setting the temperature to 700 °C thus enables the growth of fully pseudomorphic layers of GaN (4 nm) on AlN with a good surface morphology. In a next step, these growth conditions were used to grow even thicker GaN layers (10 nm) on AlN. The AFM scan of the resulting layer shown in Fig. 4.17(a) exhibits a smooth surface with clear visible terraces.

Finally, the AFM scan in Fig. 4.17(b) shows the morphology of a 10 nm GaN layer grown under the same conditions as discussed in Fig. 4.17(a) followed by 10 nm of AlN. Interestingly, there are two distinct contributions to the roughening, (i) the previously discussed large scale

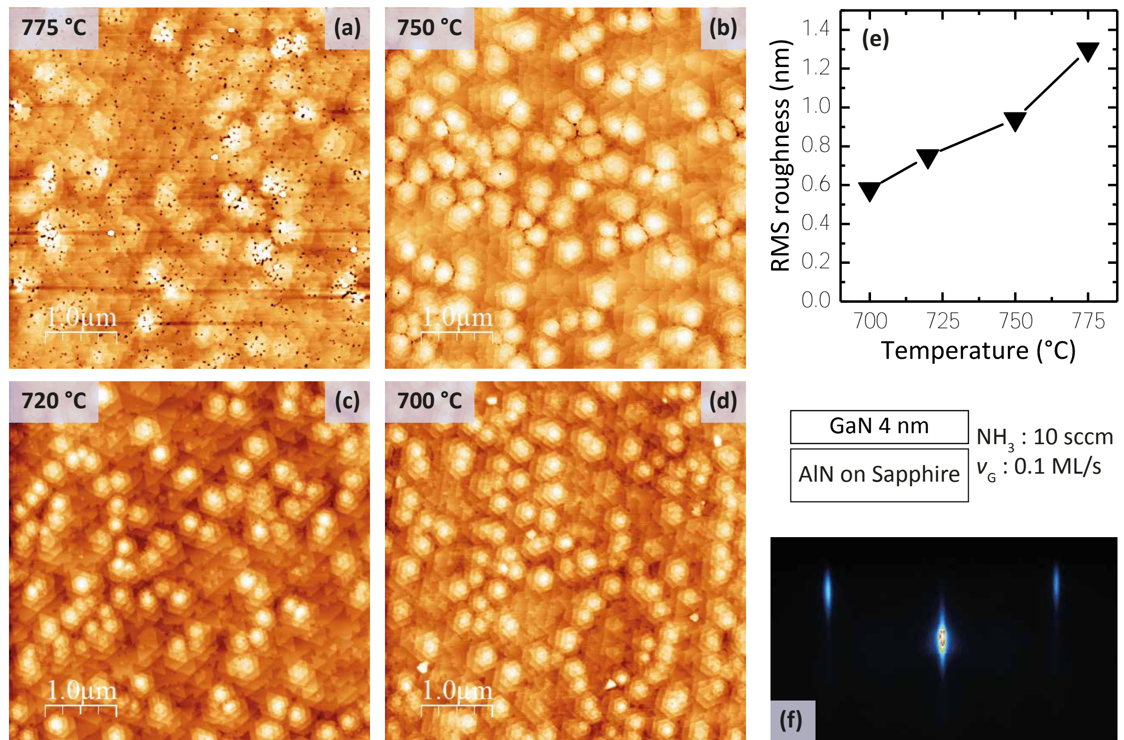

Figure 4.16 – Evolution of surface morphology of a 4 nm thick GaN layer grown on AlN template on sapphire by MBE. (a)-(d) 5×5 μm^2 AFM scans for a growth temperature range between 775 and 700 °C. (e) RMS roughness determined by AFM as a function of growth temperature for 5×5 μm^2 scans. (f) Sharp RHEED reflections after growth of GaN on AlN at 700 °C.

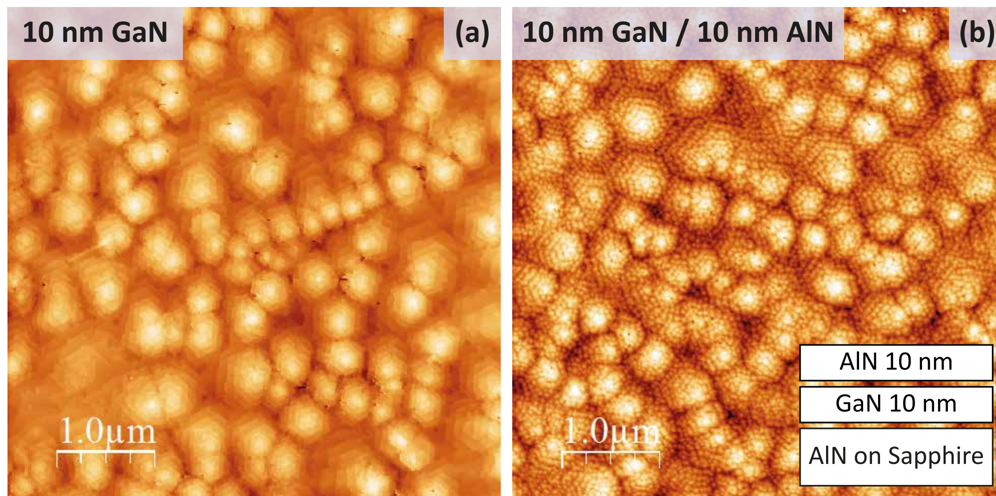

Figure 4.17 – 5×5 μm^2 AFM scans for (a) a 10 nm thick GaN layer (RMS roughness of 1.2 nm) and (b) 10 nm AlN / 10 nm GaN on AlN template on sapphire (RMS roughness of 1.3 nm).

(1μm) hills originating from the underlying GaN layer and (ii) the small scale (50 nm) roughening due to the low adatom mobility of Al during the growth of the AlN top layer. The challenges of growing highly strained AlN/GaN/AlN heterostructures with sharp interfaces will be discussed in the following chapter.

4.5 Summary

In this chapter, the critical thickness for plastic strain relaxation of GaN on AlN was determined by monitoring the *in-plane* lattice constant *in situ* by RHEED. The critical thickness is equal to 3 MLs on both AlN template on sapphire and AlN single crystal at 900 °C, which is in agreement with the near-equilibrium value predicted by theory. As the temperature is lowered (750 °C), the strain relaxation process freezes out and the critical thickness drastically increases to 16 and 35 MLs for AlN template on sapphire and AlN single crystal with an initial dislocation density of 10^9 and 10^3 cm^{-2}, respectively. Furthermore, the strain relaxation rate is strongly temperature dependent. An activation energy of 2.2 eV was extracted from the strain relaxation slopes. Growth interruption measurements revealed that, at 850 °C, the strain relaxation is governed by temperature. On the other hand, at 750 °C the layer thickness determines the evolution of relaxation relief. Finally, pseudomorphic growth of GaN with smooth surface morphology was achieved at 700 °C.

5 AlN/GaN/AlN heterostructures

In this chapter, thin GaN channel 2DEGs grown on AlN are discussed. In particular, the origin for the currently reported low electron mobility in AlN/GaN/AlN heterostructures is investigated.

5.1 Background

III-nitride based 2DEGs based on thin GaN channels grown on AlN are very promising for HEMTs operating at high frequency and high power. (i) AlN is an excellent thermal conductor (300 W m^{-1} K^{-1}) and perfect electrical insulator (6.00 eV), which allows for efficient heat management and low buffer leakage, respectively; (ii) the 2DEG resides within the thin GaN channel, leading to strong confinement; (iii) the AlN buffer acts as a natural back-barrier preventing a spill-over of the 2DEG from the channel into the buffer and (iv) in the particular case of AlN barriers, the large spontaneous polarization-mismatch between GaN and AlN allows for high carrier densities (> 1×10^{13} cm^{-2}), while maintaining a thin barrier thickness (< 3 nm). This could potentially enable record high frequency operation. In recent years, several groups have reported on the electronic properties of GaN channels grown on AlN. In case of thick quasi-bulk GaN channels (> 100 nm) the electron mobilities reach reasonably high values (> 1000 cm^2 V^{-1} s^{-1}) while maintaining a high carrier density (1 to 3×10^{13} cm^{-2}) for AlN [45, 46], AlGaN [47] and InAlN [48] barriers. On the other hand, for thin GaN channels (< 100 nm), the electron mobility strongly deteriorates with values generally below 600 cm^2 V^{-1} s^{-1} [42, 44, 117, 118].

In order to explain the drastic decrease in electron mobility for thin GaN channel 2DEGs grown on AlN, several hypotheses have been proposed over the years: (i) the strong electron-phonon coupling in thin GaN channels enhances phonon-scattering leading thereby to a low electron mobility. This theory can be discarded given the fact that the electron mobility in these structures remains low even at 30 K, where phonons can generally be neglected. (ii) The presence of a two-dimensional hole gas (2DHG) due to the negative polarization charge present at the bottom interface of the GaN channel. Since holes in III-nitrides have a much larger effective mass than electrons, there might exist a conduction path in addition to the

2DEG with a much lower electrical conductivity. Therefore, the experimentally measured effective mobility would be lower due to the presence of parallel conduction through the 2DHG. This hypothesis is also unlikely, since the low electron mobility remains even when the 2DHG is depopulated. This will be further discussed in the final section of this chapter.
In this chapter, the low electron mobility of thin GaN channel 2DEGs is investigated. The likely scattering mechanism must originate from one of the following parts of the heterostructure: (i) the GaN channel, (ii) the barrier or (iii) the substrate. In the following sections, each part will be studied individually by a series of experiments.

5.2 Channel thickness

In a first step, the impact of the GaN channel thickness on the electron mobility of AlN/-GaN/AlN heterostructures is investigated. The growth temperatures for the GaN channel and AlN barrier were 850 and 780 °C, respectively. The reason for choosing these temperatures is related to an interface instability between GaN and AlN, which will be discussed in the following section. A series of samples were grown by NH_3-MBE on AlN templates on sapphire with a nominally 4 nm thick AlN barrier and a GaN channel thickness ranging from 10 to 70 nm. The electron mobility and carrier density of these samples are depicted in Fig. 5.1. The

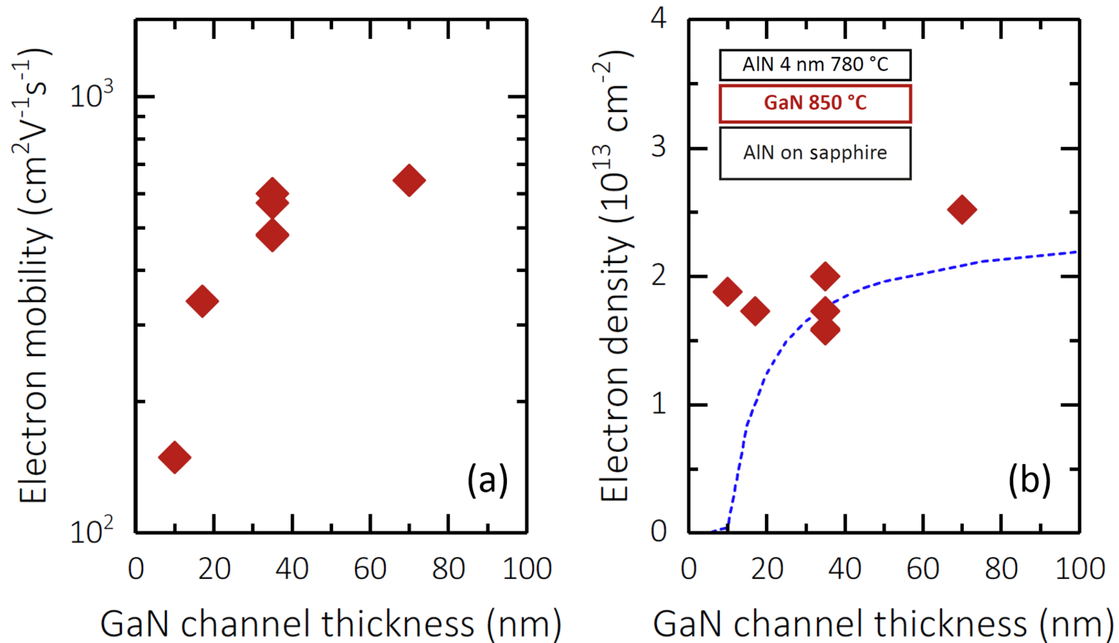

Figure 5.1 – Room temperature (a) electron mobility and (b) carrier density of AlN/GaN/AlN heterostructures grown on AlN template on sapphire as a function of GaN channel thickness. The blue dashed line corresponds to theoretical calculations. (Inset) Illustration of sample structure.

electron mobility rapidly increases from 150 to 650 $cm^2\ V^{-1}\ s^{-1}$ as the GaN channel thickness is increased, which is in agreement with the trend observed in literature. Interestingly,

the carrier density remains almost constant for all thicknesses. Furthermore, temperature-dependent Hall effect measurements were performed (Fig. 5.2).

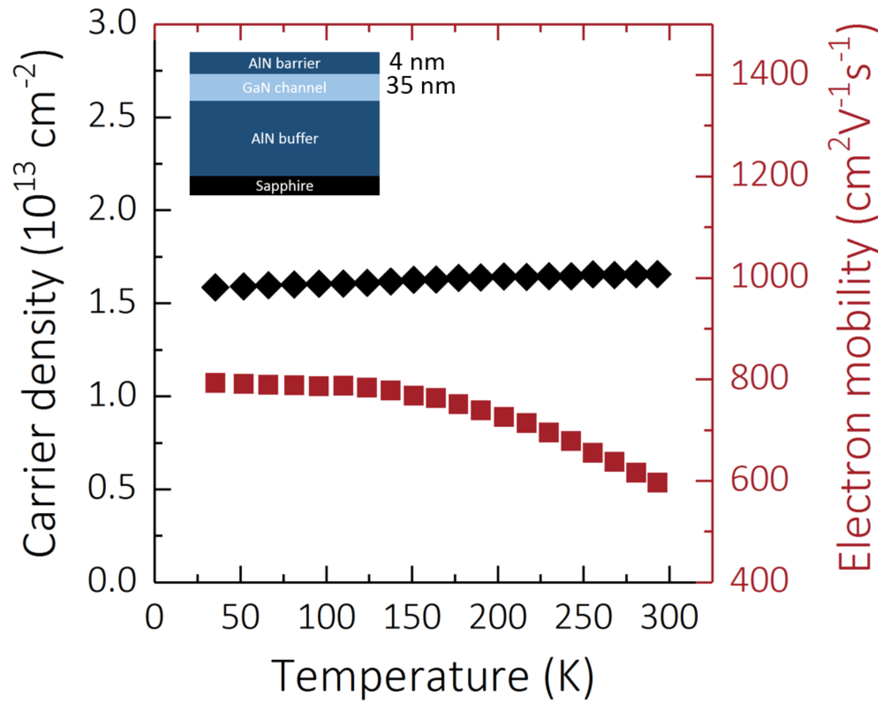

Figure 5.2 – Temperature-dependent Hall effect measurements of an AlN/GaN/AlN heterostructure showing the extracted carrier density (black diamonds) and electron mobility (red squares).

As expected, the carrier density (black diamonds) is almost constant as a function of temperature from 300 K to 30 K, confirming the presence of a 2DEG. Interestingly, the electron mobility only changes slightly from 600 to 800 cm^2 V^{-1} s^{-1} as the temperature is decreased, suggesting that the limiting scattering mechanism is temperature-independent. In Fig. 5.3, the evolution of the surface morphology is displayed as a function of the GaN channel thickness. For 10 nm thick GaN (Fig. 5.3(a)), the surface exhibits an uncoalesced morphology, which is due to the rapid strain relaxation of GaN on AlN at high temperatures. With increasing thickness, the GaN layer coalesces, which reduces the pit density (black areas) and improves the surface morphology. At the same time, the electron mobility increases and reaches a value of 650 cm^2 V^{-1} s^{-1}. One could argue that the increase in electron mobility is related to the reduction of the pit density. However, this hypothesis can be ruled out, since similar structures have been reported in literature having no pits and exhibiting even lower electron mobilities [117]. Interestingly, these results were obtained by PA-MBE, which is performed at considerably lower temperatures (600 to 700 °C) for both the GaN channel and the AlN barrier. In order to investigate the impact of growth temperature on the electronic properties, a series of samples were grown as a function of temperature ranging from 700 to 850 °C (Fig. 5.4). For these structures, the GaN channel and AlN barrier were grown at the same temperature.

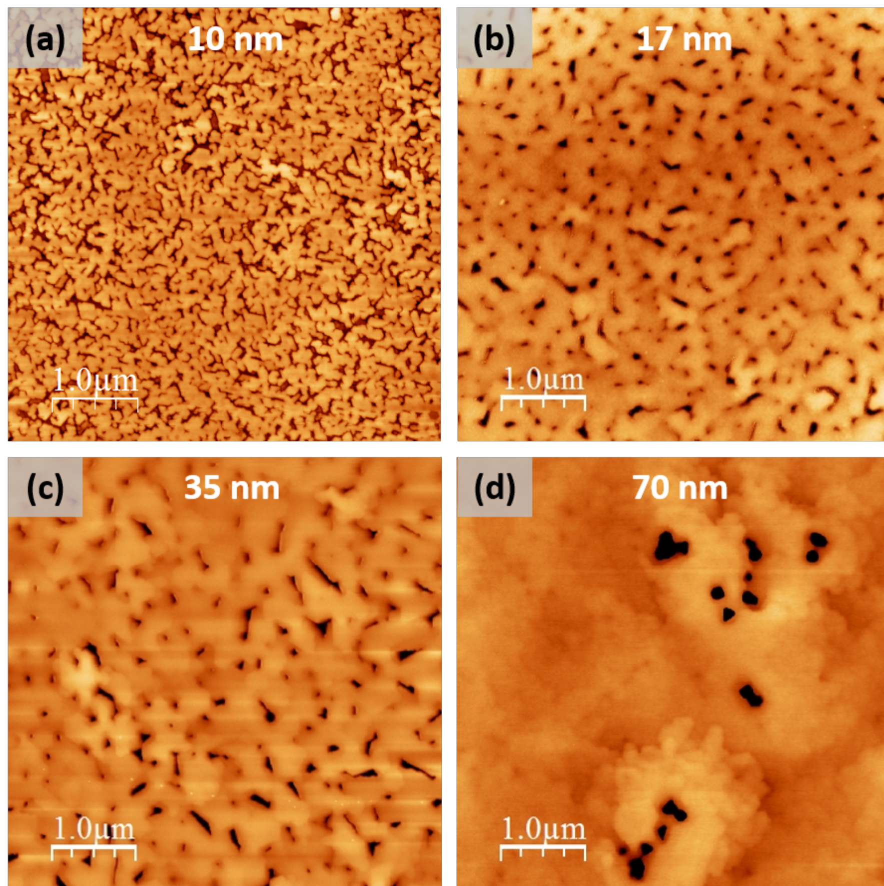

Figure 5.3 – 5×5 μm^2 AFM scans of AlN/GaN/AlN heterostructures with a GaN channel of (a) 10 nm (RMS surface roughness 3.6 nm), (b) 17 nm (RMS surface roughness 1.4 nm), (c) 35 nm (RMS surface roughness 5.7 nm) and (d) 70 nm thick GaN (RMS surface roughness 3.2 nm) channel thicknesses.

The electron mobility strongly increases as the growth temperature is increased from 700 to 800 °C. Above 800 °C, the electron mobility rapidly drops, which is surprising, considering that with increasing temperatures one would expect an improvement of crystal quality and surface morphology. However, the results on the temperature-dependent strain relaxation of GaN grown on AlN obtained in the previous chapter suggest a possible role of strain and/or dislocations. Moreover, the electron mobility shown in Fig. 5.1 seems to saturate at a value of ~ 600 - 650 $cm^2 V^{-1} s^{-1}$ as the GaN thickness increases, which is surprising considering that for AlN barriers grown on thick GaN buffers, high electron mobilities ~ 2000 $cm^2 V^{-1} s^{-1}$ [9, 34] can be achieved.
In the following section, the impact of strain and growth temperature of the AlN barrier on the electron mobility of thin GaN channels is discussed.

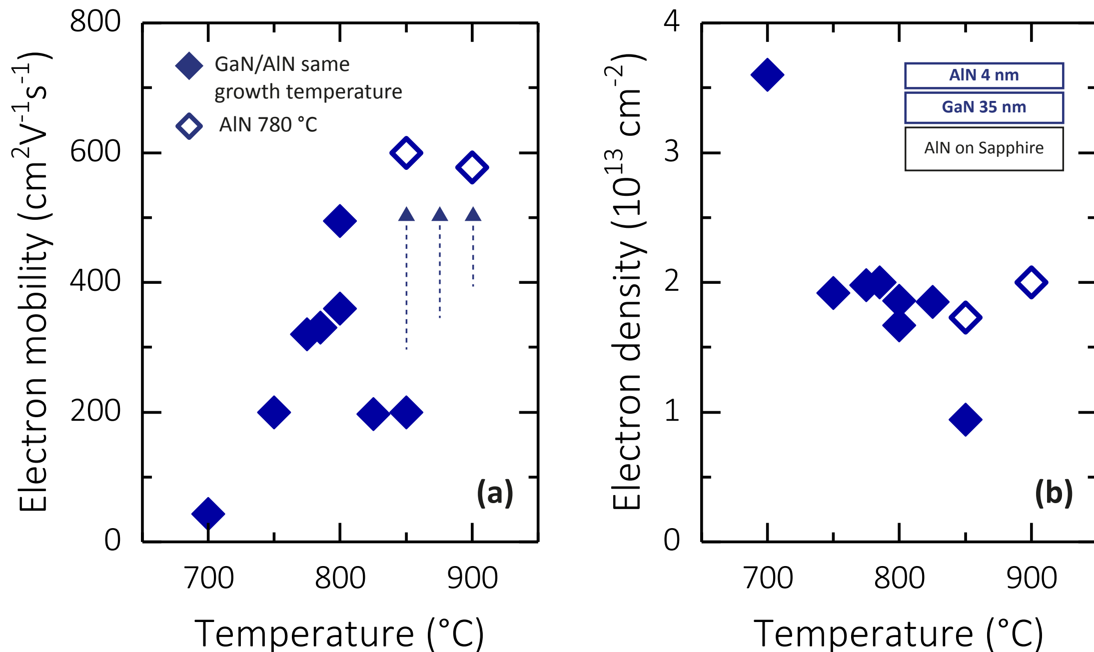

Figure 5.4 – Room temperature (a) electron mobility and (b) carrier density of AlN/GaN/AlN heterostructures grown on AlN template on sapphire as a function of growth temperature. The AlN barrier growth temperature was the same as that of the GaN channel in case of the filled blue diamonds and was reduced to 780 °C for the empty blue diamonds. (Inset) Sketch of the sample structure.

5.2.1 AlN/GaN interface instability

The impact of AlN barrier growth temperature was studied by growing a series of samples with GaN channels (35 nm thick) at 850 °C followed by the AlN barrier (4 nm thick) in a temperature range going from 700 to 850 °C. The resulting electronic properties are reported in Fig. 5.5. The electron mobility increases from 350 to 510 cm^2 V^{-1} s^{-1} as the barrier growth temperature is increased from 700 to 800 °C. With increasing growth temperature, the Al-adatom mobility increases leading to an improved AlN/GaN interface quality and hence improved electron mobility. Therefore, at low temperatures (700 °C) the electron mobility is limited by interface roughness scattering (blue shaded area in Fig. 5.5). Surprisingly, the electron mobility drastically drops as the growth temperature is increased above 800 °C (pink shaded area). The strong temperature dependence of the electron mobility can be explained when considering the thermodynamic stability of the AlN/GaN interface. Theoretical investigations performed by Laks and Zunger have shown that the interface between two binary semiconductors (e.g. III-V semiconductors) can be unstable in terms of sharpness [119]. Thermodynamics imposes two obstacles for the abruptness of the interface: (i) Exposure of semiconductor heterostructures to high temperatures can lead to inter-diffusion of the constituent atoms at the interface. This disorder is favored by the entropy term ($-TS$) and makes an alloyed interface energetically more stable. (ii) Even at $T = 0$ K an abrupt interface can

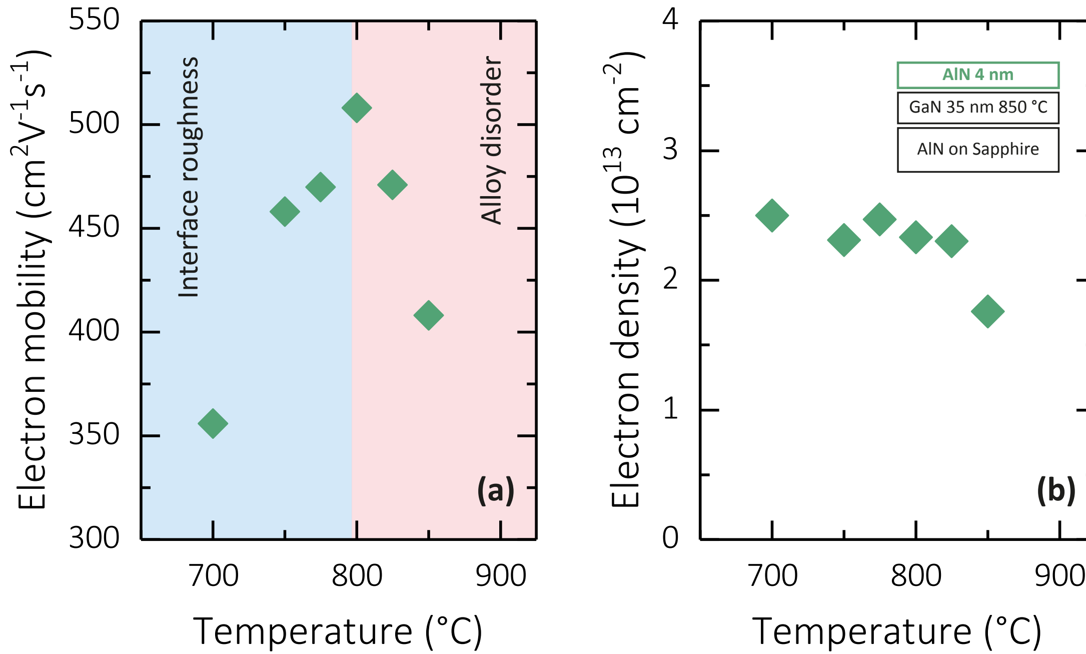

Figure 5.5 – Room temperature (a) electron mobility and (b) carrier density of AlN/GaN/AlN heterostructures grown on AlN template on sapphire as a function of AlN barrier growth temperature. (Inset) Illustration of sample structure.

have a higher formation enthalpy than the random alloy due to the presence of excess elastic energy (strain). In the particular case of III-nitrides, the interface instability is even more severe due to the large electronegativity of nitrogen (ionic chemical bond) and the lattice-mismatch between AlN and GaN [120]. These properties lead to both higher growth temperatures and higher elastic strain energies compared to conventional III-V semiconductors. For example, the well/barrier interface of multiple quantum wells (AlN/GaN) grown by PA-MBE have been shown to be sharp [121], whereas by MOVPE (higher growth temperature), the instability leads to graded interfaces [122]. Furthermore, the strain state of the heterostructure (fixed by the substrate, i.e. AlN or GaN) leads to significant differences in the interface stability. In Fig. 5.6, the situation is illustrated for the case of GaN quantum wells grown on AlN. The first interface remains sharp, whereas the second one is unstable and rough. Furthermore, atom probe tomography (APT) measurements demonstrate the impact of growth temperature on the inter-diffusion at the interface [123]. In Fig. 5.7, APT measurements for AlGaN/GaN structures grown by PA-MBE, NH_3-MBE and MOVPE are shown. For the growth by PA-MBE, the AlN spacer between the AlGaN barrier and GaN buffer exhibits a sharp interface. On the other hand, for growth by NH_3-MBE and MOVPE, the AlN spacer becomes drastically less sharp. This clearly indicates that the elevated temperatures used in NH_3-MBE and MOVPE compared to PA-MBE lead to inter-diffusion at AlN/GaN interfaces. Thus the interface instability could explain the drastic drop in electron mobility observed in Fig. 5.5 above 800 °C due to the formation of an alloy (AlGaN) at the heterostructure interface. Hence,

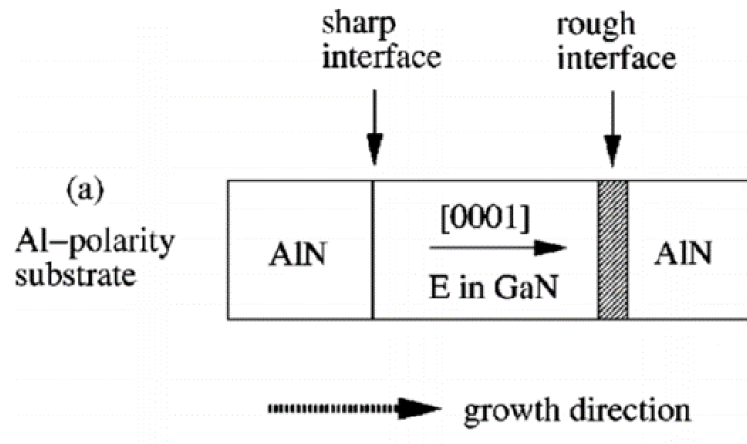

Figure 5.6 – Illustration of the instability at the AlN/GaN interface. Reproduced and modified from [120] with permission from APS.

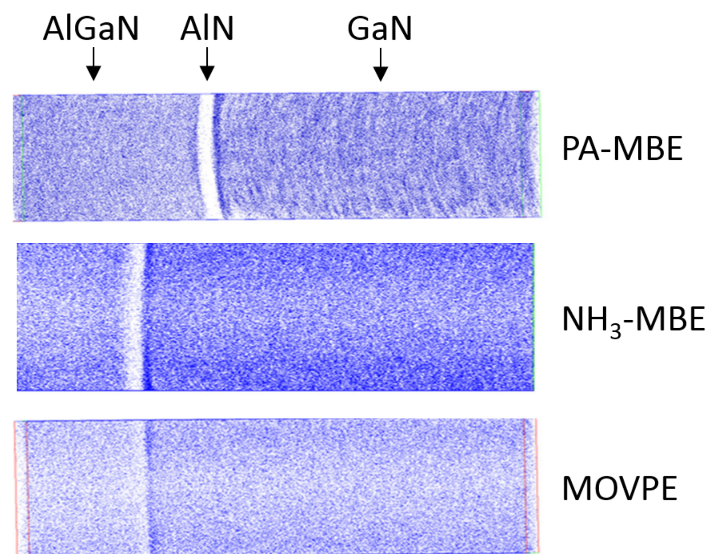

Figure 5.7 – Atom probe tomography of AlGaN/GaN heterostructures grown by (a) PA-MBE, (b) NH_3-MBE and (c) MOVPE. Reproduced and modified from [123] with permission from AIP.

the electron mobility decreases due to alloy disorder scattering (red shaded area in Fig. 5.5). For an AlN barrier growth temperature below 780 °C, the AlN/GaN interface remains sharp and the electron mobility increases to above 600 $cm^2 V^{-1} s^{-1}$ (blue hollow diamonds in Fig. 5.4). However, the electron mobility still remains limited to ~ 600 $cm^2 V^{-1} s^{-1}$. In order to investigate whether the low electron mobility in AlN/GaN/AlN heterostructures is due to the interface instability, a series of samples were prepared with AlGaN barriers grown on GaN channels of increasing thickness on AlN templates on sapphire.

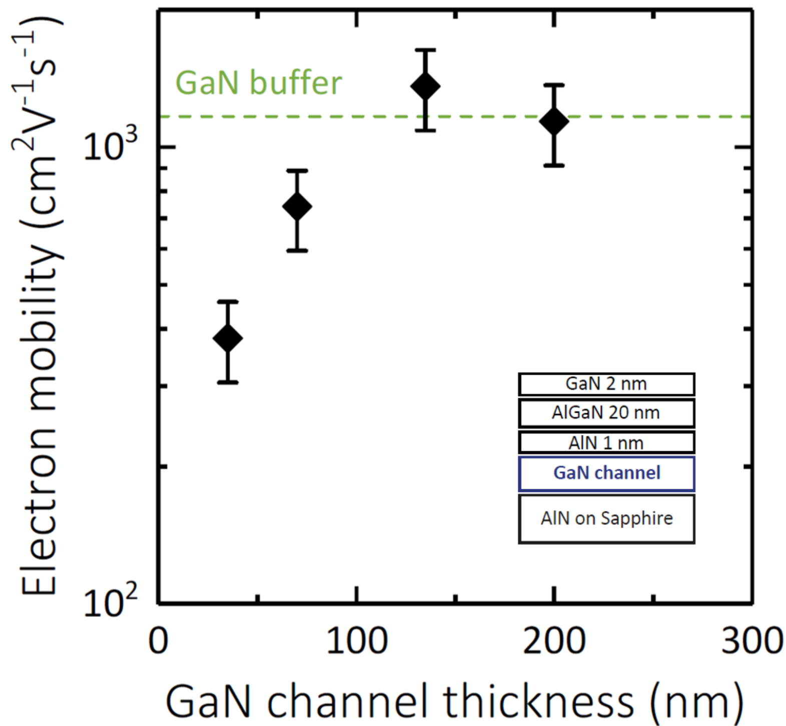

Figure 5.8 – Room-temperature electron mobility of $Al_{0.3}Ga_{0.7}N/GaN$ heterostructures grown on AlN template on sapphire as a function of GaN channel thickness. The inset shows the sample structure.

The resulting electron mobility is given in Fig. 5.8 as a function of GaN channel thickness. The electron mobility increases with GaN thickness, which is the same trend than the one observed with AlN barriers. However, in the case of AlGaN barriers, the electron mobility reaches values above 1200 $cm^2\,V^{-1}\,s^{-1}$ for a GaN channel thicker than 135 nm. Therefore, two things can be concluded: The limiting scattering mechanism is not related to (i) the interface instability and (ii) the type of barriers used. The second point will be discussed in more detail in the next section. In Fig. 5.9, the electron mobility of AlN, AlGaN barriers and literature values are given as a function of GaN channel thickness. The clear trend in electron mobility with increasing GaN thickness, suggests that the limiting parameter is closely related to the channel itself.

5.3 Barrier

As discussed in the previous section, the electron mobilities reported in literature for thin GaN channels strongly depend on the thickness of the GaN channel (red triangles in Fig. 5.9). This is interesting considering that the heterostructures were grown by different methods and by using various barriers. In order to investigate the impact of barrier-type, a series of samples were grown on AlN template on sapphire with a nominal GaN channel thickness of 70 nm followed by an AlN, AlGaN or InAlN barrier, respectively, as illustrated in Fig. 5.10.

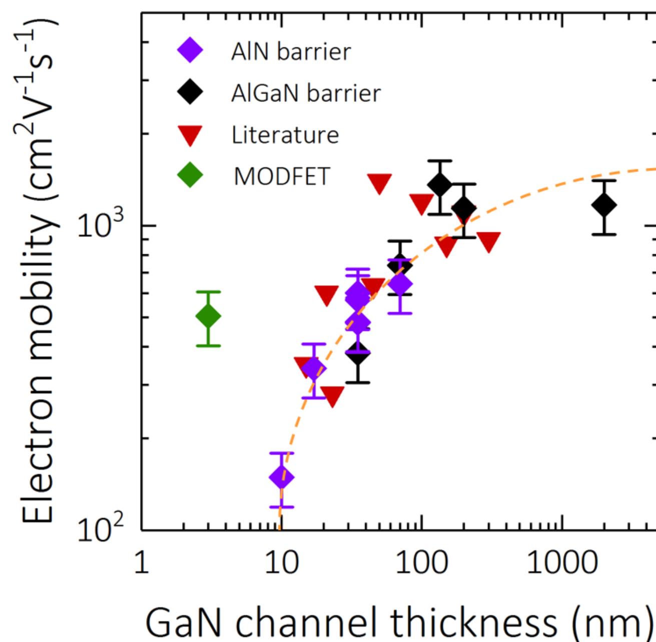

Figure 5.9 – Room-temperature electron mobility as a function of GaN channel thickness for AlN (purple diamond), AlGaN (black diamond) barriers and literature values [42–48] (red triangle). The orange dashed line is a guide to the eye illustrating the strong dependence of electron mobility on GaN channel thickness. The green diamonds represent a modulation-doped 3 nm thick GaN channel.

The samples with AlN and AlGaN barrier were grown by NH_3-MBE, whereas the InAlN heterostructure was grown by MOVPE. In Tab. 5.1, the electronic properties of the different samples are summarized. Interestingly, the electron mobility of the three structures is very similar. The electron density, on the other hand, decreases from 2.5 to 1.5 $\times 10^{13}$ cm^{-2}, which is due to the reduced polarization-mismatch between the barrier and GaN. Therefore, the low electron mobility is independent of the barrier-type and also the growth method. This further confirms that the key parameter for the mobility limitation must be related to the GaN channel.

Barrier	R_s (Ω/sq)	n_s (10^{13} cm^{-2})	μ (cm^2 V^{-1} s^{-1})
AlN	385	2.5	643
$In_{0.18}Al_{0.82}N$	630	1.9	522
$Al_{0.30}Ga_{0.70}N$	568	1.5	741

Table 5.1 – Room-temperature Hall effect measurements: Sheet resistance (R_s), carrier density (n_s) and electron mobility (μ) for GaN channels (70 nm thick) on AlN template on sapphire with AlN, InAlN and AlGaN barriers.

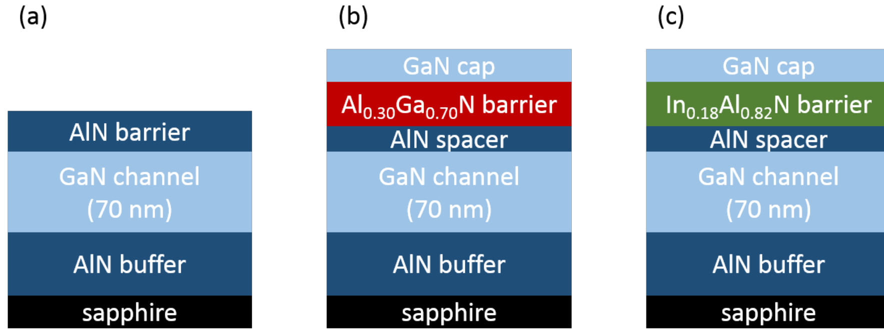

Figure 5.10 – Illustration of sample structures for 70 nm thick GaN channels grown on AlN template on sapphire with (a) AlN, (b) AlGaN and (c) InAlN barriers.

5.4 Dislocation-induced surface roughening

In the previous sections, it was shown that the low electron mobility is not related to the barrier/channel interface. Moreover, the channel thickness seems to play a crucial role in limiting the electron mobility. One of the main scattering mechanisms in III-nitride 2DEGs at low temperature is interface roughness at the barrier/channel interface. Since the substrates used so far have been AlN template on sapphire, it is conceivable that a high screw dislocation density (10^9 cm^{-2}) present in the substrate could lead to spiral growth induced roughening of the surface. In order to study the impact of the initial dislocation density on the surface morphology and electron mobility, two samples were prepared with an AlN barrier (10 nm) and GaN channel (10 nm) grown on two different substrates: (i) AlN template on sapphire and (ii) AlN single crystal with an initial dislocation density of 10^9 and 10^3 cm^{-2}, respectively. AFM scans of both samples are shown in Fig. 5.11. As expected, the growth on sapphire involves surface roughening induced by spiral growth (white dashed hexagon in Fig. 5.11(a)). On the other hand, the growth on AlN single crystal exhibits much lower surface roughness. Surprisingly, the electronic properties of the two samples are almost identical with a carrier density of 2×10^{13} cm^{-2} and electron mobility of 370 cm^2 V^{-1} s^{-1}. This suggests that the mobility limitation is not related to the initial dislocation density and the spiral-growth induced surface roughening.

5.5 Dislocation scattering

It is well known that dislocation densities as high as 10^{10} cm^{-2} originating from the substrate are not a dominating scattering mechanism in III-nitride 2DEGs at room temperature for typical carrier densities (1×10^{13} cm^{-2}). This is due to efficient screening of charged dislocations by the high carrier density, allowing for example, electron mobilities above 2000 cm^{2}V^{-1}s^{-1} on Si substrates with a dislocation density of ~ 5×10^9 cm^{-2} [124]. As discussed in Ch. 2 the electron scattering by charged dislocations can be expressed by the following simplified

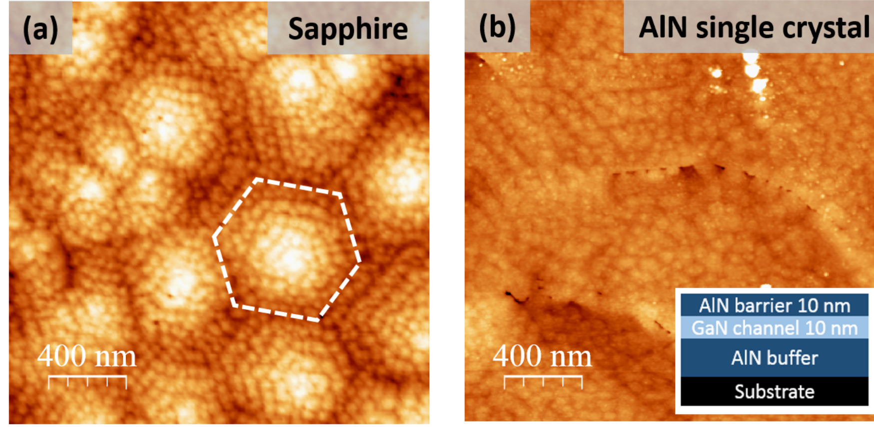

Figure 5.11 – 2×2 μm^2 AFM scans of AlN/GaN/AlN heterostructures grown on (a) AlN template on sapphire (RMS surface roughness 1.2 nm) and (b) AlN single crystal (RMS surface roughness 1.2 nm). The inset shows the sample structure.

equation [10]

$$\mu_{\text{Disl}} = 43365\left(\frac{10^8\text{cm}^{-2}}{N_{\text{Disl}}}\right)\left(\frac{n_s}{10^{12}\text{cm}^{-2}}\right)^{1.34}\left(\frac{1}{f_0^2}\right), \tag{5.1}$$

where N_{Disl} is the density of charged dislocations piercing the 2DEG, n_s is the carrier density and f_0 is the charge fraction of the dislocation which was set to 1 for the following calculations. In Fig. 5.12 the calculated room-temperature electron mobility is shown as a function of dislocation density for a fixed carrier density (1×10^{13} cm^{-2}). Only two contributions are considered for the total electron mobility (green curve), which was calculated by applying Matthiessen's rule: (i) phonon scattering (purple dashed line), which is assumed to be independent of the dislocation density and (ii) charged dislocation scattering (black dashed line) as described by Eq. 5.1. As expected, the total electron mobility is not affected by dislocations up to ~ 5×10^9 cm^{-2} and is solely limited by phonons (green area in Fig. 5.12). This is what allows for the high electron mobility heterostructures on Si discussed previously [124]. Higher dislocation densities (> 10^{10} cm^{-2}), on the other hand, cannot be efficiently screened by the carriers, and, therefore, the electron mobility reduces (pink area in Fig. 5.12). So far, only dislocations originating from the substrate were discussed with densities ranging from 10^3 to 10^9 cm^{-2} for growth on AlN single crystal and growth on AlN template on sapphire, respectively. However, the large lattice-mismatch between GaN and AlN must be taken into account. As discussed in the previous chapter, above the critical thickness, dislocations are introduced into the layer, which leads to plastic strain relaxation. At the initial stage of relaxation, the dislocation density is as high as 7×10^{11} cm^{-2} and reduces exponentially with increasing GaN thickness [83]. In Fig. 5.13, the calculated exponential decrease in dislocation density is shown as a function of GaN thickness. For this calculation, near-equilibrium growth conditions were assumed, which means that the critical thickness is 3 MLs. Furthermore, the dislocation density for quasi-bulk GaN thicknesses (> 100 nm) is assumed to be 5×10^9 cm^{-2},

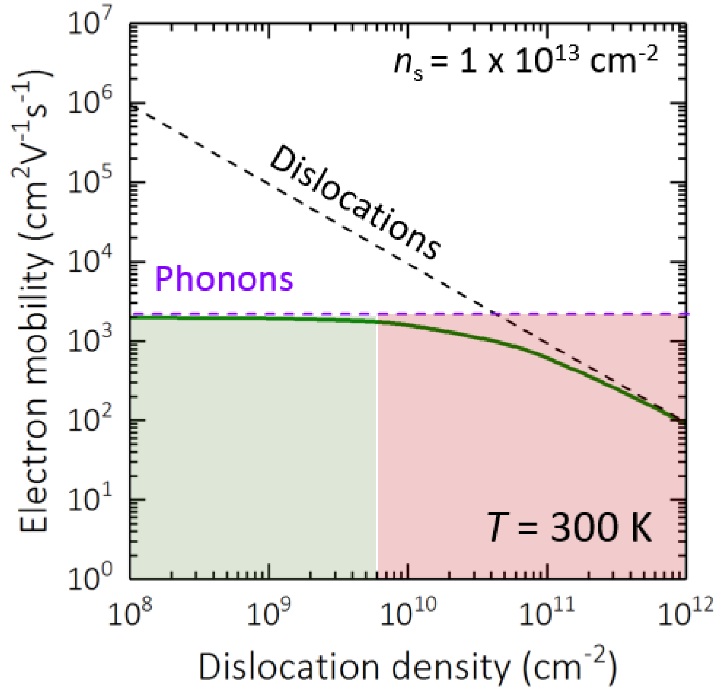

Figure 5.12 – Calculated electron mobility of a 2DEG with a carrier density of 1×10^{13} cm^{-2} as a function of dislocation density (black dashed line), phonon-limited electron mobility (purple dashed line) and the total electron mobility (green line). The green area indicates the dislocation density range at which the electron mobility is limited by phonon-scattering. In the pink area dislocation scattering becomes the dominating scattering mechanism.

which is in agreement with measured values [124]. In the initial stages of growth, the dislocation density is high and rapidly decreases with increasing GaN thickness. This suggests that the evolution of the electron mobility as a function of GaN channel thickness could be explained by dislocations. In order to test this hypothesis, a series of samples were grown with GaN channels (35 nm) on AlN template on sapphire with AlN barriers of increasing thickness from 2.5 to 8 nm. The electronic properties of the samples are shown in Fig. 5.14. As expected, the carrier density increases from 0.5 to 3.5 $\times$ 10^{13} cm^{-2}, which is in good agreement with Schrödinger-Poisson calculations (red dashed line in Fig. 5.14(a)). Interestingly, the electron mobility also increases with increasing barrier thickness (Fig. 5.14(b)), which can be attributed to the screening effect of the carrier density. In Fig. 5.15, the electron mobility is given as a function of carrier density. Furthermore, the experimental values were fitted (red dotted line in Fig. 5.15) by using Eq. 5.1 giving a dislocation density (N_{Disl}) of 5×10^{11} cm^{-2}, which is in good agreement with the reported value [83]. Therefore, the low electron mobility in thin GaN channels grown on AlN could be due to a high dislocation density piercing the 2DEG. With increasing GaN thickness, the dislocation density drops exponentially enabling high electron mobilities for GaN thicknesses above $\sim$ 100 nm with a dislocation density below 5×10^{9} cm^{-2}. In order to have direct evidence of high dislocation densities, transmission electron microscopy measurements need to be performed.

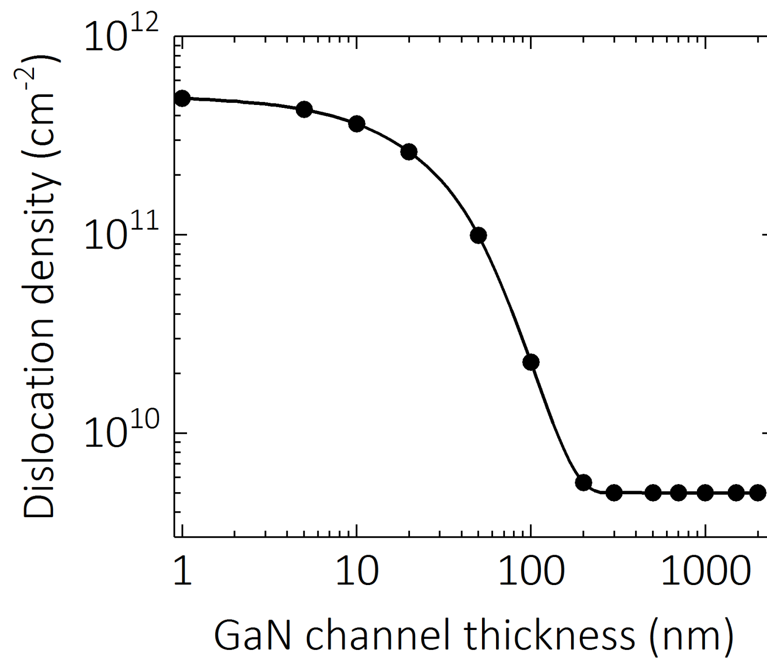

Figure 5.13 – Calculated dislocation density as a function of GaN channel thickness grown on AlN.

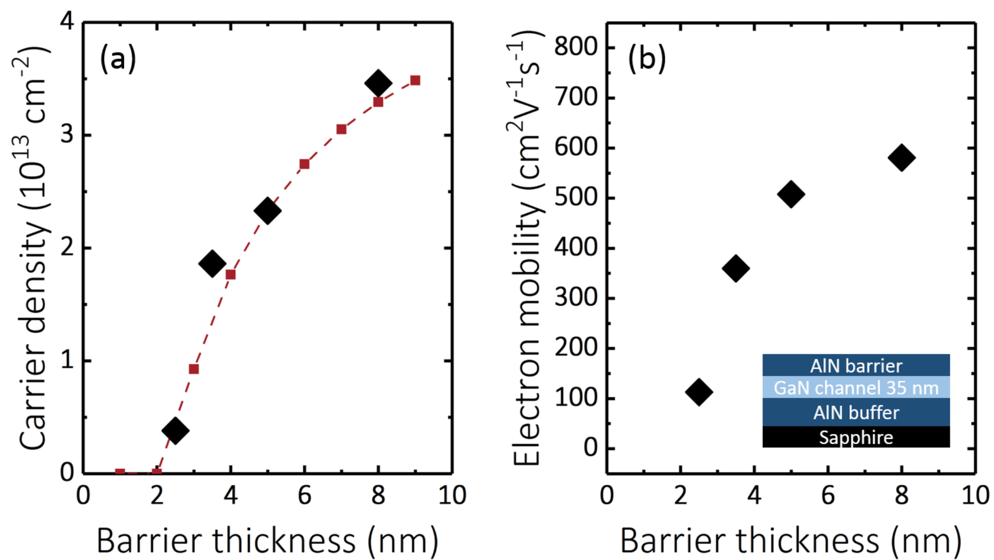

Figure 5.14 – Room temperature (a) electron mobility and (b) carrier density of AlN/GaN/AlN heterostructures grown on AlN template on sapphire as a function of AlN barrier thickness. The red dashed line corresponds to theoretical calculations. (Inset) Sketch of sample structure.

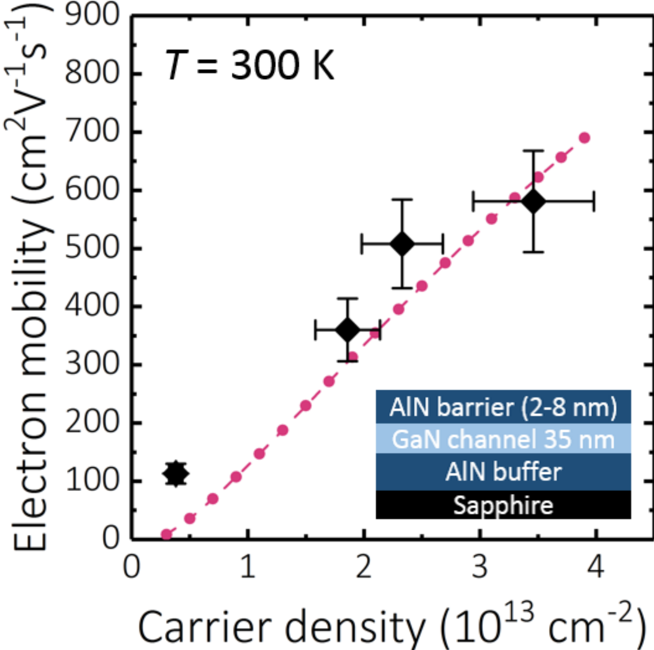

Figure 5.15 – Room-temperature electron mobility of AlN/GaN/AlN heterostructures as a function of carrier density. The red dash-dotted line is the calculated electron mobility. The inset shows the sample structure.

5.6 Modulation-doped heterostructures

In the previous section, the limiting scattering mechanism for thin GaN channel 2DEGs grown on AlN was investigated. A high dislocation density was suggested as the origin for the low electron mobility. Above the critical thickness of GaN on AlN, strain relaxation leads to a high density of charged dislocations, which cannot be screened by the 2DEG carriers. Hence, plastic strain relaxation should be avoided by keeping the GaN thickness below the critical value. As discussed in Chap. 4, the critical thickness can be increased by lowering the growth

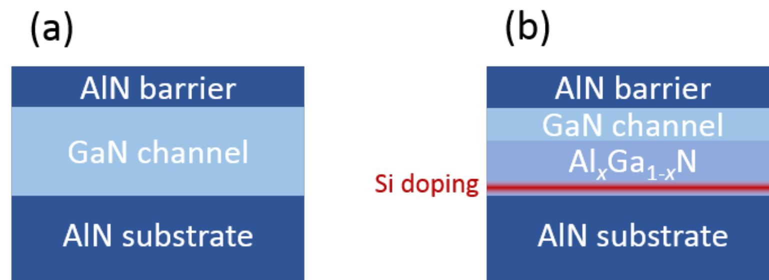

Figure 5.16 – Illustration of heterostructures with 2DEG channels induced by (a) spontaneous and piezoelectric polarization and (b) modulation doping using a Si-doped AlGaN back-barrier

temperature to 700 °C and optimizing the growth rate and NH_3 flow. This enables the growth of pseudomorphic GaN on AlN templates on sapphire with a thickness of 20 MLs (~ 5 nm). However, Schrödinger-Poisson calculations show that, by decreasing the GaN channel thickness, the carrier density of the 2DEG drastically reduces and fully diminishes at 5 nm. Therefore a 2DEG cannot be obtained purely by polarization-mismatch for pseudomorphic GaN channels as illustrated in Fig. 5.16(a). One potential solution is to supply the carrier density by modulation doping, while keeping the GaN channel thickness below the critical value. The idea of modulation doping of a heterostructure was developed in the 1980s for GaAs-based HEMTs [125–129].
The heterostructure shown in Fig. 5.16(b) consists of a GaN channel (3-5 nm) pseudomorphic to AlN grown under growth conditions discussed in the previous chapter. Modulation-doping occurs within a thin AlGaN back-barrier (5-10 nm) directly grown on the AlN substrate. Since the carriers are supplied by Si-doping, the AlN barrier can be arbitrarily thin (2-10 nm thick).

A series of samples were grown (illustrated in Fig. 5.17) in order to investigate the impact of the GaN channel thickness and modulation-doping on the electronic properties of the heterostructures (Tab. 5.2). In a first step, the impact of the GaN channel thickness was studied with a fixed 10 nm thick $Al_{0.5}Ga_{0.5}N$ back-barrier. Two structures were grown with 5 and 3 nm GaN channel thicknesses (Fig. 5.17(a-b)). The electron mobility decreases from 457 to 257 $cm^2\ V^{-1}s^{-1}$ as the GaN channel thickness is reduced from 5 to 3 nm. The drastic degradation of the electron mobility for 3 nm channel thickness could be related to interface

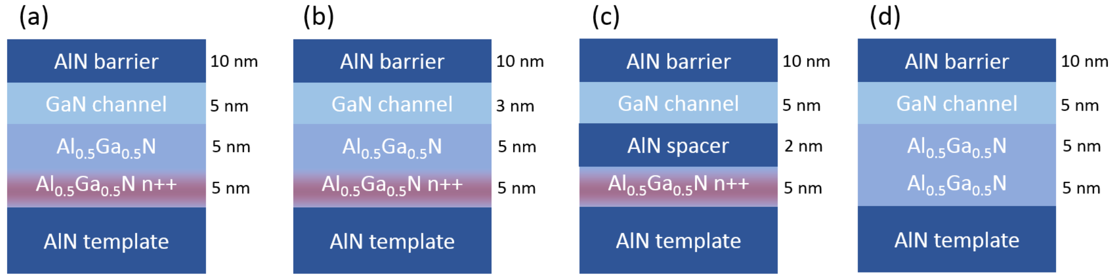

Figure 5.17 – Illustration of sample structures used to investigate the impact of modulation-doping in AlN/GaN/AlGaN/AlN heterostructures.

Sample	R_s (Ω/sq)	n_s (10^{13} cm^{-2})	μ (cm^2 V^{-1} s^{-1})
a	433	3.2	457
b	932	2.6	257
c	804	2.4	320
d	1990	0.9	326

Table 5.2 – Room-temperature Hall effect measurements: Sheet resistance (R_s), carrier density (n_s) and electron mobility (μ) for thin GaN channel 2DEGs with AlN barriers (10 nm thick) and $Al_{0.5}Ga_{0.5}N$ (5 nm thick) back-barriers grown on AlN template on sapphire.

roughness scattering, which is much stronger due to the fact that the 2DEG is probing the two interfaces. In a next step, the impact of the modulation doping on the electron mobility was studied. For this purpose, a sample was grown with a 5 nm thick GaN channel and a 2nm thick AlN spacer in an attempt to prevent impurity scattering of the 2DEG with Si-doping present in the $Al_{0.5}Ga_{0.5}N$ back-barrier. The electron mobility only slightly improved by using the AlN spacer, suggesting negligible scattering due to the presence of impurities in the vicinity of the 2DEG. Finally, a sample was grown to ensure that the carriers are in fact supplied to the 2DEG by the modulation-doping. As expected, the carrier density reduces by more than a factor of 3 in the absence of modulation-doping. The impact of interface roughness scattering in combination with high electric fields present in square and triangular QWs was theoretically investigated by Jana and Jena [130]. For high electric fields, interface roughness scattering is dramatically enforced (Stark-effect scattering), which leads to the degradation of the electron mobility as the square of the peak electric field. Figure 5.18 illustrates rectangular and triangular QWs without (a) and with (b-c) an electric field. Furthermore, interface roughness scattering and the corresponding length scales L and $\Delta(r)$ are shown. In the previous section, modulation-doped heterostructures were discussed with AlGaN back-barriers with an Al content of 50 %. In order to reduce the internal electric field and hence the Stark effect scattering, a series of samples were grown with an AlGaN back-barrier Al content of 10, 20 and 30 %. The resulting electronic properties for these structures are given in Tab. 5.3 and compared to the 50 % structure discussed before. Interestingly, the electronic properties show no clear trend as a function of Al content. For 20 % Al content, the structure exhibits the lowest sheet resistance thanks to both high carrier density (3.3×10^{13} cm^{-2}) and

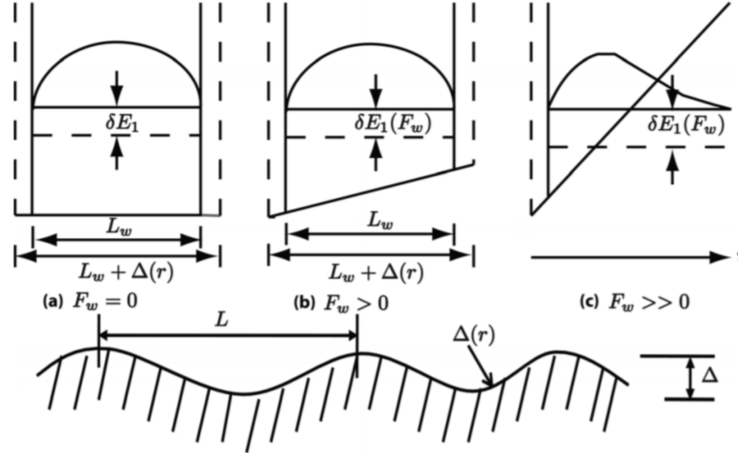

Figure 5.18 – Illustration of interface roughness scattering as a function of electric field for square and triangular QWs. (a) Square QW without electric field and (b) square QW with electric field. In (c) a triangular QW with high electric field is illustrated. In (d) interface roughness scattering and the corresponding length scales L and $\Delta(r)$ are shown. Reproduced and modified from [130] with permission from AIP.

Al content x	R_s (Ω/sq)	n_s (10^{13} cm^{-2})	μ (cm^2 V^{-1} s^{-1})
0.1	952	2.5	262
0.2	375	3.3	504
0.3	681	3.4	267
0.5	433	3.2	457

Table 5.3 – Room-temperature Hall effect measurements: Sheet resistance (R_s), carrier density (n_s) and electron mobility (μ) for thin GaN channel 2DEGs with AlN barriers (10 nm thick) and $Al_xGa_{1-x}N$ (5 nm thick) back-barriers grown on AlN template on sapphire.

high electron mobility 504 cm^2 V^{-1} s^{-1}. There are several reasons that could explain the lack of improvement as the Al content is lowered to 10 %. The high temperature (850 °C) used for the growth of the AlGaN back-barriers resulted in a 3D RHEED pattern for the 10 % Al structure. Therefore, the surface roughening could potentially be responsible for the degradation of the electron mobility. Further systematic studies are needed to conclusively understand the significance of Stark-effect scattering in AlN/GaN/AlN heterostructures.

In this final section, the modulation-doping of AlN/GaN/AlGaN heterostructures are used to investigate the low electron mobility of AlN/GaN/AlN structures. The polarization-mismatch of the thin GaN channel to the AlN barrier and buffer leads to both a 2DEG and a two-dimensional hole gas (2DHG) at the top and bottom interface, respectively, illustrated in Fig. 5.19. The much higher effective hole mass in GaN compared to electrons leads to a hole mobility, which is at least one order of magnitude lower. Since the carrier density of both gases has the same order of magnitude ($\sim 10^{13}$ cm^{-2}) the resulting conductivity for the 2DHG should also be one order of magnitude lower than in GaN. Therefore, it is suggested

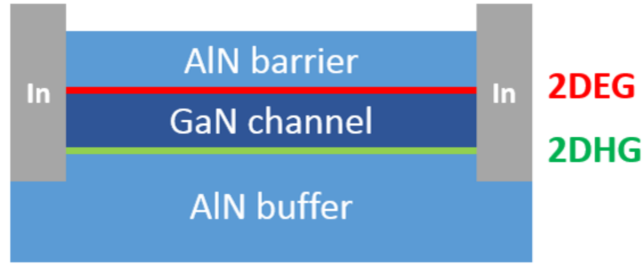

Figure 5.19 – Illustration of AlN/GaN/AlN heterostructure with parallel conduction paths formed by a 2DEG and 2DHG at the top and bottom interface, respectively.

Al content x	R_s (Ω/sq)	n_s (10^{13} cm^{-2})	μ (cm^2 V^{-1} s^{-1})
0.5	433	3.2	457
0.75	540	2.6	434
0.85	966	2.4	270
0.9	679	2.3	389

Table 5.4 – Room-temperature Hall effect measurements. Sheet resistance (R_s), carrier density (n_s) and electron mobility (μ) for thin GaN channel 2DEGs with AlN barriers (10 nm thick) and $Al_xGa_{1-x}N$ (5 nm thick) back-barriers grown on AlN template on sapphire.

that the measured electron mobility observed in AlN/GaN/AlN heterostructures is low due to parallel conduction through the 2DEG and the intrinsically lower mobility in the 2DHG.
In order to test this hypothesis, Schrödinger-Poisson calculations were performed to investigate the effect of introducing a high Al content (> 50 %) AlGaN back-barrier with modulation-doping to increase the band-offset and therefore deplete the 2DHG. The electron mobility of such structures should therefore not be affected by the presence of the 2DHG. In Fig. 5.20 the calculated band-diagrams are shown. Above an Al content of 90 % the valence band is lowered below the Fermi level (E_F) and the 2DHG is depleted. A series of samples were grown in order to investigate whether the low electron mobility can be explained by the presence of the 2DHG. The Al content of the AlGaN back-barrier was increased from 50 to 90 %. The resulting electronic properties are given in Tab. 5.4. The carrier density decreases from 3.2 to 2.3×10^{13} cm^{-2} with increasing Al content. This is expected since with increasing Al content and therefore band gap energy, doping becomes more challenging. On the other hand, the electron mobility remains almost constant for all structures. On the other hand, the electron mobility shows no clear trend as a function of Al content. Particularly, at 90 % Al the electron mobility does not increase even though the 2DHG is fully depleted. Hence, the low electron mobility is not likely to be due to the presence of the 2DHG.

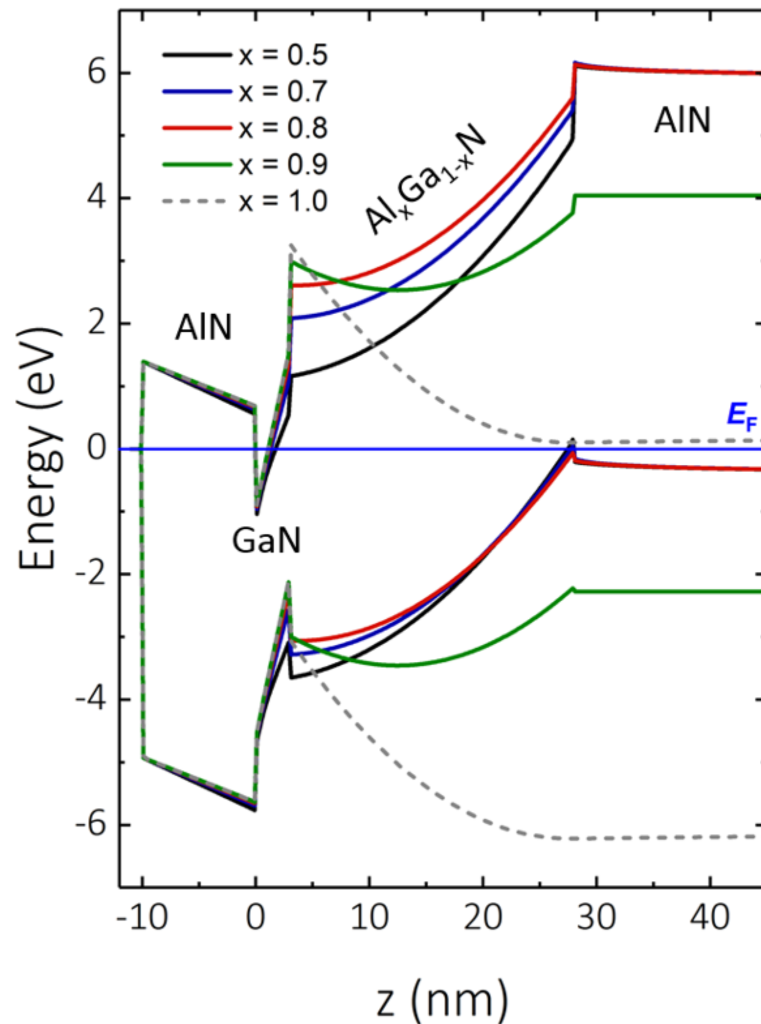

Figure 5.20 – Calculated energy band diagram of AlN/GaN/AlN heterostructures along the growth direction with modulation-doping of AlGaN barriers with Al content ranging from 0.5 to 1.

5.7 Summary

In this chapter, the low electron mobility of AlN/GaN/AlN heterostructures was investigated. The electron mobility of thin GaN channel 2DEGs grown on AlN strongly depends on the channel thickness. Furthermore, the limiting scattering mechanism is independent of barrier type and is observed both for NH_3-MBE and MOVPE growth. The electronic properties of GaN channel 2DEGs grown on AlN template on sapphire and AlN single crystal with an initial dislocation density of 10^3 and 10^{10} cm^{-2} were investigated. For carrier densities above 1×10^{13} cm^{-2}, the electron mobility is not limited by dislocation scattering up to a density of 10^{10} cm^{-2}. However, the large lattice-mismatch between GaN and AlN (2.4 %) is suggested to introduce a very high initial dislocation density (> 10^{11} cm^{-2}) by plastic strain relaxation

above the critical thickness. The impact of dislocation scattering was investigated by preparing a series of samples with increasing carrier density. The screening of dislocations by the carriers leads to an increase in electron mobility. By applying the experimental results to a scattering model, a dislocation density of 5×10^{11} cm^{-2} was extracted, which is in good agreement with the reported in literature. Furthermore, modulation-doping of AlN/GaN/AlN heterostructures on thin GaN channels (below critical thickness) were investigated by using highly Si-doped AlGaN back-barriers, enabling ultra-thin GaN channels (3-5 nm thick) with electron mobilities above 500 cm^2 V^{-1} s^{-1}.

6 InGaN-based channels

In this chapter, 2DEGs based on InGaN channels are studied. In particular, the impact of alloy disorder on the electronic properties of InGaN channels is investigated as a function of indium content. In a first step, the motivation for this study is presented. Then, results based on PL and Hall effect measurements are given, and a simple theoretical model is used to describe the alloy disorder scattering. Finally, the origin for the large discrepancy in literature observed for the electron mobilities in InGaN channels is discussed.
The material used in this chapter was published [131] and reproduced with permission of AIP Publishing.

6.1 Background

Two-dimensional electron gases (2DEGs) based on InGaN channels are interesting for two main reasons: (i) the physics of disordered systems can be studied by transport measurements; (ii) the application of InGaN channels for high power electronics. In the following sections, both topics will be discussed in more detail.

6.1.1 InGaN alloy disorder

The success of light-emitting diodes based on InGaN quantum wells is in part due to the localization of carriers imposed by the alloy disorder [1]. The lack of native substrates for the growth of III-nitrides implies a large amount of defects, which should lead to strong non-radiative recombination, dramatically reducing the efficiency of optoelectronic devices. However, since the carriers are strongly localized by alloy disorder, radiative recombination occurs before the carriers can reach a defect. Hence, it is of paramount importance to understand the mechanism of carrier localization in more depth. Over the past decade a large amount of studies have been performed, mainly through theoretical calculations and optical measurements of the InGaN alloy, as a function of indium content. In Fig. 6.1(a) one of the main results from localization landscape theory [132] is presented. The standard deviation

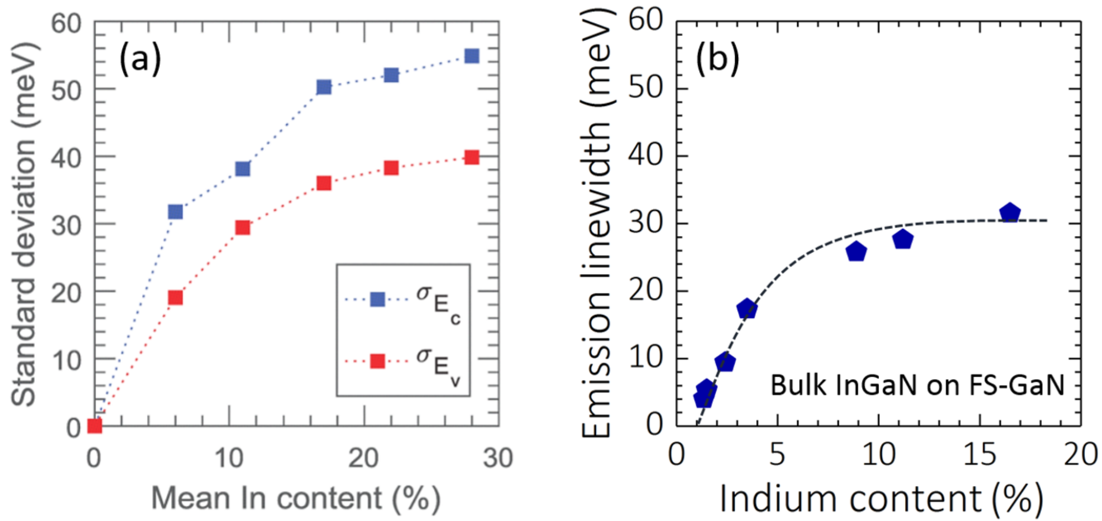

Figure 6.1 – (a) Theoretical results obtained by localization landscape theory. Standard deviation of conduction band (blue squares) and valence band (red squares) fluctuations induced by alloy disorder as a function of In content. Reproduced and modified from [132] with permission from APS. (b) Optical emission linewidth of InGaN layers grown on free-standing GaN substrates measured at 10 K as a function of In content. The experimental results were taken from [133, 134].

represents the energy fluctuations brought about by the InGaN alloy disorder as a function of In content for both electrons (blue) in the conduction band and holes (red) in the valence band. Two distinct features can be observed in the evolution of the energy fluctuations: (i) for an In content of 6 % the alloy disorder is already significant, and (ii) for even higher In content, the fluctuations gradually increase and saturate (> 15 %). Furthermore, alloy disorder seems to affect both electrons and holes. In Fig. 6.1(b), results obtained by optical measurements on InGaN layers grown on free-standing GaN substrates are shown [133, 134]. As expected, the emission linewidth broadens as a function of In content. Assuming that the emission linewidth reflects the alloy disorder, the optical measurements are in good agreement with localization landscape theory (Fig. 6.1(a)). It is worth mentioning that absorption-based optical measurements would be more conclusive, since, in that case, band-to-band states are probed. On the other hand, emission only accesses the low energy states. For an unambiguous understanding of the impact of In content on alloy disorder, probing by single particles (electrons or holes) would be more desirable, rather than measurements involving electron-hole pairs.

The results obtained in the following chapter are based on transport measurements of the electron density and mobility. They provide a complementary look at alloy disorder in InGaN and its evolution as a function of In content.

6.1.2 Power electronics with InGaN channels

The high electron saturation velocity and large piezoelectric polarization-mismatch of InN compared to GaN suggest tremendous potential for In-rich InGaN alloys as channel material, enabling very high power and high frequency electronic applications. Furthermore, the much smaller electron effective mass of InN (0.05 m_0) compared to GaN (0.2 m_0) implies higher electron mobilities than in GaN. However, compared to other III-V semiconductors, III-nitrides exhibit an alloy scattering term which is much stronger (e.g. 30 times higher in InGaN than InGaAs), which is mainly due to their much larger conduction-band offsets and their larger electron effective masses. Therefore, there are two counteracting properties which need to be compared when speaking of the electron mobility. On the one hand, the electron effective mass decreases with increasing In content, leading to high electron mobilities. On the other hand, as discussed in the previous section, the alloy disorder and, with it, alloy scattering, also increases with increasing In content. Hence, it is of interest, to investigate the impact of alloy disorder on the electron mobility of InGaN as a function of In content.

Over the past decade, several groups have reported on the electronic properties of InGaN by measuring the electron mobility of 2DEGs residing in InGaN channels [135–151]. The reported electron mobilities are much higher than for bulk InGaN layers of the same In concentration, which is surprising. The electron mobility in bulk layers is generally higher than in 2DEGs due to the absence of interface roughness scattering in the former case. For example, a mobility of 1240 $cm^2\ V^{-1}\ s^{-1}$ was reported for an $In_{0.1}Ga_{0.9}N$ channel [151], compared to 227 $cm^2\ V^{-1}\ s^{-1}$ for a bulk sample of the same composition [138]. Furthermore, the electron mobilities reported in literature are highly dispersed, ranging from 227 to 1240 $cm^2\ V^{-1}\ s^{-1}$ for 10 % In. This is possibly related to the challenges of growing high quality In-rich InGaN channels. The high vapor pressure of InN and the large lattice-mismatch to GaN constrain the possible growth temperature and channel thicknesses, leading to strain relaxation, introduction of dislocations and surface roughening. In the previous section, we discussed how In-rich InGaN layers are strongly affected by alloy disorder for an In content above 2 %. Therefore, it is surprising to see reports with electron mobilities as high as 1240 $cm^2\ V^{-1}\ s^{-1}$ for an In composition of 10 %.

In the following chapter, the electronic properties of InGaN 2DEG channels are investigated by growing a series of samples as a function of In content. Furthermore, the measured electron mobilities are compared to a theoretical model describing alloy scattering. Finally, a possible origin for the high electron mobilities observed in literature for In-rich InGaN channels is discussed.

6.2 Electron mobility of InGaN channels

As a first step, a series of samples were prepared consisting of InGaN channels with an indium content ranging from 0 to 20 %. The heterostructure growth was performed by MOVPE in a horizontal reactor on *c*-plane sapphire substrates. The absence of a showerhead eliminates

a potential source of Ga contamination which could potentially lead to the unintentional growth of GaN interlayers between the InGaN channel and the InAlN barrier when switching growth conditions. For all samples, the InGaN channels were grown on 2 μm thick GaN buffers. The channel thickness was 5 nm in order to remain pseudomorphic on GaN and to avoid strain relaxation and interface roughening . The layers following the InGaN channel consisted of a 1 nm AlN spacer, 10 nm lattice-matched $In_{0.18}Al_{0.82}N$ barrier and a 2 nm GaN cap, as shown in Fig. 6.2.a. The layer thicknesses and alloy compositions were determined by

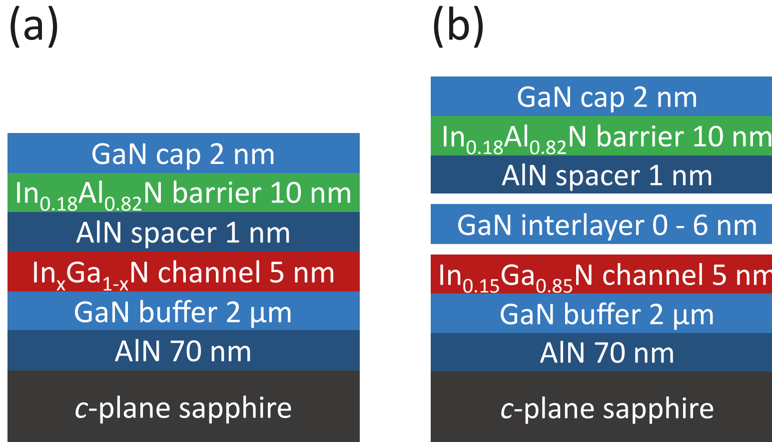

Figure 6.2 – Schematic illustration of heterostructures used for the study of (a) InGaN channel mobility and (b) the impact of thin GaN interlayers.

HR-XRD. In Fig. 6.3, the low temperature PL spectra give qualitative information about the alloy disorder of InGaN channels as a function of In content. The emission energy clearly shifts from 3.49 eV, for a GaN channel to 1.98 eV for $In_{0.2}Ga_{0.8}N$. This redshift is due to the large built-in electric field in the thin (5 nm thick) InGaN channel, giving rise to a strong quantum confined Stark effect. Furthermore, we observe an increase in the FWHM of the PL peak from about 20 to 340 meV for GaN and $In_{0.2}Ga_{0.8}N$, respectively. There are two distinct origins for the observed broadening, (i) an increase in InGaN alloy disorder and (ii) an increase in the built-in electric field combined with the InGaN channel thickness fluctuations. The additional features on the spectra are due to Fabry-Perot interference effects. In the inset of Fig. 6.3, the emission energy and the FWHM are given as a function of the In content. Interestingly, the FWHM strongly increases for an In content above 5 %. Hence, a dramatic decrease in electron mobility can be expected even for such a low In content. The transport properties of the InGaN channels were determined as a function of In content by room-temperature Hall effect measurements as presented in Fig. 6.4. While the electron density remains approximately constant as a function of In content with an average value of $\sim 2.47 \times 10^{13}$ cm^{-2}, the electron mobility strongly decreases from 1340 to 173 cm^2 V^{-1} s^{-1} when the In content is increased from 0 to 20 %. Specifically, we observe a strong decrease even for an In content as low as 2 %, which is in line with the previously discussed broadening of the PL emission with increasing In content. Theoretical calculations based on the localization landscape theory reported by Piccardo *et al.* [132] show that 6 % In can lead to significant fluctuations in

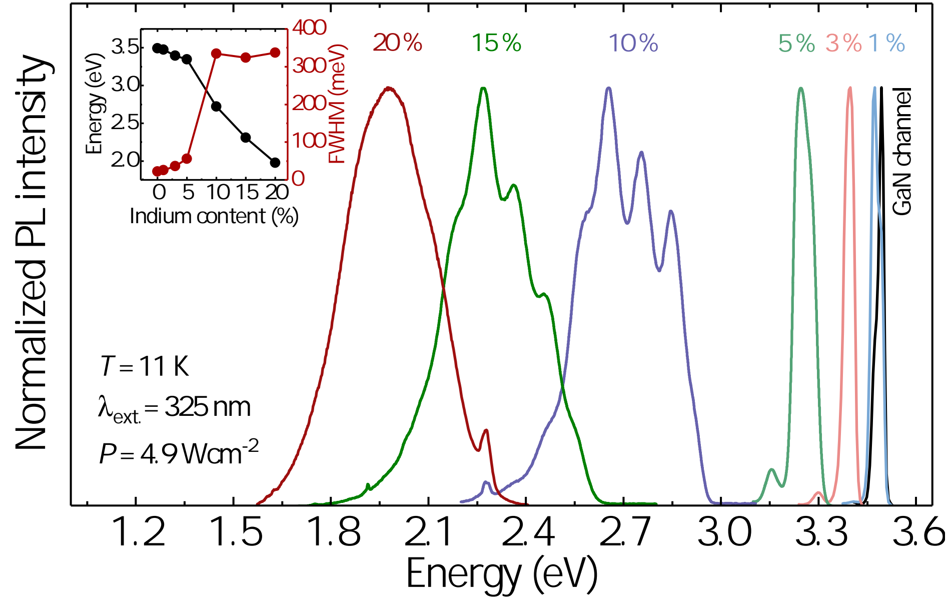

Figure 6.3 – Low temperature photoluminescence spectra of InGaN channels as a function of indium content. (Inset) Emission energy and FWHM. Reproduced and modified from [131] with permission from AIP.

the conduction band profile and hence trigger strong scattering of electrons and a decrease in mobility. Furthermore, investigations on the absorption edge broadening of bulk InGaN layers have shown a significant increase in alloy disorder for an In content above 2 % [133]. Interestingly, the electron mobility staggers at high In content ($x \geq 0.15$), which is consistent with the saturation of alloy disorder potential fluctuations shown in Fig. 6.1. In a next step, the decrease in electron mobility with increasing In content is investigated quantitatively by applying a theoretical model, which was developed by Bastard [152] to describe alloy disorder scattering at semiconductor interfaces. In order to model the total electron mobility of our structures, the individual contributions need to be separated into two components, (i) indium-independent scattering mechanisms such as phonons, interface roughness, charged impurities, dislocations and (ii) indium-dependent alloy disorder scattering. Since the lowest In content InGaN channel is 0 %, i.e. a conventional GaN channel, we can assume all scattering mechanisms that are not indium-dependent to be absorbed into the first term (μ_0). Furthermore, we assume that all investigated channels have these scattering mechanisms in common. One could argue that interface roughness could be the limiting scattering factor, since for increasing In content the surface morphology potentially deteriorates. However, we will provide an experimental argument in the next section to explain why interface roughness can be discarded as the mobility limiting scattering mechanism. The second term describing the alloy disorder scattering is expressed by [152]

$$\frac{1}{\mu_{\text{Alloy}}} = \frac{m^2 \Omega \delta V^2 x(1-x) \kappa P^2}{2e\hbar^3}, \tag{6.1}$$

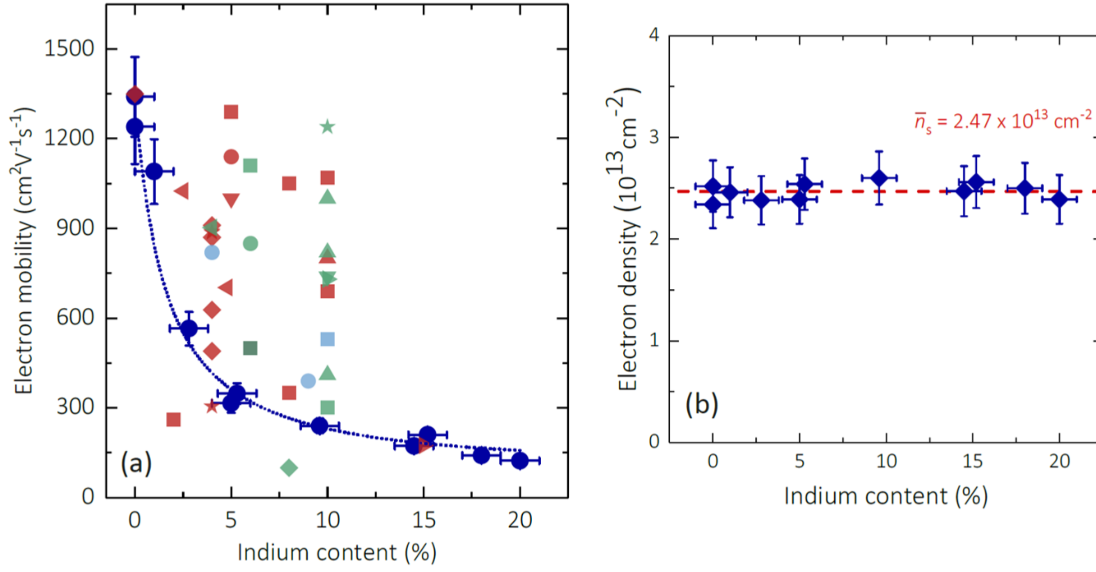

Figure 6.4 – (a) Room temperature electron mobility of InGaN channels as a function of In content (dark blue circles). The dotted blue curve corresponds to the theoretical mobility with alloy disorder as the main scattering mechanism. Light red, blue and green data-points represent values taken from literature [135–151]. (b) Electron density of InGaN channels as a function of In content (blue diamonds). The red dashed line corresponds to the average value. Reproduced and modified from [131] with permission from AIP.

where m is the linearly interpolated electron effective mass of InGaN, Ω is the wurtzite unit cell volume ($\sqrt{3}/2a^2c$) with a and c the linearly interpolated lattice constants, x is the In content, κ is the extent of the electron wave function, P is the fraction of electrons penetrating the alloy barrier region and δV is the alloy fluctuation potential, which is assumed to be close to the conduction-band offset between GaN and InN (2.4 eV) [20, 152]. In the particular case where the 2DEG resides in an alloy channel, we modify the expression by assuming that the full wave function is within the alloy ($P = 1$) and we estimate the extent of the wave function κ by the FWHM of the electron density determined by Schrödinger-Poisson calculations shown in Fig. 6.5. The FWHM of the electron wave function decreases as a function of increasing In content from 1.6 to 1.2 nm. The wave vector κ is estimated as the inverse of the 2DEG FWHM (κ=1/FWHM). As previously discussed, we assume that all other scattering mechanisms are independent of the In content and give rise to the mobility of a pure GaN channel (μ_0). Hence, by using Matthiessen's rule, the total mobility (μ) of an InGaN channel can be described by μ_0 and μ_{Alloy} given by Eq. 6.1 as,

$$\frac{1}{\mu} = \frac{1}{\mu_{\text{Alloy}}} + \frac{1}{\mu_0}. \tag{6.2}$$

The total mobility is calculated by applying Eq. 6.2 and using the material values given in Tab. 6.1 as a function of In content. The result is shown in Fig. 6.4 as a blue dotted line. The theoretical model fits remarkably well with our experimental values. The mobility drops

	GaN	InN
m (m_0)	0.2	0.05
a (Å)	3.189	3.545
c (Å)	5.185	5.703
δV (eV)	2.4	
b (eV)	1.4	

Table 6.1 – Room-temperature material parameters of GaN and InN used for the alloy scattering model, where m is the electron effective mass in units of the free electron mass, a and c are the *in-plane* and perpendicular lattice constants, δV is the conduction-band offset and b is the bowing parameter between GaN and InN. Taken from [7].

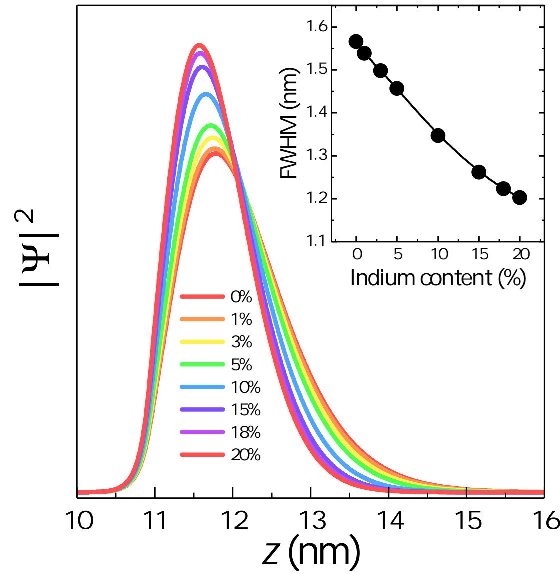

Figure 6.5 – InGaN channel 2DEG wave function probability density in the growth direction for In contents ranging from 0 to 20 %. The inset shows the FWHM of the distribution as a function of In content. Reproduced and modified from [131] with permission from AIP.

rapidly as a function of In content, which is mainly due to the large value of the conduction-band offset (2.4 eV) between GaN and InN. At this point we should mention that a similar expression can be derived for alloy scattering in quantum well structures as [153],

$$\frac{1}{\mu_{\mathrm{Alloy}}^{\mathrm{QW}}} = \frac{m^2 \Omega \delta V^2 x(1-x)}{2e\hbar^3} \frac{27\pi^2}{64L}, \tag{6.3}$$

where L is the quantum well width. Comparing the two mobility expressions, Eqs. 6.1 and 6.3, we observe that for a well width L of 5 nm corresponding to the thickness of the InGaN channel, the wave vector κ corresponds to a FWHM of 1.2 nm. This value is in good agreement with our theoretical estimation shown in Fig. 6.5. Hence, both expressions can be used for the calculation of the alloy scattering term. Furthermore, it demonstrates the importance

of the conduction-band offset (δV) common to both expressions.
In Fig 6.4, experimentally determined electron mobilities for InGaN channels reported in literature are also shown. The InGaN channels are based on a variety of different barriers (AlGaN [135–142], InAlN [143–147], InAlGaN [148–151])) and channel thicknesses. Many of the values are much higher than what is expected theoretically based on our alloy disorder scattering model. The large data scattering is a strong argument in favor of an extrinsic origin for the high mobilities reported for InGaN channels. Therefore, the following growth related issues are suggested as possible origins for the observed high electron mobilities:

- The growth temperature for the barriers was increased (> 1000 °C) after the deposition of the InGaN channel in several reports. The high vapor pressure of InN could therefore induce desorption of In during the temperature ramp leading to a thin GaN interlayer. Hence, the subsequent barriers were grown on GaN leading to conventional HEMT structures with high electron mobilities. In many cases, the In content of the channels was not experimentally determined, neither by HR-XRD nor PL, which makes the interpretation of the results difficult.

- The presence of residual Ga atoms in the growth chamber, particularly in the shower head of vertical MOVPE reactors is known to result in parasitic growth of GaN (see Fig. 6.6). The presence of an unintentional GaN interlayer [154–158] between the InGaN channel and the barrier could potentially lead to a redistribution of the InGaN channel 2DEG. For a sufficient interlayer thickness, the 2DEG mainly resides in the GaN interlayer and only partially in the InGaN channel. Hence, the electron mobility will be less affected by the alloy disorder of the InGaN channel.

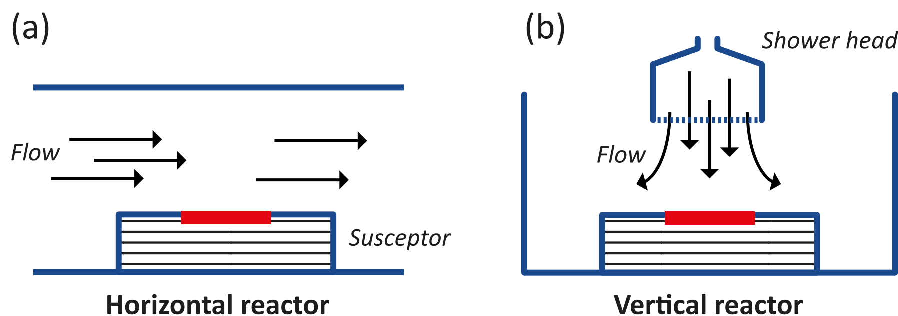

Figure 6.6 – Schematic illustration of (a) horizontal and (b) vertical MOVPE reactors.

In both cases, the measured electron mobility is higher than what is expected from alloy disorder scattering theory described in the previous section due to an unintentional GaN interlayer.
In the following section, the impact of GaN interlayers is investigated both theoretically and experimentally by performing Schrödinger-Poisson calculations and intentionally growing GaN interlayers between the $In_{0.15}Ga_{0.85}N$ channel and InAlN barrier.

6.3 Impact of GaN interlayers

As a first step, a series of samples were grown with GaN interlayers of increasing thickness (0 to 6 nm) intentionally inserted between the $In_{0.15}Ga_{0.85}N$ channel and InAlN barrier (see Fig. 6.2(b)). The GaN interlayers were grown under the growth conditions of the InGaN channels (low temperature) in order to avoid In desorption. The room-temperature electronic properties of the samples as a function of GaN interlayer thickness are shown in Fig. 6.7 as blue circles. The electron mobility clearly increases with GaN interlayer thickness, while the electron density remains approximately constant ($\sim 2.36\times10^{13}$ cm^{-2}). Interestingly, only a few nm ($\sim$ 5 nm) of GaN are necessary to reach the electron mobility of a pure GaN channel shown as a green dashed line in Fig. 6.7(a). Furthermore, the increase in electron mobility with only a few nm of GaN interlayer demonstrates that alloy scattering is indeed the dominating scattering mechanism. If interface roughness was the limiting scattering mechanism, the insertion of a thin GaN interlayer (~ 5 nm) grown at low temperature would not be sufficient to improve the surface morphology and therefore the electron mobility would not improve, contrary to what we observe. In a next step, Schrödinger-Poisson calculations were performed in order

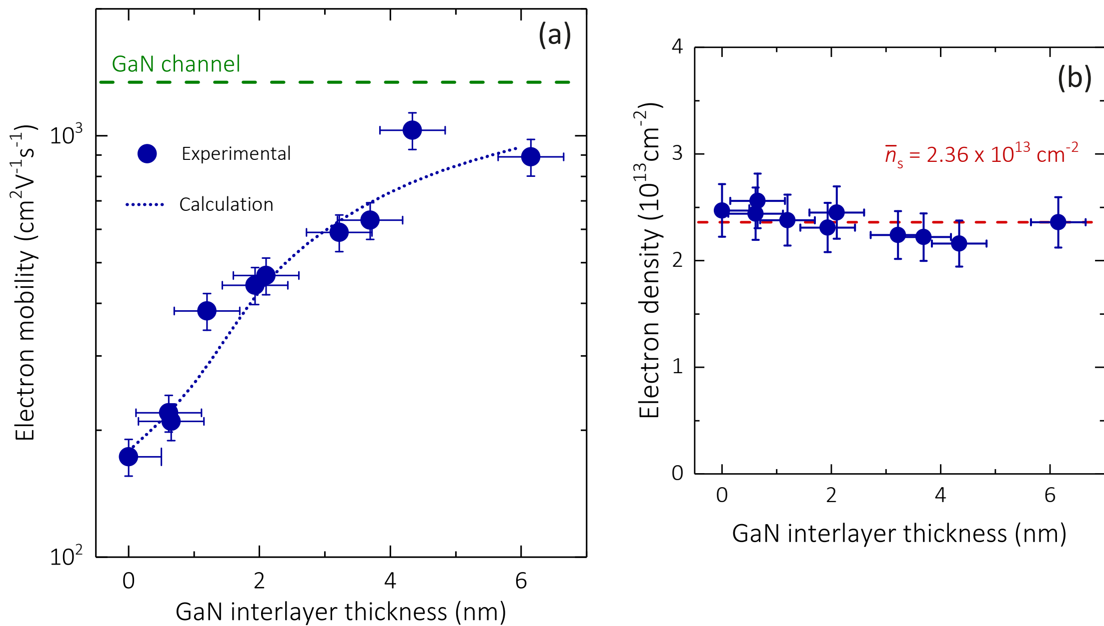

Figure 6.7 – Room temperature (a) electron mobility of InGaN channels as a function of GaN interlayer thickness (blue circles). The blue dotted line corresponds to theoretical calculations. The green dashed line shows the mobility of a GaN channel. (b) Electron density of InGaN channels as a function of GaN interlayer thickness. Red dashed line corresponds to the average value. Reproduced and modified from [131] with permission from AIP.

to investigate the impact of GaN interlayer thickness on the distribution of the 2DEG and on the electron mobility. In Fig. 6.8, the electron density and conduction band profile of InGaN channels (see structure in Fig. 6.2(b)) are given for GaN interlayer thicknesses ranging from 0 to 6 nm. In the absence of a GaN interlayer (black curve in Fig. 6.8(a)), the 2DEG resides

fully within the InGaN channel. With increasing interlayer thickness, the electron density redistributes between the InGaN channel and the GaN interlayer. Hence, above an interlayer thickness of 3 nm the electron density lies primarily within the GaN interlayer and only partially in the InGaN channel. Since the electron mobility in GaN is much higher than in the $In_{0.15}Ga_{0.85}N$ channel (1340 and 173 $cm^2\ V^{-1}\ s^{-1}$, respectively), we expect a strong impact on the measured electron mobility.

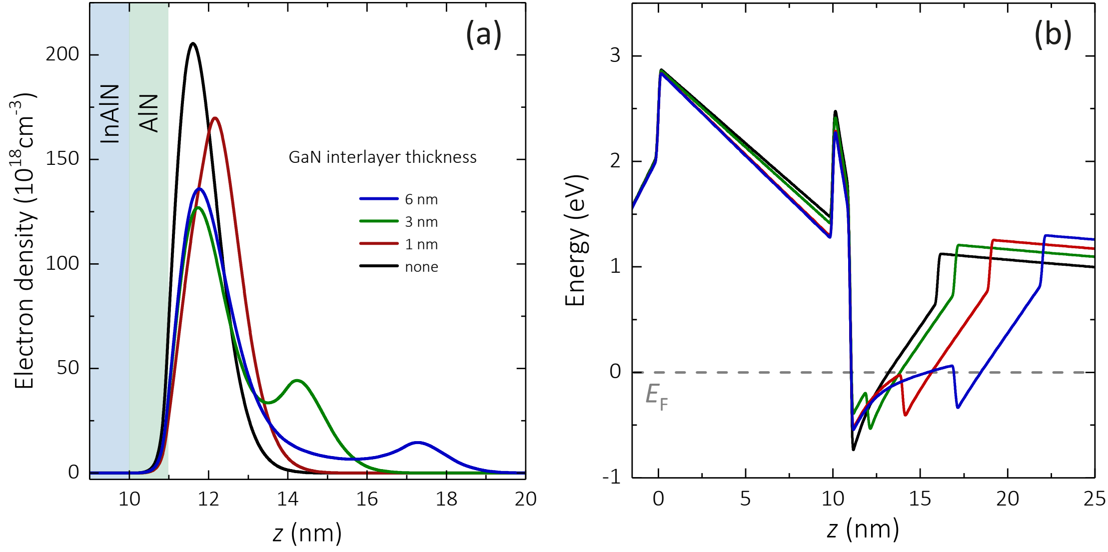

Figure 6.8 – (a) Electron density distribution of InGaN channels as a function of GaN interlayer thickness. (b) Conduction band profile as a function of GaN interlayer thickness. Reproduced and modified from [131] with permission from AIP.

The distribution of the 2DEG in the GaN interlayer and the InGaN channel was determined by integrating over the spatial extent of the electron density illustrated in Fig. 6.9 for 3 nm GaN interlayer thickness. The weights of the electron densities for GaN and InGaN are given by p_{GaN} and p_{InGaN}, respectively, as

$$p_{\mathrm{GaN}} = \int_{\mathrm{GaN}} \rho(z)dz, \tag{6.4}$$

where $\rho(z)$ is the electron density in growth direction. The probability p_{InGaN} is determined by the normalization condition ($p_{\mathrm{GaN}} + p_{\mathrm{InGaN}} = 1$). Finally, the total electron mobility (μ) can be expressed by

$$\frac{1}{\mu} = \frac{p_{\mathrm{GaN}}}{\mu_{\mathrm{GaN}}} + \frac{p_{\mathrm{InGaN}}}{\mu_{\mathrm{InGaN}}}. \tag{6.5}$$

with the mobilities of GaN (1340 $cm^2\ V^{-1}\ s^{-1}$), InGaN (173 $cm^2\ V^{-1}\ s^{-1}$) and weights given by p_{GaN} and p_{InGaN}, respectively, as a function of GaN interlayer thickness. The calculated electron mobility as a function of the GaN interlayer thickness is shown in Fig. 6.7(a) as a blue dotted line. The calculated model is in excellent agreement with the experimental re-

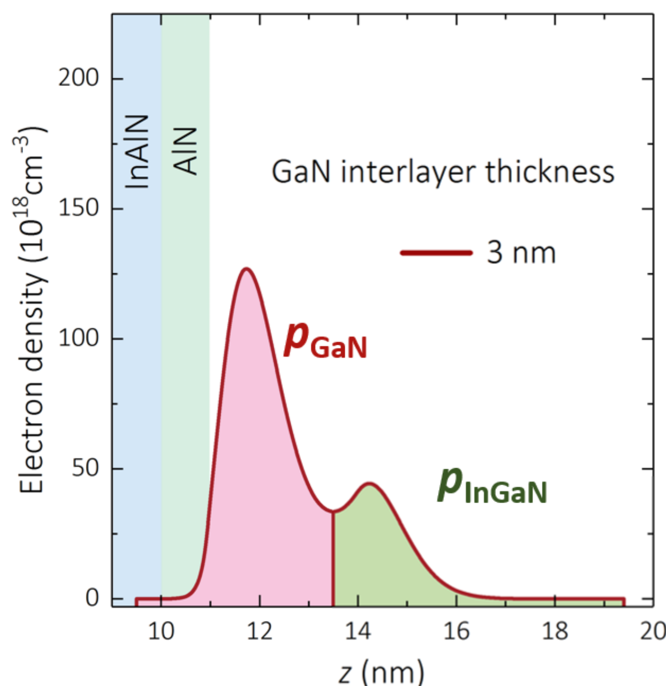

Figure 6.9 – Electron density distribution of an InGaN channel with a 3 nm GaN interlayer. The probabilities p_{GaN} and p_{InGaN} are determined by integration of the electron density over the red and green areas, respectively.

sults. Hence, the increase in electron mobility with increasing GaN interlayer thickness can be explained by the redistribution of the electron density from the InGaN channel to the GaN interlayer, avoiding strong alloy scattering.

6.4 Summary

In this chapter, the electronic properties of InGaN channels were determined as a function of In content. The electron mobility rapidly drops for an In content as low as 2 %, which is in line with linewidth broadening observed in optical measurements. The electron mobility is modeled by considering a modified alloy scattering term. Alloy disorder is identified as the dominating scattering mechanism limiting the electron mobility in In-rich InGaN channels. The high mobilities for InGaN channels reported in literature are explained by two main extrinsic phenomena occurring during growth. (i) Temperature ramps after the growth of InGaN above 1000 °C lead to the desorption of In, leaving behind a low-In content GaN surface. (ii) Unintentional growth of GaN is known to occur due to parasitic Ga atoms present in the growth chamber, in particular, in the showerhead of vertical MOVPE reactors. In both cases, the InGaN channel is covered by a thin GaN interlayer, which leads to a high electron mobility due to the redistribution of the 2DEG carrier density from the InGaN channel to the GaN interlayer.

7 Ohmic contacts grown by MOVPE

In this chapter, ohmic contacts and their application to electronic devices are discussed. In the first section, the importance of low contact resistance is described. In the following part, the state-of-the-art fabrication of ohmic contacts by alloyed metal stacks and MBE regrowth is summarized. Finally, the regrowth of ohmic contacts performed by MOVPE is presented.

7.1 Background

7.1.1 Ohmic contacts

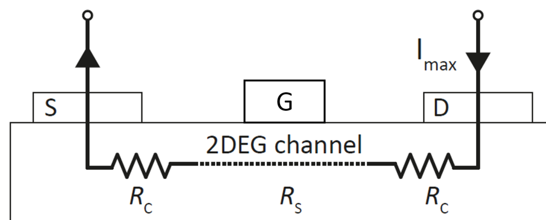

Figure 7.1 – Illustration of ohmic contacts. Source (S) and drain (D) electrodes are connected to the active area (2DEG channel) of a HEMT structure with a contact resistance R_C.

Ohmic contacts are conducting junctions between two conductors with a linear current-voltage relation (i.e. satisfying Ohm's law). A low resistance ohmic contact allows electrical charge to flow easily between the two conductors in both directions without rectification and significant power dissipation. For electronic devices such as HEMTs, ohmic contacts (source (S) and drain (D) in Fig. 7.1)) are fundamental building blocks used to connect the active region of the transistor (2DEG channel) to the external circuitry. For HEMTs operating at high power, a maximum current I_{max} flows between source and drain contacts when the transistor is in the On-state. Hence, the contact resistance between the channel and the ohmic contacts leads to a parasitic power dissipation by heat generation which needs to be removed from the active area in order to avoid self-heating effects. For HEMTs operating at high frequency, low contact resistances are also of importance. High frequency operation

can be characterized by the current gain cutoff frequency ($f_T = 1/(2\pi(\tau_t + \tau_p))$, where τ_t is the transient time for electrons in the active region and τ_p the parasitic delay time, which is proportional to the contact resistance. The second characteristic frequency is the maximum frequency $f_{max} \propto f_T$. Hence, it is of paramount interest to have low resistance ohmic contacts for both high power and high frequency electronics.
In the following section, the state-of-the-art fabrication methods for achieving low resistance ohmic contacts to III-nitride based HEMTs will be discussed in detail.

7.1.2 Alloyed ohmic contacts

The most commonly used fabrication method for the fabrication of ohmic contacts in III-nitride HEMTs is the deposition of a metal stack (Ti/Al) followed by an annealing step at high temperature (800 to 900 °C) under N_2 for up to 1 min. Typically the metal stack is capped by an additional Au layer (~ 100 nm) in order to prevent any oxidation. Furthermore, a refractory metal (Mo, Ni or Pt) is usually inserted between the Ti/Al and Au layer to avoid intermixing [159–162]. The contact resistances achievable by this method are usually about 0.3 Ω mm. The simple process flow for the fabrication of ohmic contacts by deposition of metal stacks makes this method convenient for rapid measurements. However, the harsh annealing step can give rise to a rough surface morphology of the contact, as well as reproducibility issues regarding the contact resistance.

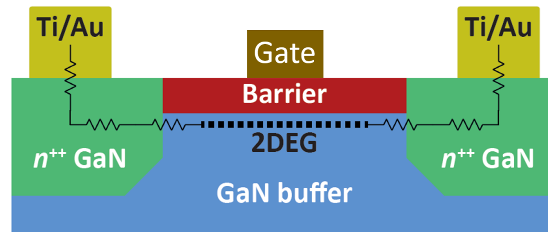

Figure 7.2 – Illustration of regrown ohmic contacts on HEMT structures.

7.1.3 Ohmic contacts by MBE

A more reliable method for the fabrication of ohmic contacts is the regrowth of highly Si-doped GaN (> 1×10^{20} cm^{-3}) by MBE [163–166]. Regrowth is performed selectively in pits which have been etched out around the active region of the HEMT as illustrated in Fig. 7.2. The growth temperature is kept below 700 °C in order to avoid deterioration of the 2DEG. Remarkably, the contact resistance achievable by regrowth can be as low as 0.1 Ω mm [163]. This comes at the price of the following processing steps:

- **Processing :** The regions of regrowth need to be removed by etching, while the remaining area is covered by SiO_2 in order to achieve selective regrowth.
- **Surface preparation :** The sample surface needs to be cleaned with a Piranha solution

(S_2SO_4:H_2O_2 3:1) for 15 minutes, followed by rinsing in deionized water. This step was identified as crucial in order to achieve a smooth surface morphology of the regrown GaN [164].

- **MBE calibration :** The Si-doping for the growth of n^{++} GaN needs to be calibrated prior to regrowth. A GaN template on sapphire is used as a test sample for the calibration growth. The Si-doping is determined by capacitance–voltage profiling and room-temperature Hall effect.
- **Sample preparation :** MBE regrowth is generally done on small sample pieces. Therefore, the sample pieces need to be glued on 2 inch Si wafers with indium.
- **Outgassing :** The samples need to be out-gassed for several hours at 600 °C prior to regrowth.

Even though MBE regrowth enables low contact resistances, the many necessary processing steps combined with the low availability of MBE systems, make this method not well appropriate for HEMT production.
A more industrially scalable technique for the fabrication of ohmic contacts on HEMTs would be regrowth by MOPVE, thanks to its wider availability and low cost of fabrication. In contrast to MBE, regrowth by MOVPE does not require repeated doping calibration, sample preparation and outgassing time. One of the main challenges of regrowth by MOVPE is the higher growth temperatures for GaN (> 1000 °C) compared to MBE (700 - 800 °C).
In the following section, the low temperature growth of n^{++} GaN by MOVPE and the optimization of processing steps (hardmask and surface preparation) are discussed. Finally, the low temperature n^{++} GaN is applied to HEMTs as regrown ohmic contacts.

7.2 Regrowth of ohmic contacts by MOVPE

7.2.1 Low temperature growth of n^{++} GaN by MOVPE

In this section, the conditions for low temperature growth of highly Si-doped GaN are discussed. GaN growth by MOVPE is typically performed at temperatures > 1000 °C. However, high temperature exposure of HEMT structures leads to strong deterioration. In particular, the electronic properties of the 2DEG are affected by high temperatures. Lowering the growth temperature usually leads to a reduced adatom mobility, poor surface morphology and introduction of defects, which can trap free carriers and therefore limit the free carrier concentration. Therefore, the challenge lies in lowering the growth temperature and optimizing the remaining growth conditions to achieve high free carrier densities. The optimization of the low temperature n^{++} GaN was performed by MOVPE on unintentionally doped 2 μm thick GaN templates on sapphire as illustrated in Fig. 7.3(a). The metal precursor and carrier gas were triethylgallium and N_2, respectively. The chamber pressure was maintained at 200 mbar for all growths. The Si-doping was performed by using silane (SiH_4), which was diluted to 100

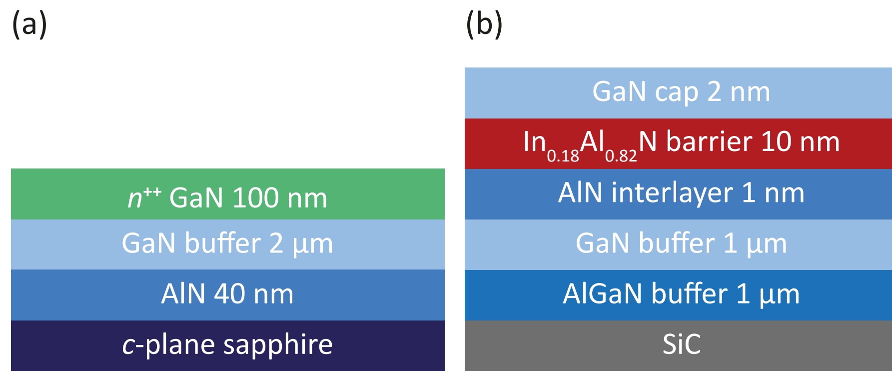

Figure 7.3 – Sample structures used for (a) the optimization of low temperature n^{++} GaN growth and (b) HEMT structure used for regrowth of ohmic contacts.

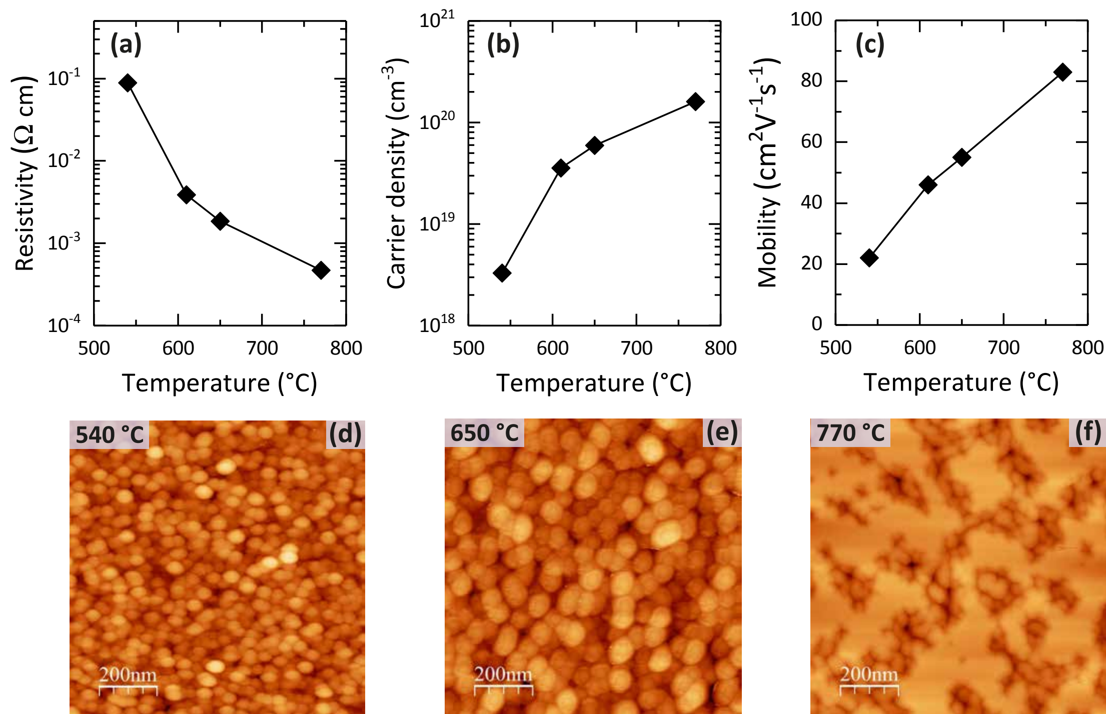

Figure 7.4 – Room temperature (a) resistivity, (b) carrier density and (c) mobility as a function of growth temperature of heavily Si-doped GaN layers at fixed SiH_4 flow rate of 6 sccm. 1×1 μm^2 AFM scans of samples grown at (d) 540 °C (e) 650 °C, and (f) 770 °C. The RMS surface roughness is 5, 11 and 6 nm, respectively. Reproduced and modified from [167] with permission from IOP.

ppm in H_2. The electronic properties and surface morphology were determined by room-temperature Hall effect and AFM, respectively. In a first step, a series of samples were grown in a temperature range from 540 to 780 °C with a fixed SiH_4 flow of 6 sccm. In Figs. 7.4 (a-c), the electronic properties and the corresponding surface morphology (d-f) are presented as a function of growth temperature. The carrier density decreases by two orders of magnitude

as the temperature is lowered. This is likely due to an enhanced incorporation of carbon, which compensates the carriers provided by the Si-doping [168]. The electron mobility also deteriorates by a factor 4 with decreasing temperature. The AFM scans in Figs. 7.4 (d-f) show granular-like features in the surface morphology for temperatures below 700 °C due to low surface kinetics. The grain sizes increase with temperature and start to coalescence at 770 °C into a continuous two-dimensional surface, leading to an increased electron mobility. Thus, it is possible to grow highly Si-doped GaN layers with a carrier density > 2×10^{20} cm^{-3} for a growth temperature as low as 770 °C. In a next step, a series of samples were grown at 740 °C as a function of SiH_4 flow in order to further optimize the growth. The electronic properties and AFM scans are shown in Fig. 7.5. The carrier density reaches values above 1×10^{20}

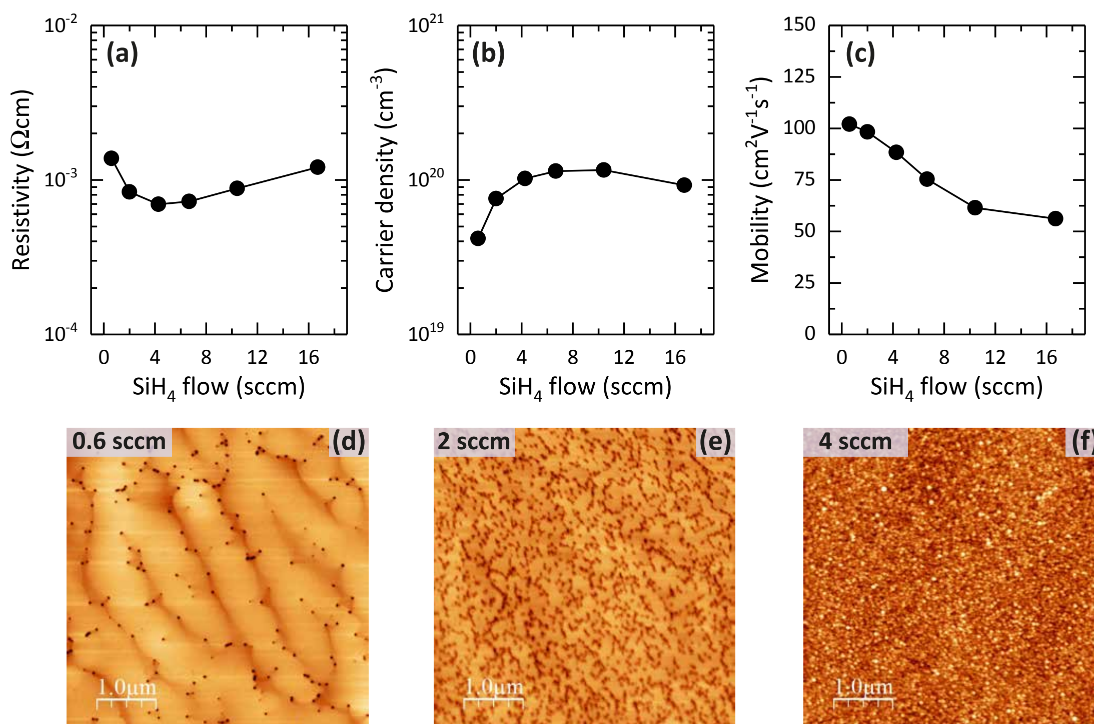

Figure 7.5 – Room temperature (a) resistivity (b) carrier density and (c) mobility as a function of SiH_4 flow rate of heavily Si-doped GaN layers at a fixed growth temperature of 740 °C. 5×5 μm^2 AFM scans of samples grown with (d) 0.6 sccm (e) 2 sccm, and (f) 4 sccm of SiH_4. The RMS surface roughness is equal to 2.7, 5.5 and 7.5 nm, respectively. Reproduced and modified from [167] with permission from IOP.

cm^{-3} for a SiH_4 flow exceeding 4 sccm. The electron mobility on the other hand decreases by a factor 2 as the SiH_4 is increased from 0 to 16 sccm. This degradation can be ascribed to: (i) increased Si incorporation and therefore impurity scattering and (ii) increased pit density with SiH_4 flow as can be observed in the AFM scans shown in Figs. 7.5(d-f). Overall, this results in a minimum resistivity of 7×10^{-4} Ω cm for a SiH_4 flow between 2 and 8 sccm. The optimized n^{++} GaN was also used for the fabrication of tunnel junctions on blue LEDs which is discussed in Appendix A.

7.2.2 Fabrication of TLM structures

The optimized low temperature growth of n^{++} GaN was applied to ohmic contacts for InAlN-based HEMT structures grown by MOVPE on SiC, as illustrated in Fig. 7.3(b). The processing and measurements of the TLM structures were performed in the group of Prof. Bolognesi at ETHZ. Following the growth of InAlN/GaN heterostructures on SiC, a SiO_x hardmask was deposited by plasma-enhanced chemical vapor deposition (PECVD) at a table temperature of 120 °C using $SiH_4(N_2)$ 2.5 % and N_2O as precursors. TLM test structures were patterned using polymethylmethacrylat (PMMA) and LN_2 cooled inductively-coupled plasma (ICP) etching based on SF_6 and Cl_2 to achieve a GaN-recess of 35 nm. The ICP etching process is identical to the recipe reported by Lugani *et al.* [164]. The PMMA resist was removed by dimethylsulfoxide (DMSO), acetone and IPA. Following the regrowth by MOVPE, metal stacks of Ti/Pt/Au (10/30/90 nm) were deposited by e-beam evaporation on the regrown n^{++} GaN contacts. One of the issues arising after the regrowth step was the removal of the SiO_x hard mask. In

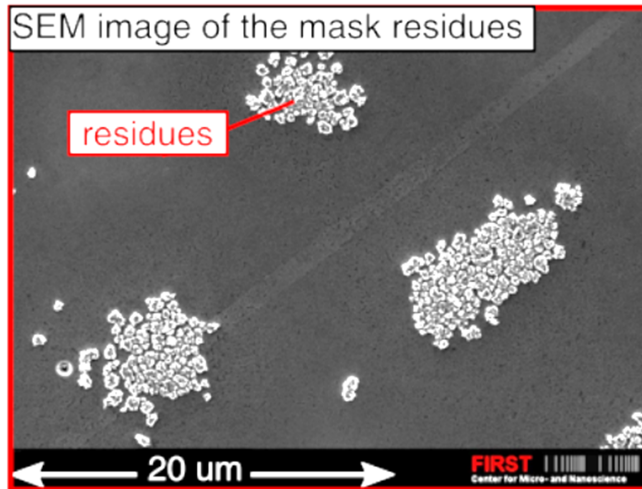

Figure 7.6 – SEM image showing the mask residues for a low-γ SiO_x mask.

the SEM image shown in Fig. 7.6, residues are clearly visible on the sample surface. High temperature exposure (~ 800 °C) of the SiO_x hardmask under NH_3 during regrowth leads to deterioration which is stronger for unoptimized stoichiometries. The PECVD recipe was optimized for regrowth by MBE, which occurs at much lower growth temperatures (700 °C). In the following section, the optimization of the SiO_x mask stoichiometry is discussed.

7.2.3 Optimization of SiO_x mask

The SiO_x hardmask stoichiometry is known to depend on the precursor flow ratio γ [169]

$$\gamma = \frac{\text{flow}\,(N_2O)}{\text{flow}\,(SiH_4)}. \tag{7.1}$$

In order to find the optimal SiO_x stoichiometry, a series of samples were prepared with flow ratios of 30, 84 and 110. Regrowth was performed on all samples at a fixed temperature of 825 °C. In Fig. 7.7, the SEM images show the results for the lowest and highest flow ratio. For a low flow ratio (γ = 30) the sample surface is contaminated with residues as mentioned in the previous section. In the case of high flow ratio (γ = 110), the hardmask could be easily removed with a HF (1:5) dip (150 s) and agitation in an ultrasonic bath (10 min).

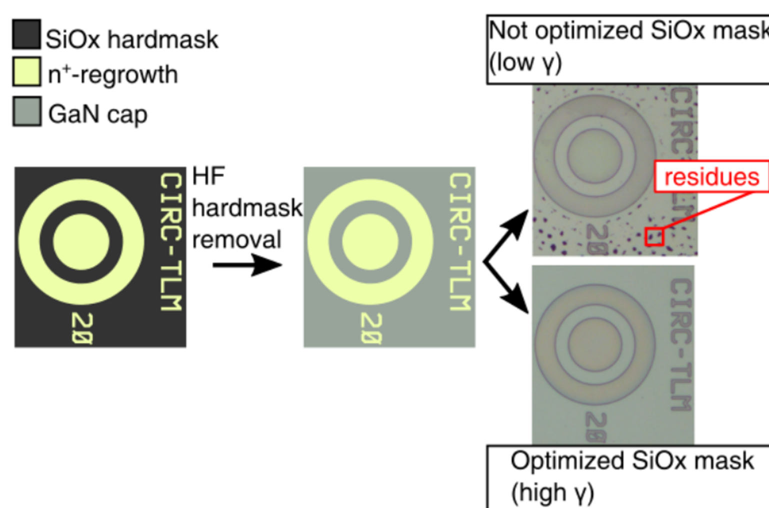

Figure 7.7 – SEM images of circular TLM structures showing the impact of high and low γ ratio. In the case of low-γ stoichiometry masks, residues remain on the surface of the sample. For high γ ratios, the mask can be completely removed with no observable residues.

7.2.4 Optimization of regrowth temperature

In Sec. 7.2.1, the growth of n^{++} GaN was optimized at low temperature (540 and 770 °C). This was mainly done in order to avoid a degradation of the 2DEG once the n^{++} GaN is used as regrown ohmic contacts. On the other hand, regrowth performed at too low temperatures reduces the carrier density of the n^{++} GaN due to compensation. In order to investigate the impact of temperature on the electronic properties of the regrown ohmic contacts, a series of samples were prepared. The regrowth temperature was varied between 675 and 825 °C, using a growth rate of 100 nm h^{-1}, high NH_3 flow and 20 sccm SiH_4. In Fig. 7.8 the resulting four-point probe TLM measurements are given. The total contact resistance (black points in Fig. 7.8(a) drastically reduces from 0.6 to 0.25 Ω mm as the growth temperature is increased from 675 to 825 °C. A similar trend is observed for the contact resistance between the n^{++} GaN and the metal stack (blue points). Furthermore, the sheet resistance of the n^{++} GaN (purple points in Fig. 7.8(b)) reduces from 200 to 50 Ω/sq as the temperature is increased to 825 °C, which is in line with the results obtained in the previous section. Interestingly, the 2DEG sheet resistance (green points in Fig. 7.8(b)) is not affected by the regrowth temperature. Hall effect measurements show that the carrier density and electron mobility prior/after regrowth

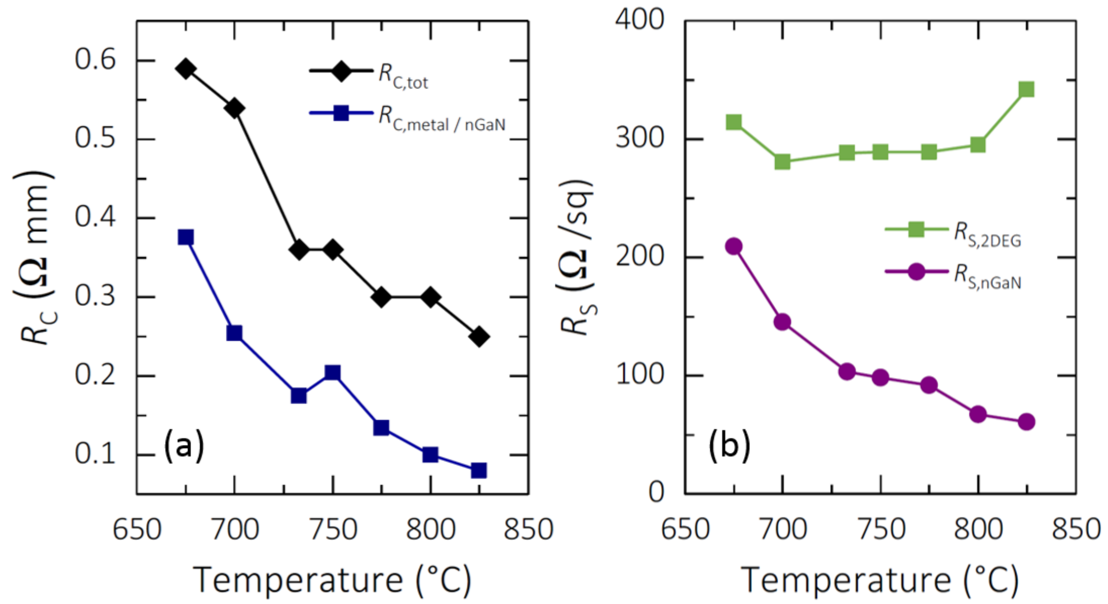

Figure 7.8 – TLM measurements of regrown ohmic contacts as a function of regrowth temperature. (a) Total contact resistance (black diamonds) and contact resistance between metal stack and regrowth (blue diamonds) (b) Sheet resistance of 2DEG (green squares) and sheet resistance of regrown n^{++} GaN (purple circles).

were $1.28/1.05 \times 10^{13}$ cm^{-2} and 1800/1850 cm^2 V^{-1} s^{-1}, respectively. This suggests that the electronic properties of InAlN-based HEMTs do not deteriorate during regrowth of ohmic contacts at 825 °C.

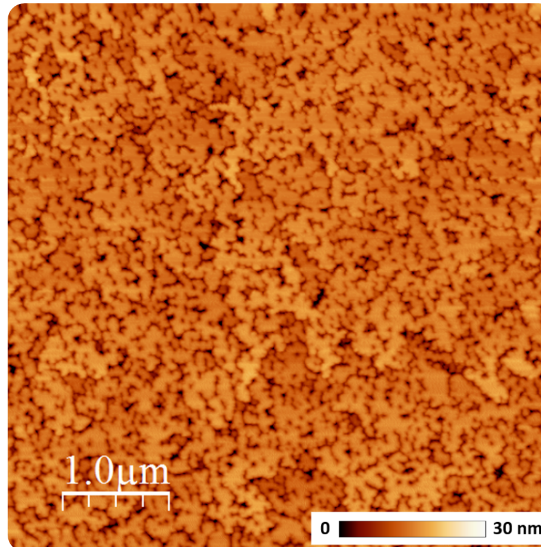

Figure 7.9 – 5×5 μm^2 AFM scan of an optimized 70 nm thick n^{++} GaN layer grown on unintentionally doped GaN templates on sapphire at 825 °C.

In Fig. 7.9, the AFM scan shows the surface morphology for an n^{++} GaN layer grown under growth conditions used for regrowth (825 °C) on a GaN template on sapphire, giving a RMS surface roughness of 3.6 nm, which is low considering the low temperature and the presence of Si.

7.2.5 Summary

In this chapter, the growth of low temperature highly Si-doped GaN by MOVPE was investigated for the fabrication of low resistance ohmic contacts for HEMTs. The electronic properties of n^{++} GaN layers grown on GaN templates on sapphire were optimized by modifying growth parameters such as temperature and SiH_4 flow. Carrier densities for n^{++} GaN above 1×10^{20} cm^{-2} were achieved for growth temperatures below 800 °C. Next, the SiO_x hardmask stoichiometry was optimized in order to achieve selective growth and full removal of mask after regrowth. The optimized growth conditions were used to grow ohmic contacts on InAlN/GaN HEMT structures, giving rise to a low contact resistance of 0.25 Ω mm at 825 °C.

8 Conclusions

8.1 Summary

In this thesis, several distinct problems in III-nitride electronics were investigated. In this final chapter, the main results are summarized. This is followed by an outlook on potential future research.

The evolution of strain relaxation of GaN grown on AlN was studied *in situ* by RHEED. A strong temperature dependence was observed for the critical thickness and strain relaxation rate. Furthermore, the impact of initial dislocation density was examined by comparing the growth of GaN on AlN template on sapphire (~ 10^8 cm^{-2}) and AlN single crystal (~ 10^3 cm^{-2}). The critical thickness for plastic strain relaxation is 3 MLs on both substrates at high temperature (900 °C). This is in line with theoretical predictions assuming near-equilibrium growth conditions. However, as the growth temperature is lowered (750 °C), the critical thickness drastically increases to 16 and 35 MLs for AlN template on sapphire and AlN single crystal, respectively, likely due to a much lower dislocation density in the latter. The strain relaxation process freezes out as the temperature is lowered. Pre-existing dislocations are known to be thermally activated. Hence, at low temperature, their mobility is reduced hindering their motion and multiplication. A thermal activation energy of 2.2 eV was extracted from temperature-dependent strain relaxation slopes, which is in line with previously reported values. Furthermore, the high activation energy (compared to conventional III-V semiconductors) supports the presence of kinetic barriers hindering strain relaxation at low temperatures. Growth interruption measurements showed that at high temperature (900 °C) the strain relaxation is governed by temperature, whereas at low temperature (750 °C) the increase in strain energy with thickness determines the relaxation. In order to further increase the critical thickness, the temperature was lowered to 700 °C. Kinetic roughening of the surface morphology was prevented by adjusting the growth conditions in order to enhance adatom mobility.

The low electron mobility observed in AlN/GaN/AlN heterostructures was studied by a series of growths both by MOVPE and MBE. A high dislocation density introduced at the early stages of growth by plastic strain relaxation (due to the large lattice-mismatch between GaN

and AlN) is suggested as the limiting scattering mechanism for thin GaN channel 2DEGs grown on AlN. The electron mobility drastically decreases as the GaN channel thickness is reduced. Furthermore, the electron mobility was shown to be independent of barrier and substrate type. The impact of 2DEG carrier density on the electron mobility was investigated by a series of growth with increasing barrier thickness. The electron mobility increases with carrier density, which suggests that 2DEG carriers have a screening effect on the charged dislocations. A theoretical model for charged dislocation scattering was used to extract the dislocation density. The obtained value (5×10^{11} cm^{-2}) is in good agreement with reports in literature (7×10^{11} cm^{-2}). Furthermore, modulation-doped heterostructures with ultra-thin GaN channels were explored, giving reasonably high electron mobilities, compared to the conventional AlN/GaN/AlN structure.

The electronic properties of InGaN channel 2DEGs were studied as a function of indium content. The electron mobility drastically drops as the In content is increased above 2%. This is in line with the linewidth broadening observed in optical measurements. Furthermore, the electron mobility was modeled using a modified alloy scattering term. Alloy disorder is identified as the dominating scattering mechanism for In-rich InGaN channels at room-temperature. The high electron mobilities for In-rich InGaN channels reported in literature is suggested to be caused by two external reasons. (i) Temperature ramps above the growth temperature of the InGaN channel give rise to In desorption, leaving behind a low-In content or In-free GaN thin layer. (ii) The unintentional growth of GaN due to parasitic Ga atoms present in the growth chamber, in particular, showerheads of vertical MOVPE reactors. In both cases, a thin GaN interlayer is formed between the barrier and the InGaN channel. Calculations show that the 2DEG electron density redistributes in the presence of a GaN interlayer. The effective electron mobility is therefore higher since the carriers can propagate partially through the GaN interlayer and avoid strong alloy scattering of the In-rich InGaN channel.

The growth of low temperature highly Si-doped GaN by MOVPE was investigated to be used as an alternative to regrowth by MBE for the fabrication of ohmic contacts for HEMTs. The low temperature n^{++} GaN was optimized by varying growth parameters such as temperature and silane flow. The SiO_x hardmask stoichiometry was also optimized in order to achieve selective growth and full removal after regrowth. Carrier densities above 1×10^{20} cm^{-3} were achieved for growth temperatures below 800 °C. The optimized growth conditions were applied to the regrowth of ohmic contacts on InAlN/GaN HEMTs and a low contact resistance of 0.25 Ω mm was achieved at 825 °C.

The low temperature growth of highly Si-doped GaN by MOVPE was also used for the fabrication of low resistivity tunnel junctions on blue LEDs (Appendix A). Highly Si-doped n^{++} GaN layers were grown at low temperature (< 800 °C) on the p^{++} GaN top surface in order to hinder Mg-passivation by H_2. The tunnel junctions were further improved by the insertion of 5 nm thick $In_{0.15}Ga_{0.85}N$ interlayers thanks to the piezoelectric polarization induced band bending.

8.2 Outlook

- **AlN/GaN/AlN heterostructures:** As discussed in the previous section, the critical thickness for GaN grown on AlN can be significantly increased by reducing the growth temperature. During this thesis the growth method was restricted to NH_3-MBE and MOVPE, which generally require high growth temperatures. On the other hand, growth by PA-MBE is performed at much lower temperatures, which could enable thicker pseudomorphic GaN layers on AlN to be used in AlN/GaN/AlN HEMTs. The proposed MODFET heterostructures could be optimized in terms of doping and thicknesses in order to achieve higher electron mobilities for pseudomorphic ultra-thin GaN channels. Modulation-doping could possibly enable very high 2DEG densities, since it is not limited by the interface polarization charges.

- **InGaN channels:** Electron transport measurements on InGaN channel nanostructures could potentially be used to study alloy disorder and Anderson localization [170, 171] which would complement recent work done by optical measurements [172]. The strong impact of alloy disorder on the transport properties of 2DEGs could also be used to trigger a transition between a conducting and insulating states by shifting the Fermi Energy level above/below the disorder-induced localized states. Furthermore, InGaN interlayers could have potential applications as back-barriers in electronic devices [173] improving the 2DEG confinement.

- **Low temperature growth of n^{++} GaN by MOVPE:** For the regrowth of ohmic contacts for HEMTs, the contact resistance could be further optimized to reach values previously achieved by MBE. The surface morphology could be improved by using In as a surfactant. In the case of AlGaN/GaN HEMTs the regrowth temperature could possibly be increased significantly (950 °C) in order to further improve the contact resistance without degrading the electronic properties of the 2DEG.

A Tunnel junctions by MOVPE

In this chapter, the growth of low temperature n^{++} GaN by MOVPE (discussed in Sec. 7.2.1) is used to fabricate tunnel junctions (TJ) on activated commercial blue LED epiwafers.
The material used in this chapter was published [167] and reproduced with permission from IOP.

A.1 Background

For heavily doped (degenerate) p-n junctions, the depletion region shrinks to a few nanometers, allowing for interband quantum tunneling of carriers from the conduction band to valence band and vice versa. This so called TJ gives rise to an anomalous negative differential resistance in the forward voltage direction and was first observed in 1958 by Esaki [174] in highly p-n doped Ge junctions. The probability of tunneling depends on the barrier height, depletion width and the carrier effective mass. A detailed description of tunnel junctions and their applications can be found in literature [175]. Essentially, TJs can be used for the injection of holes into a p-type region while having an n-type top layer, allowing low resistivity n-type contacts. This is of particular interest in III-nitride LEDs due to the low conductivity of the p-type (Mg-doped) material, which limits the device performance. Furthermore, the addition of an interlayer (into the TJ) will reduce the depletion width when the electric field is in the same direction as the field in the p-n junction. TJs in III-nitrides have been shown to give rise to excellent electrical characteristics despite the low tunneling probability (wide band gap and large effective electron mass) likely due to defect assisted tunneling. Furthermore, band bending makes the tunneling process more favorable (high polarization fields).
In particular, high-power visible LEDs suffer from issues related to efficiency droop at high current densities. Akyol *et al.* [176] proposed an approach based on cascaded LEDs connected by TJs. Furthermore, TJs could potentially replace indium-tin-oxide (ITO) transparent contacts for high power LEDs, ultraviolet LEDs [177], white LEDs [178], microLEDs [179], LDs [180, 181] and vertical cavity surface emitting lasers (VCSELs) [182]. Additionally, the high contact resistance and high absorption of the ITO layer at short wavelengths [183] can

be avoided. TJs have been proven to be excellent substitutes to metal contacts as shown by Yonkee *et al.* demonstrating blue LEDs with an external quantum efficiency (EQE) exceeding 70 % [184]. Furthermore, TJs have been shown to reduce the droop efficiency in green LEDs [185].

Takeuchi *et al.* [186] reported the first InGaN/GaN-based TJ in 2001, which was performed by MOVPE. In 2010 Krishnamoorthy *et al.* [187] demonstrated low resistivity TJs achieved by MBE, which allowed for much lower growth temperatures compared to MOVPE, hindering the passivation of the Mg acceptor. In recent years, TJs have been reported with specific differential resistances as low as $1.2\times10^{-4}\ \Omega\ \mathrm{cm}^2$ by PA-MBE [188] and $3.7\times10^{-4}\ \Omega\ \mathrm{cm}^2$ by NH_3-MBE [179]. In 2016 a hybrid approach was proposed [189] in which a low temperature n^{++} GaN layer is grown on the activated p^{++} GaN LED surface. This led to a series of high performance optoelectronic devices such as LEDs [189, 190], LDs [180] and VCSELs [182].

On the other hand, MOVPE is the standard growth technique for manufacturing III-nitride-based optoelectronic devices. Hence, an all-MOVPE grown GaN-based TJ would be highly desirable. However, during the growth of the n^{++} GaN layer, the Mg acceptors in the p^{++} top surface might get passivated. The passivation starts at 500 °C under NH_3 [191], which corresponds to the decomposition temperature thereof [94]. For achieving low-resistivity TJs by MOVPE, the growth temperature should be low enough in order to avoid passivation and subsequent annealing steps [192–194], which potentially might deteriorate the electronic properties. In the following section the application of low temperature growth n^{++} GaN by MOVPE (discussed in Chap. 7.2.1) will be applied to GaN-based TJs on commercial LED wafers.

A.2 Tunnel junctions on blue LEDs by MOVPE

The TJs were formed by growing n^{++} GaN layers on activated 455 nm LED wafers (supplied by PAM-XIAMEN). The structure of LED and TJ are illustrated in Fig. A.1(b). A thin (5 nm thick) n^{++} interlayer is grown on the activated LED wafer. Then, a 150 nm thick n^{+} GaN spreading layer is grown at a slightly higher growth temperature (740 °C) in order to keep a smooth surface morphology. Finally, a 10 nm thick n^{++} GaN cap is grown. Five different samples were prepared with interlayers as described in Tab. A.1. All interlayers were heavily doped ($1\text{-}2\times10^{20}\ \mathrm{cm}^{-3}$). LEDs were fabricated ($100\times100\ \mu\mathrm{m}^2$) using standard photolithography and inductively coupled plasma reactive ion etching. For the top and bottom contacts Ti/Al/Ti/Au metal stack layers were used. Furthermore, a standard LED (p-contact) was fabricated for comparison using Pd/Au and Ti/Al/Ti/Au stacks for the p- and n-type contacts, respectively. In Fig. A.2(a) the J-V characteristics of the LEDs with interlayers described in Tab. A.1 and the reference LED (p-contact) are shown. For the p-contact LED the forward voltage is as low as 2.58 V, which is close to an ideal InGaN/GaN QW p-n junction [195]. The forward voltage increases for a pure GaN interlayer (sample A) to 2.85 V and reduces for InGaN interlayers (samples B and C) to 2.8 and 2.67 V for an In content of 10 and 15 %, respectively. The improvement of the electrical characteristics with InGaN interlayers is

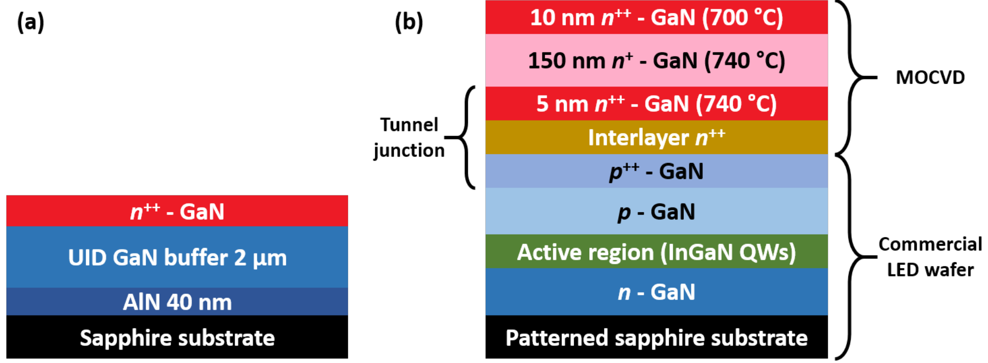

Figure A.1 – Illustration of (a) sample structure used for the study of low temperature highly Si-doped GaN and (b) the tunnel junctions grown on commercial LED wafers. Reproduced and modified from [167] with permission from AIP.

Sample	Interlayer
A	5 nm n^{++} GaN (700 °C)
B	5 nm n^{++} $In_{0.10}Ga_{0.90}N$ (700 °C)
C	5 nm n^{++} $In_{0.15}Ga_{0.85}N$ (700°C)
D	1 nm n^{++} $In_{0.15}Ga_{0.85}N$ (700°C)
E	3 nm n^{++} $In_{0.18}Al_{0.82}N$ (775°C)

Table A.1 – Sample structure, composition, thickness and growth temperature of tunnel junctions grown on blue LED wafers by MOVPE.

in agreement with previous reports [187, 193] and can be ascribed to polarization-assisted band bending. Indeed, as the InGaN interlayer thickness is reduced to 1 nm (sample D) the forward voltage increases. Furthermore, a strong degradation of the TJ forward voltage is observed for an InAlN interlayer. This is consistent with the lower tunneling probability due to the larger band gap of $In_{0.18}Al_{0.82}N$ (~ 4.5 eV). The specific differential resistances (ρ_{sd}) of the samples measured at 1.5 kA cm^{-2} are given in Fig. A.2(c) with sample D exhibiting the lowest resistance of 8.6×10^{-4} Ω cm^2. Since the lowest resistance was achieved for the highest In content (15 %) InGaN interlayer, potential losses due to absorption need to be investigated. Therefore, the EQE of TJ-LEDs were measured and the results are given in Fig. A.3. The EQE was measured from the backside of the planar devices and therefore the value is significantly underestimated. Nevertheless, the measurement can be used to compare the optical absorption for the various interlayers. The maximum EQE was obtained for current densities between 2.5 and 3.8 A cm^{-2}, which is in line with results published by David *et al.* [195]. The highest value of the EQE is obtained for sample E (InAlN interlayer) followed by sample A. With increasing In content of the interlayer the EQE maximum further decreases due to optical losses. It is worth mentioning that the light extraction was not optimized for the TJ-LEDs (due to the additional 170 nm thick multilayer in the LED). Therefore, the optical field maximum and the QWs are no longer perfectly matching. This explains the lower EQE

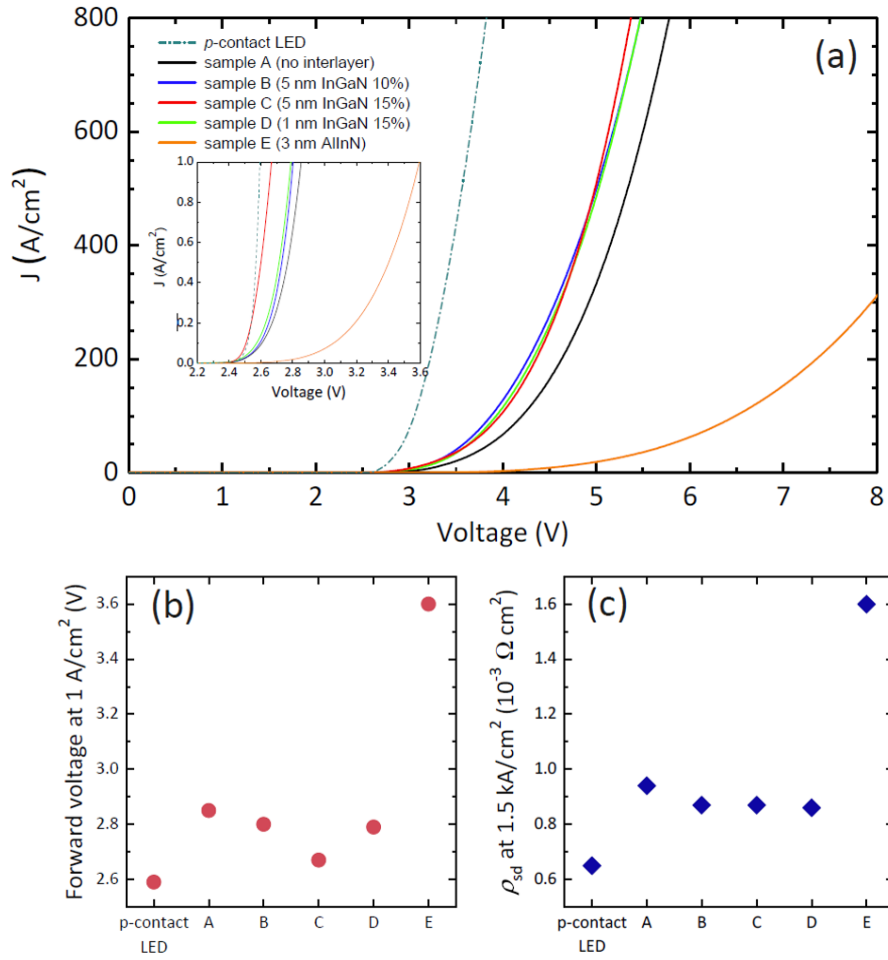

Figure A.2 – (a) Current density (J) as a function of voltage (V) for 100×100 μm^2 LEDs fabricated using the interlayers A-E, together with the p-contact LED sample. The inset shows the same characteristics at lower current density (< 1 A cm^{-2}). (b) LED forward voltage at 1 A cm^{-2}. (c) Specific differential resistance of the TJ LED devices measured at 1.5 kA cm^{-2} for different samples. The horizontal axis refers to samples A to E described in Tab. A.1. Reproduced and modified from [167] with permission from IOP.

compared to the p-contact LED. Furthermore, the top contacts differ between the p-contact and the TJ-LEDs giving rise to different reflectivities.

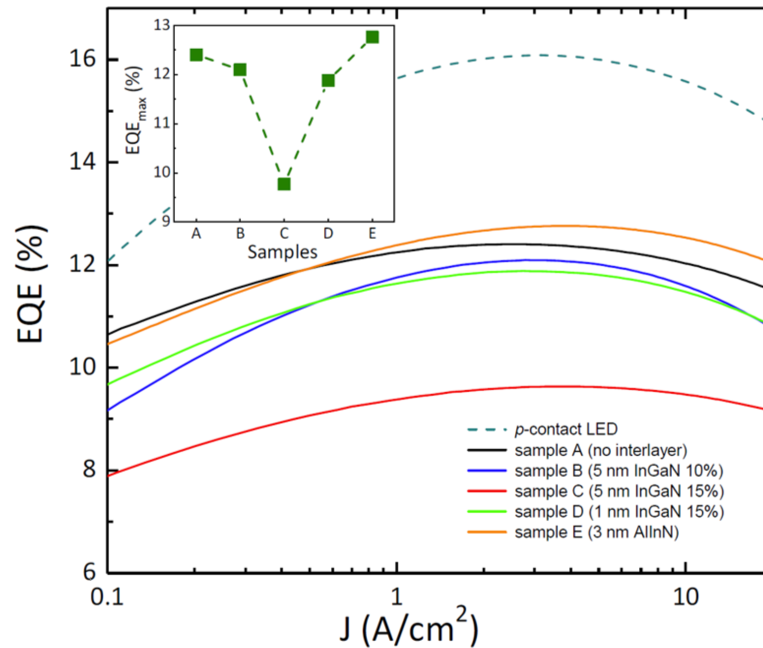

Figure A.3 – EQE as a function of J for 100×100 μm^2 LEDs fabricated using the interlayers A-E, together with the p-contact LED sample. The horizontal axis refers to samples A to E described in Tab. A.1. Reproduced and modified from [167] with permission from IOP.

A.3 Summary

In this chapter, low resistivity tunnel junctions grown by MOVPE on blue LEDs were investigated. Highly Si-doped n^{++} GaN layers were grown at low temperature (< 800 °C) on the p^{++} GaN top surface in order to hinder Mg-passivation by H_2. Tunnel junctions were further improved by inserting 5 nm thick $In_{0.15}Ga_{0.85}N$ interlayers giving rise to a total differential resistance of 8.6×10^{-4} Ω cm^2, operating at 2.67 V at 1 A cm^{-2} and 3.28 V at 20 A cm^{-2}.

B Acronyms

2DEG	Two-dimensional electron gas
2DHG	Two-dimensional hole gas
AFM	Atomic force microscopy
APT	Atom probe tomography
CCD	Charge-coupled device
CV	Capacitance–voltage profiling
CW	Continuous wave
DMSO	Dimethylsulfoxide
EQE	External quantum efficiency
FM	Frank–Van der Merwe
FWHM	Full width at half maximum
HEMT	High electron mobility transistor
HR-XRD	High resolution x-ray diffraction
IPA	Isopropanol
ITO	Indium-tin-oxide
LD	Laser diode
LED	Light emitting diode
MBE	Molecular beam epitaxy
MODFET	Modulation-doped field-effect transistor
MOVPE	Metalorganic vapor-phase epitaxy
PA-MBE	Plasma-assisted molecular beam epitaxy
PECVD	Plasma-enhanced chemical vapor deposition
PL	Photoluminescence
PMMA	Polymethylmethacrylat
PVD	Physical vapor deposition
QW	Quantum well
RF	Radio frequency
RHEED	Reflection high-energy electron diffraction
RMS	Root mean square

RSM	Reciprocal space mapping
SEM	Scanning electron microscopy
SK	Stranski–Krastanov
TEGa	Triethylgallium
TEM	Transmission electron microscopy
TJ	Tunnel junction
TLM	Transmission line measurement
TMAl	Trimethylaluminum
TMGa	Trimethylgallium
TMIn	Trimethylindium
UID	Unintentionally doped
VCSEL	Vertical cavity surface emitting laser
VW	Volmer–Weber
XRR	X-ray reflectivity

Bibliography

[1] S. Nakamura, S. Pearton, and G. Fasol, “The blue laser diode: GaN based light emitters and lasers”, (Springer, Berlin, 2001) .

[2] M. A. Khan, J. N. Kuznia, J. M. Van Hove, N. Pan, and J. Carter, “Observation of a two-dimensional electron gas in low pressure metalorganic chemical vapor deposited GaN-$Al_xGa_{1-x}N$ heterojunctions”, Applied Physics Letters **60**, 3027–3029 (1992).

[3] J. Kuzmík, “Power electronics on InAlN/(In)GaN: Prospect for a record performance”, IEEE Electron Device Letters **22**, 510–512 (2001).

[4] F. Medjdoub, J.-F. Carlin, M. Gonschorek, E. Feltin, M. Py, D. Ducatteau, C. Gaquière, N. Grandjean, and E. Kohn, “Can InAlN/GaN be an alternative to high power/high temperature AlGaN/GaN devices?”, IEEE International Electron Devices Meeting (2006).

[5] E. Kohn and A. Denisenko, “Concepts for diamond electronics”, Thin Solid Films **515**, 4333–4339 (2007).

[6] A. Aleksov, M. Kubovic, N. Kaeb, U. Spitzberg, A. Bergmaier, G. Dollinger, T. Bauer, M. Schreck, B. Stritzker, and E. Kohn, “Diamond field effect transistors—concepts and challenges”, Diamond and Related Materials **12**, 391–398 (2003).

[7] H. Morkoç, “Handbook of Nitride Semiconductors and Devices: Materials Properties, Physics and Growth”, (WILEY-VCH, Weinheim, 2009) .

[8] D. C. Look and J. Sizelove, “Dislocation scattering in GaN”, Physical Review Letters **82**, 1237 (1999).

[9] I. Smorchkova, S. Keller, S. Heikman, C. Elsass, B. Heying, P. Fini, J. Speck, and U. Mishra, “Two-dimensional electron-gas AlN/GaN heterostructures with extremely thin AlN barriers”, Applied Physics Letters **77**, 3998–4000 (2000).

[10] C. Wood and D. Jena, “Polarization Effects in Semiconductors: From Ab Initio Theory to Device Applications”, (Springer Science & Business Media, New York, 2008) .

[11] I. Vurgaftman and J. R. Meyer, “Band parameters for nitrogen-containing semiconductors”, Journal of Applied Physics **94**, 3675–3696 (2003).

[12] F. Bernardini, V. Fiorentini, and D. Vanderbilt, "Accurate calculation of polarization-related quantities in semiconductors", Physical Review B **63**, 193201 (2001).

[13] J. Wu, W. Walukiewicz, W. Shan, K. Yu, J. Ager Iii, S. Li, E. Haller, H. Lu, and W. J. Schaff, "Temperature dependence of the fundamental band gap of InN", Journal of Applied Physics **94**, 4457–4460 (2003).

[14] M. Feneberg, B. Neuschl, K. Thonke, R. Collazo, A. Rice, Z. Sitar, R. Dalmau, J. Xie, S. Mita, and R. Goldhahn, "Sharp bound and free exciton lines from homoepitaxial AlN", Physica Status Solidi (A) **208**, 1520–1522 (2011).

[15] A. Zoroddu, F. Bernardini, P. Ruggerone, and V. Fiorentini, "First-principles prediction of structure, energetics, formation enthalpy, elastic constants, polarization, and piezo-electric constants of AlN, GaN, and InN: Comparison of local and gradient-corrected density-functional theory", Physical Review B **64**, 045208 (2001).

[16] F. Bernardini and V. Fiorentini, "Nonlinear macroscopic polarization in III-V nitride alloys", Physical Review B **64**, 085207 (2001).

[17] T. Onuma, S. Chichibu, Y. Uchinuma, T. Sota, S. Yamaguchi, S. Kamiyama, H. Amano, and I. Akasaki, "Recombination dynamics of localized excitons in $Al_{1-x}In_xN$ epitaxial films on GaN templates grown by metalorganic vapor phase epitaxy", Journal of Applied Physics **94**, 2449–2453 (2003).

[18] B. Lee and L. W. Wang, "Band gap bowing and electron localization of $Ga_xIn_{1-x}N$", Journal of Applied Physics **100**, 093717 (2006).

[19] D. Brunner, H. Angerer, E. Bustarret, F. Freudenberg, R. Höpler, R. Dimitrov, O. Ambacher, and M. Stutzmann, "Optical constants of epitaxial AlGaN films and their temperature dependence", Journal of Applied Physics **82**, 5090–5096 (1997).

[20] C. Van de Walle and J. Neugebauer, "Universal alignment of hydrogen levels in semiconductors, insulators and solutions", Nature **423**, 626–628 (2003).

[21] G. Martin, S. Strite, A. Botchkarev, A. Agarwal, A. Rockett, H. Morkoç, W. Lambrecht, and B. Segall, "Valence-band discontinuity between GaN and AlN measured by x-ray photoemission spectroscopy", Applied Physics Letters **65**, 610–612 (1994).

[22] G. Martin, A. Botchkarev, A. Rockett, and H. Morkoç, "Valence-band discontinuities of wurtzite GaN, AlN, and InN heterojunctions measured by x-ray photoemission spectroscopy", Applied Physics Letters **68**, 2541–2543 (1996).

[23] F. Bernardini, V. Fiorentini, and D. Vanderbilt, "Spontaneous polarization and piezo-electric constants of III-V nitrides", Physical Review B **56**, R10024 (1997).

[24] V. Fiorentini, F. Bernardini, and O. Ambacher, "Evidence for nonlinear macroscopic polarization in III–V nitride alloy heterostructures", Applied Physics Letters **80**, 1204–1206 (2002).

[25] J. P. Ibbetson, P. Fini, K. Ness, S. DenBaars, J. Speck, and U. Mishra, "Polarization effects, surface states, and the source of electrons in AlGaN/GaN heterostructure field effect transistors", Applied Physics Letters **77**, 250–252 (2000).

[26] G. Koley and M. Spencer, "On the origin of the two-dimensional electron gas at the AlGaN/GaN heterostructure interface", Applied Physics Letters **86**, 042107 (2005).

[27] B. Bakeroot, S. You, T.-L. Wu, J. Hu, M. Van Hove, B. De Jaeger, K. Geens, S. Stoffels, and S. Decoutere, "On the origin of the two-dimensional electron gas at AlGaN/GaN heterojunctions and its influence on recessed-gate metal-insulator-semiconductor high electron mobility transistors", Journal of Applied Physics **116**, 134506 (2014).

[28] T. Palacios, A. Chakraborty, S. Rajan, C. Poblenz, S. Keller, S. P. DenBaars, J. S. Speck, and U. K. Mishra, "High-power AlGaN/GaN HEMTs for Ka-band applications", IEEE Electron Device Letters **26**, 781–783 (2005).

[29] M. Gurusinghe, S. Davidsson, and T. Andersson, "Two-dimensional electron mobility limitation mechanisms in $Al_xGa_{1-x}N$/GaN heterostructures", Physical Review B **72**, 045316 (2005).

[30] N. Dharmarasu, K. Radhakrishnan, M. Agrawal, L. Ravikiran, S. Arulkumaran, K. E. Lee, and N. G. Ing, "Demonstration of AlGaN/GaN high-electron-mobility transistors on 100-mm-diameter Si (111) by ammonia molecular beam epitaxy", Applied Physics Express **5**, 091003 (2012).

[31] M. Gonschorek, J.-F. Carlin, E. Feltin, M. Py, and N. Grandjean, "High electron mobility lattice-matched AlInN/GaN field-effect transistor heterostructures", Applied Physics Letters **89**, 062106 (2006).

[32] I. P. Smorchkova, L. Chen, T. Mates, L. Shen, S. Heikman, B. Moran, S. Keller, S. P. DenBaars, J. S. Speck, and U. K. Mishra, "AlN/GaN and (Al,Ga)N/AlN/GaN two-dimensional electron gas structures grown by plasma-assisted molecular-beam epitaxy", Journal of Applied Physics **90**, 5196–5201 (2001).

[33] K. Jeganathan, T. Ide, M. Shimizu, and H. Okumura, "Two-dimensional electron gases induced by polarization charges in AlN/GaN heterostructure grown by plasma-assisted molecular-beam epitaxy", Journal of Applied Physics **94**, 3260–3263 (2003).

[34] Y. Cao and D. Jena, "High-mobility window for two-dimensional electron gases at ultrathin AlN/GaN heterojunctions", Applied Physics Letters **90**, 182112 (2007).

[35] Y. Cao, K. Wang, A. Orlov, H. Xing, and D. Jena, "Very low sheet resistance and Shubnikov–de-Haas oscillations in two-dimensional electron gases at ultrathin binary AlN/GaN heterojunctions", Applied Physics Letters **92**, 152112 (2008).

[36] K. Shinohara, D. C. Regan, Y. Tang, A. L. Corrion, D. F. Brown, J. C. Wong, J. F. Robinson, H. H. Fung, A. Schmitz, T. C. Oh, *et al.*, "Scaling of GaN HEMTs and Schottky diodes for

submillimeter-wave MMIC applications", IEEE Transactions on Electron Devices **60**, 2982–2996 (2013).

[37] J. Xue, J. Zhang, and Y. Hao, "Ultrathin barrier AlN/GaN high electron mobility transistors grown at a dramatically reduced growth temperature by pulsed metal organic chemical vapor deposition", Applied Physics Letters **107**, 043503 (2015).

[38] D. A. Deen, D. F. Storm, D. J. Meyer, R. Bass, S. C. Binari, T. Gougousi, and K. R. Evans, "Impact of barrier thickness on transistor performance in AlN/GaN high electron mobility transistors grown on free-standing GaN substrates", Applied Physics Letters **105**, 093503 (2014).

[39] T. Zimmermann, D. Deen, Y. Cao, J. Simon, P. Fay, D. Jena, and H. G. Xing, "AlN/GaN insulated-gate HEMTs with 2.3 A/mm output current and 480 mS/mm transconductance", IEEE Electron Device Letters **29**, 661–664 (2008).

[40] F. Medjdoub, M. Zegaoui, N. Rolland, and P. Rolland, "Demonstration of low leakage current and high polarization in ultrathin AlN/GaN high electron mobility transistors grown on silicon substrate", Applied Physics Letters **98**, 223502 (2011).

[41] F. Medjdoub, M. Zegaoui, D. Ducatteau, N. Rolland, and P. Rolland, "High-performance low-leakage-current AlN/GaN HEMTs grown on silicon substrate", IEEE Electron Device Letters **32**, 874–876 (2011).

[42] S. Rennesson, M. Leroux, M. Al Khalfioui, M. Nemoz, S. Chenot, J. Massies, L. Largeau, E. Dogmus, M. Zegaoui, F. Medjdoub, and F. Semond, "Ultrathin AlN-Based HEMTs Grown on Silicon Substrate by NH_3-MBE", Physica Status Solidi (A) Applications and Materials Science **215**, 1700640 (2018).

[43] G. Li, B. Song, S. Ganguly, M. Zhu, R. Wang, X. Yan, J. Verma, V. Protasenko, H. Grace Xing, and D. Jena, "Two-dimensional electron gases in strained quantum wells for AlN/GaN/AlN double heterostructure field-effect transistors on AlN", Applied Physics Letters **104**, 193506 (2014).

[44] G. Li, R. Wang, J. Guo, J. Verma, Z. Hu, Y. Yue, F. Faria, Y. Cao, M. Kelly, T. Kosel, H. Xing, and D. Jena, "Ultrathin body GaN-on-insulator quantum well FETs with regrown ohmic contacts", IEEE Electron Device Letters **33**, 661–663 (2012).

[45] A. Bairamis, C. Zervos, A. Adikimenakis, A. Kostopoulos, M. Kayambaki, K. Tsagaraki, G. Konstantinidis, and A. Georgakilas, "Electron density and currents of AlN/GaN high electron mobility transistors with thin GaN/AlN buffer layer", Applied Physics Letters **105**, 113508 (2014).

[46] F. Medjdoub, J. Derluyn, K. Cheng, M. Leys, S. Degroote, D. Marcon, D. Visalli, M. Van Hove, M. Germain, and G. Borghs, "Low on-resistance high-breakdown normally off AlN/GaN/AlGaN DHFET on Si substrate", IEEE Electron Device Letters **31**, 111–113 (2010).

[47] X. Hu, J. Deng, N. Pala, R. Gaska, M. S. Shur, C. Q. Chen, J. Yang, G. Simin, M. A. Khan, J. C. Rojo, and L. J. Schowalter, “AlGaN/GaN heterostructure field-effect transistors on single-crystal bulk AlN”, Applied Physics Letters **82**, 1299–1301 (2003).

[48] L. Lugani, J.-F. Carlin, M. A. Py, D. Martin, F. Rossi, G. Salviati, P. Herfurth, E. Kohn, J. Bläsing, A. Krost, and N. Grandjean, “Ultrathin InAlN/GaN heterostructures on sapphire for high on/off current ratio high electron mobility transistors”, Journal of Applied Physics **113**, 214503 (2013).

[49] S. Kolluri, S. Keller, D. Brown, G. Gupta, S. Rajan, S. P. DenBaars, and U. K. Mishra, “Influence of AlN interlayer on the anisotropic electron mobility and the device characteristics of N-polar AlGaN/GaN metal-insulator-semiconductor-high electron mobility transistors grown on vicinal substrates”, Journal of Applied Physics **108**, 074502 (2010).

[50] U. Singisetti, M. Hoi Wong, and U. K. Mishra, “Interface roughness scattering in ultrathin N-polar GaN quantum well channels”, Applied Physics Letters **101**, 012101 (2012).

[51] U. Singisetti, M. H. Wong, and U. K. Mishra, “High-performance N-polar GaN enhancement-mode device technology”, Semiconductor Science and Technology **28**, 074006 (2013).

[52] U. Singisetti, M. H. Wong, S. Dasgupta, J. S. Speck, and U. K. Mishra, “Enhancement-mode N-polar GaN metal–insulator–semiconductor field effect transistors with current gain cutoff frequency of 120 GHz”, Applied Physics Express **4**, 024103 (2011).

[53] D. F. Brown, S. Rajan, S. Keller, Y.-H. Hsieh, S. P. DenBaars, and U. K. Mishra, “Electron mobility in N-polar GaN/AlGaN/GaN heterostructuress”, Applied Physics Letters **93**, 042104 (2008).

[54] S. Dasgupta, Nidhi, D. F. Brown, F. Wu, S. Keller, J. S. Speck, and U. K. Mishra, “Ultralow nonalloyed ohmic contact resistance to self aligned N-polar GaN high electron mobility transistors by In(Ga)N regrowth”, Applied physics letters **96**, 143504 (2010).

[55] S. Nakamura, “InGaN-based violet laser diodes”, Semiconductor Science and Technology **14**, R27 (1999).

[56] T. Miyajima, T. Tojyo, T. Asano, K. Yanashima, S. Kijima, T. Hino, M. Takeya, S. Uchida, S. Tomiya, K. Funato, *et al.*, “GaN-based blue laser diodes”, Journal of Physics: Condensed Matter **13**, 7099 (2001).

[57] F. C. Frank and J. H. van der Merwe, “One-Dimensional Dislocations. I. Static Theory”, Proceedings of the Royal Society A: Mathematical, Physical and Engineering Sciences **198**, 205–216 (1949).

[58] J. H. van der Merwe, “Strain relaxation in epitaxial overlayers”, Journal of Electronic Materials **20**, 793–803 (1991).

[59] J. Matthews and A. Blakeslee, "Defects in epitaxial multilayers", Journal of Crystal Growth **27**, 118–125 (1974).

[60] J. Matthews, S. Mader, and T. Light, "Accommodation of misfit across the interface between crystals of semiconducting elements or compounds", Journal of Applied Physics **41**, 3800–3804 (1970).

[61] J. Kui and W. A. Jesser, "Thermal Relaxation in Strained InGaAs/GaAs Heterostructures", Journal of Electronic Materials **20**, 827–831 (1991).

[62] G. L. Price, "Critical-thickness and growth-mode transitions in highly strained $In_xGa_{1-x}As$ films", Physical Review Letters **66**, 469–472 (1991).

[63] W. A. Jesser and B. A. Fox, "On the generation of misfit dislocations", Journal of Electronic Materials **19**, 1289–1297 (1990).

[64] W. A. Jesser and J. Kui, "Misfit dislocation generation mechanisms in heterostructures", Materials Science and Engineering: A **164**, 101–110 (1993).

[65] S. Jain, J. Willis, and R. Bullough, "A review of theoretical and experimental work on the structure of Ge_xSi_{1-x} strained layers and superlattices, with extensive bibliography", Advances in Physics **39**, 127–190 (1990).

[66] R. People and J. Bean, "Calculation of critical layer thickness versus lattice mismatch for Ge_xSi_{1-x}/Si strained-layer heterostructures", Applied Physics Letters **47**, 322–324 (1985).

[67] B. W. Dodson and J. Y. Tsao, "Relaxation of strained-layer semiconductor structures via plastic flow", Applied Physics Letters **51**, 1325 (1987).

[68] A. Fischer, H. Kühne, and H. Richter, "New approach in equilibrium theory for strained layer relaxation", Physical Review Letters **73**, 2712–2715 (1994).

[69] B. Daudin, F. Widmann, G. Feuillet, Y. Samson, M. Arléry, and J. L. Rouvière, "Stranski-Krastanov growth mode during the molecular beam epitaxy of highly strained GaN", Physical Review B **56**, R7069–R7072 (1997).

[70] B. Daudin, G. Feuillet, G. Mula, H. Mariette, J. Rouvière, N. Pelekanos, G. Fishman, C. Adelmann, and J. Simon, "Molecular beam epitaxy of GaN, AlN, InN and related alloys: from two-to three-dimensional growth mode", Diamond and Related Materials **9**, 506–511 (2000).

[71] G. Feuillet, B. Daudin, F. Widmann, J. Rouvière, and M. Arléry, "Plastic versus elastic misfit relaxation in III-nitrides grown by molecular beam epitaxy", Journal of Crystal Growth **189-190**, 142–146 (1998).

[72] B. Damilano, N. Grandjean, F. Semond, J. Massies, and M. Leroux, "From visible to white light emission by GaN quantum dots on Si(111) substrate", Applied Physics Letters **75**, 962 (1999).

[73] N. Grandjean and J. Massies, "GaN and $Al_xGa_{1-x}N$ molecular beam epitaxy monitored by reflection high-energy electron diffraction", Applied Physics letters **71**, 1816–1818 (1997).

[74] R. Langer, A. Barski, A. Barbier, G. Renaud, M. Leszczynski, I. Grzegory, and S. Porowski, "Strain relaxation in AlN epitaxial layers grown on GaN single crystals", Journal of Crystal Growth **205**, 31–35 (1999).

[75] E. Bellet-Amalric, "Plastic strain relaxation of nitride heterostructures", Journal of Applied Physics **95**, 1127 (2004).

[76] J. Floro, D. Follstaedt, P. Provencio, S. Hearne, and S. Lee, "Misfit dislocation formation in the AlGaN/GaN heterointerface", Journal of Applied Physics **96**, 7087–7094 (2004).

[77] B. Jahnen, M. Albrecht, W. Dorsch, S. Christiansen, H. P. Strunk, D. Hanser, and R. F. Davis, "Pinholes, dislocations and strain relaxation in InGaN", MRS Internet Journal of Nitride Semiconductor Research **3**, 1–12 (1998).

[78] D. Holec, Y. Zhang, D. V. S. Rao, M. J. Kappers, C. McAleese, and C. J. Humphreys, "Equilibrium critical thickness for misfit dislocations in III-nitrides", Journal of Applied Physics **104**, 123514 (2008).

[79] K. Chinkyo, I. K. Robinson, M. Jaemin, S. Kyuhwan, Y. Myung-Cheol, and K. Kyekyoon, "Critical thickness of GaN thin films on sapphire (0001)", Applied Physics Letters **69**, 2358–2360 (1996).

[80] S. Srinivasan, L. Geng, R. Liu, F. A. Ponce, Y. Narukawa, and S. Tanaka, "Slip systems and misfit dislocations in InGaN epilayers", Applied Physics Letters **83**, 5187–5189 (2003).

[81] M. A. Moram, T. C. Sadler, M. Häberlen, M. J. Kappers, and C. J. Humphreys, "Dislocation movement in GaN films", Applied Physics Letters **97**, 261907 (2010).

[82] I. Yonenaga, Y. Ohno, T. Taishi, and Y. Tokumoto, "Recent knowledge of strength and dislocation mobility in wide band-gap semiconductors", Physica B: Condensed Matter **404**, 4999–5001 (2009).

[83] A. Bourret, C. Adelmann, B. Daudin, J.-L. Rouvière, G. Feuillet, and G. Mula, "Strain relaxation in (0001) AlN/GaN heterostructures", Physical Review B **63**, 245307 (2001).

[84] J. Speck and S. Rosner, "The role of threading dislocations in the physical properties of GaN and its alloys", Physica B: Condensed Matter **273**, 24–32 (1999).

[85] N. G. Weimann, L. F. Eastman, D. Doppalapudi, H. M. Ng, and T. D. Moustakas, "Scattering of electrons at threading dislocations in GaN", Journal of Applied Physics **83**, 3656–3659 (1998).

[86] D. Jena, A. C. Gossard, and U. K. Mishra, "Dislocation scattering in a two-dimensional electron gas", Applied Physics Letters **76**, 1707–1709 (2000).

[87] S. W. Kaun, M. H. Wong, U. K. Mishra, and J. S. Speck, "Correlation between threading dislocation density and sheet resistance of AlGaN/AlN/GaN heterostructures grown by plasma-assisted molecular beam epitaxy", Applied Physics Letters **100**, 262102 (2012).

[88] S. W. Kaun, P. G. Burke, M. Hoi Wong, E. C. Kyle, U. K. Mishra, and J. S. Speck, "Effect of dislocations on electron mobility in AlGaN/GaN and AlGaN/AlN/GaN heterostructures", Applied Physics Letters **101**, 262102 (2012).

[89] D. Jena and U. Mishra, "Effect of scattering by strain fields surrounding edge dislocations on electron transport in two-dimensional electron gases", Applied Physics Letters **80**, 64–66 (2002).

[90] E. Bauer and J. H. van der Merwe, "Structure and growth of crystalline superlattices: From monolayer to superlattice", Physical Review B **33**, 3657 (1986).

[91] P. Politi, G. Grenet, A. Marty, A. Ponchet, and J. Villain, "Instabilities in crystal growth by atomic or molecular beams", Physics Reports **324**, 271–404 (2000).

[92] A. Y. Cho and J. Arthur, "Molecular beam epitaxy", Progress in Solid State Chemistry **10**, 157–191 (1975).

[93] D. C. Tsui, H. L. Stormer, and A. C. Gossard, "Two-dimensional magnetotransport in the extreme quantum limit", Physical Review Letters **48**, 1559 (1982).

[94] M. Mesrine, N. Grandjean, and J. Massies, "Efficiency of NH_3 as nitrogen source for GaN molecular beam epitaxy", Applied Physics Letters **72**, 350–352 (1998).

[95] H. Manasevit and W. I. Simpson, "The Use of Metal-Organics in the Preparation of Semiconductor Materials I. Epitaxial Gallium-V Compounds", Journal of The Electrochemical Society **116**, 1725–1732 (1969).

[96] W. Braun, "Applied RHEED: reflection high-energy electron diffraction during crystal growth", (Springer Science & Business Media, Berlin, 1999) .

[97] J. Harris, B. Joyce, and P. Dobson, "Oscillations in the surface structure of Sn-doped GaAs during growth by MBE", Surface Science Letters **103**, L90–L96 (1981).

[98] C. E. Wood, "RED intensity oscillations during MBE of GaAs", Surface Science **108**, L441–L443 (1981).

[99] J. Van Hove, C. Lent, P. Pukite, and P. Cohen, “Damped oscillations in reflection high energy electron diffraction during GaAs MBE”, Journal of Vacuum Science & Technology B: Microelectronics Processing and Phenomena **1**, 741–746 (1983).

[100] J. Neave, B. Joyce, P. Dobson, and N. Norton, “Dynamics of film growth of GaAs by MBE from RHEED observations”, Applied Physics A **31**, 1–8 (1983).

[101] G. K. Binnig, “Atomic force microscope and method for imaging surfaces with atomic resolution”, US Patent RE33,387 (1990).

[102] I. Miccoli, F. Edler, H. Pfnür, and C. Tegenkamp, “The 100th anniversary of the four-point probe technique: the role of probe geometries in isotropic and anisotropic systems”, Journal of Physics: Condensed Matter **27**, 223201 (2015).

[103] F. Wenner, The four-terminal conductor and the Thomson bridge, US Government Printing Office (1913).

[104] L. J. van der Pauw, “A method of measuring specific resistivity and Hall effect of discs of arbitrary shape”, Philips Res. Rep **13**, 1–9 (1958).

[105] E. H. Hall, “On a new action of the magnet on electric currents”, American Journal of Mathematics **2**, 287–292 (1879).

[106] S. Birner, “Modeling of semiconductor nanostructures and semiconductor-electrolyte interfaces”, Ph.D. thesis, TUM, 2011 .

[107] P. Sohi, D. Martin, and N. Grandjean, “Critical thickness of GaN on AlN: Impact of growth temperature and dislocation density”, Semiconductor Science and Technology **32**, 075010 (2017).

[108] H. J. Osten and J. Klatt, “In situ monitoring of strain relaxation during antimony-mediated growth of Ge and $Ge_{1-y}C_y$ layers on Si(001) using reflection high energy electron diffraction”, Applied Physics Letters **65**, 630–632 (1994).

[109] M. J. Ekenstedt, S. M. Wang, and T. G. Andersson, “Temperature-dependent critical layer thickness for $In_{0.36}Ga_{0.64}As$/GaAs single quantum wells”, Applied Physics Letters **58**, 854 (1991).

[110] G. J. Whaley and P. I. Cohen, “Relaxation of strained InGaAs during molecular beam epitaxy”, Applied Physics Letters **57**, 144 (1990).

[111] J. L. Vassent, M. Dynna, A. Marty, B. Gilles, and G. Patrat, “A study of growth and the relaxation of elastic strain in MgO on Fe(001)”, Journal of Applied Physics **80**, 5727 (1996).

[112] B. P. Rodríguez and J. M. Millunchick, “Dislocation dynamics in strain relaxation in GaAsSb/GaAs heteroepitaxy”, Journal of Applied Physics **100**, 044503 (2006).

[113] M. Qi, G. Li, V. Protasenko, P. Zhao, J. Verma, B. Song, S. Ganguly, M. Zhu, Z. Hu, X. Yan, A. Mintairov, H. G. Xing, and D. Jena, "Dual optical marker Raman characterization of strained GaN-channels on AlN using AlN/GaN/AlN quantum wells and 15N isotopes", Applied Physics Letters **106**, 041906 (2015).

[114] L. Sugiura, "Dislocation motion in GaN light-emitting devices and its effect on device lifetime", Journal of Applied Physics **81**, 1633 (1997).

[115] N. A. Kaufmann, L. Lahourcade, B. Hourahine, D. Martin, and N. Grandjean, "Critical impact of Ehrlich–Schwöbel barrier on GaN surface morphology during homoepitaxial growth", Journal of Crystal Growth **433**, 36–42 (2016).

[116] N. Grandjean, J. Massies, and V. Etgens, "Delayed relaxation by surfactant action in highly strained III-V semiconductor epitaxial layers", Physical Review Letters **69**, 796 (1992).

[117] G. Li, B. Song, S. Ganguly, M. Zhu, R. Wang, X. Yan, J. Verma, V. Protasenko, H. Grace Xing, and D. Jena, "Two-dimensional electron gases in strained quantum wells for Al-N/GaN/AlN double heterostructure field-effect transistors on AlN", Applied Physics Letters **104**, 193506 (2014).

[118] M. Qi, G. Li, S. Ganguly, P. Zhao, X. Yan, J. Verma, B. Song, M. Zhu, K. Nomoto, H. Xing, and D. Jena, "Strained GaN quantum-well FETs on single crystal bulk AlN substrates", Applied Physics Letters **110**, 063501 (2017).

[119] D. B. Laks and A. Zunger, "Theory of interfacial stability of semiconductor superlattices", Physical Review B **45**, 14177–14188 (1992).

[120] P. Bogusławski, K. Rapcewicz, and J. Bernholc, "Surface segregation and interface stability of AlN/GaN, GaN/InN, and AlN/InN (0001) epitaxial systems", Physical Review B - Condensed Matter and Materials Physics **61**, 10820–10826 (2000).

[121] K. Kishino, A. Kikuchi, H. Kanazawa, and T. Tachibana, "Intersubband transition in $(GaN)_m/(AlN)_n$ superlattices in the wavelength range from 1.08 to 1.61 μm", Applied Physics Letters **81**, 1234–1236 (2002).

[122] S. Nicolay, E. Feltin, J.-F. Carlin, N. Grandjean, L. Nevou, F. H. Julien, M. Schmidbauer, T. Remmele, and M. Albrecht, "Strain-induced interface instability in GaNAlN multiple quantum wells", Applied Physics Letters **91**, 061927 (2007).

[123] B. Mazumder, S. W. Kaun, J. Lu, S. Keller, U. K. Mishra, and J. S. Speck, "Atom probe analysis of AlN interlayers in AlGaN/AlN/GaN heterostructures", Applied Physics Letters **102**, 111603 (2013).

[124] S. Rennesson, F. Lecourt, N. Defrance, M. Chmielowska, S. Chenot, M. Lesecq, V. Hoel, E. Okada, Y. Cordier, and J. C. De Jaeger, "Optimization of $Al_{0.29}Ga_{0.71}N$/GaN high electron mobility heterostructures for high-power/frequency performances", IEEE Transactions on Electron Devices **60**, 3105–3111 (2013).

[125] R. Dingle, H. L. Störmer, A. C. Gossard, and W. Wiegmann, “Electron mobilities in modulation-doped semiconductor heterojunction superlattices”, Applied Physics Letters **33**, 665–667 (1978).

[126] L. Witkowski, T. Drummond, C. Stanchak, and H. Morkoç, “High mobilities in Al_xGa_{1-x}As-GaAs heterojuntions”, Applied Physics Letters **37**, 1033–1035 (1980).

[127] S. Hiyamizu, T. Fujii, T. Mimura, K. Nanbu, J. Saito, and H. Hashimoto, “The effect of growth temperature on the mobility of two-dimensional electron gas in selectively doped GaAs/N-AlGaAs heterostructures grown by MBE”, Japanese Journal of Applied Physics **20**, L455 (1981).

[128] H. Störmer, A. Gossard, W. Wiegmann, and K. Baldwin, “Dependence of electron mobility in modulation-doped GaAs-(AlGa)As heterojunction interfaces on electron density and Al concentration”, Applied Physics Letters **39**, 912–914 (1981).

[129] S. Judaprawira, W. Wang, P. Chao, C. Wood, D. Woodard, and L. Eastman, “Modulation-doped MBE GaAs/n-Al_xGa_{1-x} As MESFETs”, IEEE Electron Device Letters **2**, 14–15 (1981).

[130] R. K. Jana and D. Jena, “Stark-effect scattering in rough quantum wells”, Applied Physics Letters **99**, 12104 (2011).

[131] P. Sohi, J.-F. Carlin, and N. Grandjean, “Alloy disorder limited mobility of InGaN two-dimensional electron gas”, Applied Physics Letters **112**, 262101 (2018).

[132] M. Piccardo, C. K. Li, Y. R. Wu, J. S. Speck, B. Bonef, R. M. Farrell, M. Filoche, L. Martinelli, J. Peretti, and C. Weisbuch, “Localization landscape theory of disorder in semiconductors. II. Urbach tails of disordered quantum well layers”, Physical Review B **95**, 144205 (2017).

[133] R. Butté, L. Lahourcade, T. K. Uzdavinys, G. Callsen, M. Mensi, M. Glauser, G. Rossbach, D. Martin, J.-F. Carlin, S. Marcinkevičius, and N. Grandjean, “Optical absorption edge broadening in thick InGaN layers: Random alloy atomic disorder and growth mode induced fluctuations”, Applied Physics Letters **112**, 032106 (2018).

[134] G. Callsen, R. Butté, and N. Grandjean, “Probing alloy formation using different excitonic species: The particular case of InGaN”, arXiv preprint arXiv:1811.02348 (2018).

[135] N. Pala, S. Rumyantsev, M. Shur, R. Gaska, X. Hu, J. Yang, G. Simin, and M. A. Khan, “Low frequency noise in AlGaN/InGaN/GaN double heterostructure field effect transistors”, Solid-State Electronics **47**, 1099–1104 (2003).

[136] N. Okamoto, K. Hoshino, N. Hara, M. Takikawa, and Y. Arakawa, “MOCVD-grown InGaN-channel HEMT structures with electron mobility of over 1000 $cm^2\ V^{-1}\ s^{-1}$”, Journal of Crystal Growth **272**, 278–284 (2004).

[137] N. Maeda, T. Saitoh, K. Tsubaki, T. Nishida, and N. Kobayashi, “Enhanced electron mobility in AlGaN/InGaN/AlGaN double-heterostructures by piezoelectric effect”, Japanese Journal of Applied Physics, Part 2: Letters **38**, L799–L801 (1999).

[138] C. X. Wang, K. Tsubaki, N. Kobayashi, T. Makimoto, and N. Maeda, “Electron transport properties in AlGaN/InGaN/GaN double heterostructures grown by metalorganic vapor phase epitaxy”, Applied Physics Letters **84**, 2313–2315 (2004).

[139] G. Simin, X. Hu, A. Tarakji, J. Zhang, A. Koudymov, S. Saygi, J. Yang, A. Khan, M. S. Shur, and R. Gaska, “AlGaN/InGaN/GaN Double Heterostructure Field-Effect Transistor”, Japanese Journal of Applied Physics **40**, L1142–L1144 (2001).

[140] H. Ikki, Y. Isobe, D. Iida, M. Iwaya, T. Takeuchi, S. Kamiyama, I. Akasaki, H. Amano, A. Bandoh, and T. Udagawa, “AlGaN/GaInN/GaN heterostructure field-effect transistor”, Physica Status Solidi (A) **208**, 1614–1616 (2011).

[141] G. Simin, A. Koudymov, H. Fatima, J. Zhang, J. Yang, M. A. Khan, X. Hu, A. Tarakji, R. Gaska, and M. S. Shur, “SiO_2/AlGaN/InGaN/GaN MOSDHFETs”, IEEE Electron Device Letters **23**, 458–460 (2002).

[142] R. L. Wang, Y. K. Su, and K. Y. Chen, “Influence of InGaN channel thickness on electrical characteristics of AlGaN/InGaN/GaN HFETs”, Electronics Letters **42**, 718–719 (2006).

[143] Y. Zhang, Z. Wang, S. Xu, D. Chen, W. Bao, J. Zhang, J. Zhang, and Y. Hao, “Studies on the InAlN/InGaN/InAlN/InGaN double channel heterostructures with low sheet resistance”, Applied Physics Letters **111**, 222107 (2017).

[144] Y. Zhang, X. Zhou, S. Xu, Z. Wang, Z. Chen, J. Zhang, J. Zhang, and Y. Hao, “Effects of growth temperature on the properties of InGaN channel heterostructures grown by pulsed metal organic chemical vapor deposition”, AIP Advances **5**, 127102 (2015).

[145] Y. Zhang, X. Zhou, S. Xu, Z. Wang, Y. Zhao, J. Zhang, D. Chen, J. Zhang, and Y. Hao, “Effects of interlayer growth condition on the transport properties of heterostructures with InGaN channel grown on sapphire by metal organic chemical vapor deposition”, Applied Physics Letters **106**, 152101 (2015).

[146] S. Gökden, R. Tülek, A. Teke, J. H. Leach, Q. Fan, J. Xie, Ü. Özgür, H. Morkoç, S. B. Lisesivdin, and E. Özbay, “Mobility limiting scattering mechanisms in nitride-based two-dimensional heterostructures with the InGaN channel”, Semiconductor Science and Technology **25**, 045024 (2010).

[147] J. Liberis, I. Matulioniene, A. Matulionis, E. Sermuksnis, J. Xie, J. H. Leach, and H. Morkoç, “InAlN-barrier HFETs with GaN and InGaN channels”, Physica Status Solidi (A) Applications and Materials Science **206**, 1385–1395 (2009).

[148] O. Laboutin, Y. Cao, W. Johnson, R. Wang, G. Li, D. Jena, and H. Xing, “InGaN channel high electron mobility transistor structures grown by metal organic chemical vapor deposition”, Applied Physics Letters **100**, 121909 (2012).

[149] R. Wang, G. Li, G. Karbasian, J. Guo, F. Faria, Z. Hu, Y. Yue, J. Verma, O. Laboutin, Y. Cao, W. Johnson, G. Snider, P. Fay, D. Jena, and H. Xing, "InGaN channel high-electron-mobility transistors with InAlGaN barrier and f_T/f_{max} of 260/220 GHz", Applied Physics Express **6**, 016503 (2013).

[150] J. Xie, J. H. Leach, X. Ni, M. Wu, R. Shimada, Ü. Özgür, and H. Morkoç, "Electron mobility in InGaN channel heterostructure field effect transistor structures with different barriers", Applied Physics Letters **91**, 262102 (2007).

[151] V. Adivarahan, M. E. Gaevski, M. M. Islam, B. Zhang, Y. Deng, and M. A. Khan, "Double-recessed high-frequency AlInGaN/InGaN/GaN metal-oxide double heterostructure field-effect transistors", IEEE Transactions on Electron Devices **55**, 495–499 (2008).

[152] G. Bastard, "Wave mechanics applied to semiconductor heterostructures", (Editions de Physique, Les Ulis, 1990) .

[153] D. Chattopadhyay, "Alloy scattering in quantum-well structures of semiconductor ternaries", Physical Review B **31**, 1145–1146 (1985).

[154] S. Choi, H. J. Kim, Z. Lochner, J. Kim, R. D. Dupuis, A. M. Fischer, R. Juday, Y. Huang, T. Li, J. Y. Huang, F. A. Ponce, and J. H. Ryou, "Origins of unintentional incorporation of gallium in AlInN layers during epitaxial growth, part I: Growth of AlInN on AlN and effects of prior coating", Journal of Crystal Growth **388**, 137–142 (2014).

[155] J. Kim, Z. Lochner, M. H. Ji, S. Choi, H. J. Kim, J. S. Kim, R. D. Dupuis, A. M. Fischer, R. Juday, Y. Huang, T. Li, J. Y. Huang, F. A. Ponce, and J. H. Ryou, "Origins of unintentional incorporation of gallium in InAlN layers during epitaxial growth, part II: Effects of underlying layers and growth chamber conditions", Journal of Crystal Growth **388**, 143–149 (2014).

[156] G. Naresh-Kumar, A. Vilalta-Clemente, S. Pandey, D. Skuridina, H. Behmenburg, P. Gamarra, G. Patriarche, I. Vickridge, M. A. Di Forte-Poisson, P. Vogt, M. Kneissl, M. Morales, P. Ruterana, A. Cavallini, D. Cavalcoli, C. Giesen, M. Heuken, and C. Trager-Cowan, "Multicharacterization approach for studying InAl(Ga)N/Al(Ga)N/GaN heterostructures for high electron mobility transistors", AIP Advances **4**, 127101 (2014).

[157] J. Kim, M. H. Ji, T. Detchprohm, R. D. Dupuis, A. M. Fischer, F. A. Ponce, and J. H. Ryou, "Effect of Group-III precursors on unintentional gallium incorporation during epitaxial growth of InAlN layers by metalorganic chemical vapor deposition", Journal of Applied Physics **118**, 125303 (2015).

[158] M. Hiroki, Y. Oda, N. Watanabe, N. Maeda, H. Yokoyama, K. Kumakura, and H. Yamamoto, "Unintentional Ga incorporation in metalorganic vapor phase epitaxy of In-containing III-nitride semiconductors", Journal of Crystal Growth **382**, 36–40 (2013).

[159] C.-T. Lee and H.-W. Kao, "Long-term thermal stability of Ti/Al/Pt/Au Ohmic contacts to n-type GaN", Applied Physics Letters **76**, 2364–2366 (2000).

[160] B. Jacobs, M. Kramer, E. Geluk, and F. Karouta, "Optimisation of the Ti/Al/Ni/Au ohmic contact on AlGaN/GaN FET structures", Journal of Crystal Growth **241**, 15–18 (2002).

[161] M. Fay, G. Moldovan, P. Brown, I. Harrison, J. Birbeck, B. Hughes, M. Uren, and T. Martin, "Structural and electrical characterization of AuTiAlTi/AlGaN/GaN ohmic contacts", Journal of Applied Physics **92**, 94–100 (2002).

[162] A. Basu, F. Mohammed, S. Guo, B. Peres, and I. Adesida, "Mo/Al/Mo/Au Ohmic contact scheme for $Al_xGa_{1-x}N$/GaN high electron mobility transistors annealed at 500° C", Journal of Vacuum Science & Technology B: Microelectronics and Nanometer Structures Processing, Measurement, and Phenomena **24**, L16–L18 (2006).

[163] S. Ganguly, B. Song, W. S. Hwang, Z. Hu, M. Zhu, J. Verma, H. Xing, and D. Jena, "AlGaN/GaN HEMTs on Si by MBE with regrown contacts and f_T= 153 GHz", Physica Status Solidi (C) **11**, 887–889 (2014).

[164] L. Lugani, M. Malinverni, S. Tirelli, D. Marti, E. Giraud, J.-F. Carlin, C. Bolognesi, and N. Grandjean, "n^+-GaN grown by ammonia molecular beam epitaxy: Application to regrown contacts", Applied Physics Letters **105**, 202113 (2014).

[165] K. Shinohara, D. Regan, A. Corrion, D. Brown, Y. Tang, J. Wong, G. Candia, A. Schmitz, H. Fung, S. Kim, *et al.*, "Self-aligned-gate GaN-HEMTs with heavily-doped n^+-GaN ohmic contacts to 2DEG", Electron Devices Meeting (2012).

[166] F. Afroz Faria, J. Guo, P. Zhao, G. Li, P. Kumar Kandaswamy, M. Wistey, H. Xing, and D. Jena, "Ultra-low resistance ohmic contacts to GaN with high Si doping concentrations grown by molecular beam epitaxy", Applied Physics Letters **101**, 032109 (2012).

[167] P. Sohi, M. Mosca, Y. Chen, J.-F. Carlin, and N. Grandjean, "Low-temperature growth of n^{++}-GaN by metalorganic chemical vapor deposition to achieve low-resistivity tunnel junctions on blue light emitting diodes", Semiconductor Science and Technology **34**, 015002 (2018).

[168] S. C. Cruz, S. Keller, T. E. Mates, U. K. Mishra, and S. P. DenBaars, "Crystallographic orientation dependence of dopant and impurity incorporation in GaN films grown by metalorganic chemical vapor deposition", Journal of Crystal Growth **311**, 3817 – 3823 (2009).

[169] F. Iacona, G. Ceriola, and F. La Via, "Structural properties of SiO_2 films prepared by plasma-enhanced chemical vapor deposition", Materials Science in Semiconductor Processing **4**, 43–46 (2001).

[170] P. W. Anderson, "Absence of diffusion in certain random lattices", Physical Review **109**, 1492 (1958).

[171] A. Lagendijk, B. Van Tiggelen, and D. S. Wiersma, "Fifty years of Anderson localization", Phys. Today **62**, 24–29 (2009).

[172] W. Hahn, J.-M. Lentali, P. Polovodov, N. Young, S. Nakamura, J. Speck, C. Weisbuch, M. Filoche, Y.-R. Wu, M. Piccardo, *et al.*, "Evidence of nanoscale Anderson localization induced by intrinsic compositional disorder in InGaN/GaN quantum wells by scanning tunneling luminescence spectroscopy", Physical Review B **98**, 045305 (2018).

[173] T. Palacios, A. Chakraborty, S. Heikman, S. Keller, S. DenBaars, and U. Mishra, "AlGaN/-GaN high electron mobility transistors with InGaN back-barriers", IEEE Electron Device Letters **27**, 13–15 (2005).

[174] L. Esaki, "New phenomenon in narrow germanium p-n junctions", Physical Review **109**, 603 (1958).

[175] S. M. Sze and K. K. Ng, "Physics of semiconductor devices", (John wiley & sons, New Jersey, 2006) .

[176] F. Akyol, S. Krishnamoorthy, and S. Rajan, "Tunneling-based carrier regeneration in cascaded GaN light emitting diodes to overcome efficiency droop", Applied Physics Letters **103**, 081107 (2013).

[177] S. Sadaf, S. Zhao, Y. Wu, Y.-H. Ra, X. Liu, S. Vanka, and Z. Mi, "An AlGaN core–shell tunnel junction nanowire light-emitting diode operating in the ultraviolet-C band", Nano Letters **17**, 1212–1218 (2017).

[178] K.-T. Lam, W.-H. Lin, S.-C. Shei, N.-M. Lin, W.-S. Chen, and S.-J. Chang, "White-light emission from GaN-based TJ LEDs coated with red phosphor", IEEE Electron Device Letters **37**, 1150–1153 (2016).

[179] M. Malinverni, D. Martin, and N. Grandjean, "InGaN based micro light emitting diodes featuring a buried GaN tunnel junction", Applied Physics Letters **107**, 051107 (2015).

[180] B. P. Yonkee, E. C. Young, C. Lee, J. T. Leonard, S. P. DenBaars, J. S. Speck, and S. Nakamura, "Demonstration of a III-nitride edge-emitting laser diode utilizing a GaN tunnel junction contact", Optics Express **24**, 7816–7822 (2016).

[181] M. Malinverni, C. Tardy, M. Rossetti, A. Castiglia, M. Duelk, C. Vélez, D. Martin, and N. Grandjean, "InGaN laser diode with metal-free laser ridge using n^+-GaN contact layers", Applied Physics Express **9**, 061004 (2016).

[182] J. Leonard, E. Young, B. Yonkee, D. Cohen, T. Margalith, S. DenBaars, J. Speck, and S. Nakamura, "Demonstration of a III-nitride vertical-cavity surface-emitting laser with a III-nitride tunnel junction intracavity contact", Applied Physics Letters **107**, 091105 (2015).

[183] K. Takehara, K. Takeda, K. Nagata, H. Sakurai, S. Ito, M. Iwaya, T. Takeuchi, S. Kamiyama, I. Akasaki, and H. Amano, "Transparent electrode for UV light-emitting-diodes", Physica Status Solidi (c) **8**, 2375–2377 (2011).

[184] B. Yonkee, E. Young, S. DenBaars, S. Nakamura, and J. Speck, “Silver free III-nitride flip chip light-emitting-diode with wall plug efficiency over 70% utilizing a GaN tunnel junction”, Applied Physics Letters **109**, 191104 (2016).

[185] A. I. Alhassan, E. C. Young, A. Y. Alyamani, A. Albadri, S. Nakamura, S. P. DenBaars, and J. S. Speck, “Reduced-droop green III–nitride light-emitting diodes utilizing GaN tunnel junction”, Applied Physics Express **11**, 042101 (2018).

[186] T. Takeuchi, G. Hasnain, S. Corzine, M. Hueschen, R. P. Schneider Jr, C. Kocot, M. Blomqvist, Y.-l. Chang, D. Lefforge, M. R. Krames, *et al.*, “GaN-based light emitting diodes with tunnel junctions”, Japanese Journal of Applied Physics **40**, L861 (2001).

[187] S. Krishnamoorthy, D. N. Nath, F. Akyol, P. S. Park, M. Esposto, and S. Rajan, “Polarization-engineered GaN/InGaN/GaN tunnel diodes”, Applied Physics Letters **97**, 203502 (2010).

[188] S. Krishnamoorthy, F. Akyol, P. S. Park, and S. Rajan, “Low resistance GaN/InGaN/GaN tunnel junctions”, Applied Physics Letters **102**, 113503 (2013).

[189] E. C. Young, B. P. Yonkee, F. Wu, S. H. Oh, S. P. DenBaars, S. Nakamura, and J. S. Speck, “Hybrid tunnel junction contacts to III–nitride light-emitting diodes”, Applied Physics Express **9**, 022102 (2016).

[190] S. J. Kowsz, E. C. Young, B. P. Yonkee, C. D. Pynn, R. M. Farrell, J. S. Speck, S. P. DenBaars, and S. Nakamura, “Using tunnel junctions to grow monolithically integrated optically pumped semipolar III-nitride yellow quantum wells on top of electrically injected blue quantum wells”, Optics express **25**, 3841–3849 (2017).

[191] S. Nakamura, N. Iwasa, M. Senoh, and T. Mukai, “Hole compensation mechanism of p-type GaN films”, Japanese Journal of Applied Physics **31**, 1258 (1992).

[192] Y. Kuwano, M. Kaga, T. Morita, K. Yamashita, K. Yagi, M. Iwaya, T. Takeuchi, S. Kamiyama, and I. Akasaki, “Lateral hydrogen diffusion at p-GaN Layers in nitride-based light emitting diodes with tunnel junctions”, Japanese Journal of Applied Physics **52**, 08JK12 (2013).

[193] D. Takasuka, Y. Akatsuka, M. Ino, N. Koide, T. Takeuchi, M. Iwaya, S. Kamiyama, and I. Akasaki, “GaInN-based tunnel junctions with graded layers”, Applied Physics Express **9**, 081005 (2016).

[194] S. Neugebauer, M. Hoffmann, H. Witte, J. Bläsing, A. Dadgar, A. Strittmatter, T. Niermann, M. Narodovitch, and M. Lehmann, “All metalorganic chemical vapor phase epitaxy of p/n-GaN tunnel junction for blue light emitting diode applications”, Applied Physics Letters **110**, 102104 (2017).

[195] A. David, C. A. Hurni, N. G. Young, and M. D. Craven, “Electrical properties of III-Nitride LEDs: Recombination-based injection model and theoretical limits to electrical efficiency and electroluminescent cooling”, Applied Physics Letters **109**, 083501 (2016).

Pirouz Sohi

✉ *pirouz.sohi@gmail.com*

pirouz-sohi

Education

2015–2019	**Ph.D. Physics**, Ecole Polytechnique Fédérale de Lausanne (EPFL)
2014–2015	**M.Sc. Physics**, Eidgenössische Technische Hochschule Zürich (ETHZ)
2010–2014	**B. S. Physics**, Eidgenössische Technische Hochschule Zürich (ETHZ)

Professional experience

2015–2019 **Ph.D. Student**, Laboratory of advanced Semiconductors for Photoncis and Electronics (EPFL), Lausanne
Thesis:*Growth and characterization of III-nitride heterostructures*

2015 **Research Associate**, Spin Physics (ETH), Zurich
Project:*Magnetic Resonance Force Microscopy*

2015 **Master Student**, Nanophysics (ETH), Zurich
Thesis:*Local investigation of self-sustaining resistance oscillations at the $\nu = 2/3$ spin phase transition*

Skills

Languages	English, German, Persian, French
Epitaxy	Metalorganic vapour-phase epitaxy, molecular-beam epitaxy
Characterization	High resolution x-ray diffraction, atomic force microscopy, scanning electron microscopy, Hall effect, capacitance–voltage profiling
Fabrication	Photolithography, Electron beam evaporation
Programming	Python, C++, Matlab, LaTeX, Mathematica
Software	Simulaiton: NextNano. CAD: SolidWorks. Instrumentation: LabView. Microcontrollers: Arduino

Conferences

11.2018 **Contributed Talk**, *International Workshop on Nitride Semiconductors*, Kanazawa, Japan.

11.2018 **Contributed Talk**, *International Workshop on Nitride Semiconductors*, Kanazawa, Japan.

4.2018 **Contributed Poster**, *GaN Marathon 2.0*, Padova, Italy.

7.2018 **Contributed Poster**, *International conference on nitride semiconductors*, Strasbourg, France.

7.2018 **Contributed Poster**, *Compound Semiconductor Week*, Berlin, Germany.

3.2017 **Contributed Talk**, *European Workshop on Molecular Beam Epitaxy*, St. Petersburg, Russia.

10.2016 **Contributed Poster**, *International Workshop on Nitride Semiconductors*, Orlando, USA.

9.2016 **Contributed Talk**, *International Conference on Molecular-Beam Epitaxy*, Montpelier, France.

Patents

I. Rousseau and **P. Sohi.** Vacuum gauge based on III-nitride semiconductor surfaces. (Patent Application) PCT/IB2018/053177 2018

Publications

P. Sohi, J.-F. Carlin, and N. Grandjean. Investigating the low electron mobility of AlN/GaN/AlN two-dimensional electron gases (in preparation).

P. Sohi, M. Mosca, Y. Chen, J.-F. Carlin, and N. Grandjean. Low-temperature growth of n^{++} GaN by metalorganic chemical vapor deposition to achieve low-resistivity tunnel junctions on blue light emitting diodes. *Semicond. Sci. and Technol.*, 34(1):015002, 2019.

P. Sohi, J.-F. Carlin, and N. Grandjean. Alloy disorder limited mobility of InGaN two-dimensional electron gas. *Appl. Phys. Lett.*, 112(26):262101, 2018.

P. Sohi, D. Martin, and N. Grandjean. Critical thickness of GaN on AlN: Impact of growth temperature and dislocation density. *Semicond. Sci. and Technol.*, 32(7):075010, 2017.

S. Hennel, B. A. Braem, S. Baer, L. Tiemann, **P. Sohi**, D. Wehrli, A. Hofmann, C. Reichl, W. Wegscheider, C. Rössler, T. Ihn, K. Ensslin, M. Rudner, and B. Rosenow. Nonlocal polarization feedback in a fractional quantum hall ferromagnet. *Phys. Rev. Lett.*, 116:136804, 2016.

Ce document a été imprimé au Centre d’impression EPFL,
imprimerie climatiquement neutre, certifiée myClimate.